HIGH ANGULAR RESOLUTION DIFFUSION IMAGING OF BRAIN WHITE MATTER AND ITS APPLICATION TO SCHIZOPHRENIA

By

Xin Hong

Dissertation

Submitted to the Faculty of the

Graduate School of Vanderbilt University

in partial fulfillment of the requirements

for the degree of

DOCTOR OF PHILOSOPHY

in

Biomedical Engineering

May, 2010

Nashville, Tennessee

Approved:

Professor Adam W. Anderson

Professor Zhaohua Ding

Professor Mark D. Does

Professor Daniel F. Gochberg

Professor John C. Gore

To my beloved parents

ACKNOWLEDGEMENTS

I am heartily thankful to my advisor, Dr. Adam W. Anderson, for his knowledge, guidance, patience, and support through all these years I have been working with him. I could not wish for a better advisor. I offer my sincerest gratitude to Dr. John C. Gore, director of the Institute of Imaging Science. I feel lucky to be a member of such a nurturing research environment. I am grateful to Dr. Zhaohua Ding for his advice and many invaluable discussions and advices. Thanks also go to other members of my dissertation committee, Dr. Mark D. Does and Dr. Daniel F. Gochberg, for their time and thoughtful comments on the manuscript.

I would like to thank my labmates Dr. Lori R. Arlinghaus, who helped collect and pre-processed the images of the schizophrenia study, Dr. Ha-Kyu Jeong, who provided helpful suggestions and volunteered to be scanned, and Ann S. Choe, who always encourages me and cheers me up.

I would like to thank Dr. Herbert Meltzer in the Department of Psychiatry and Dr. Sohee Park in the Department of Psychology for their help with the schizophrenia study. My appreciation also goes to Dr. Benoit M. Dawant and the members of his Medical Image Processing laboratory in the Department of Electrical Engineering and Computer Science, Dr. Xia Li, Dr. Yong Li, and Rui Li, for their expert assistance with image registration. This work was supported by grants from the NIH/NIBIB (R01-EB02777 and R01NS058639).

Finally, I owe my deepest gratitude to my parents and my husband. This thesis would not have been possible without their immense love, encouragement and support.

TABLE OF CONTENTS

Page

LIST OF TABLES

LIST OF FIGURES

LIST OF ABBREVIATIONS

ACC	Angular Correlation Coefficient
acg	anterior corona radiata
acr	anterior coronal radiata
ADC	Apparent Diffusion Coefficient
atr	anterior thalamic radiation
cc	corpus callosum
cg	cingulum bundle
CO	normal COntrols
cpt	corticopontine tract
cst	corticospinal tract
DOT	Diffusion Orientation Transform
DSI	Diffusion Spectrum Imaging
DSVD	Damped Singular Value Decomposition
DTI	Diffusion Tensor Imaging
DW	Diffusion Weighted
FA	Fractional Anisotropy
FOD	Fiber Orientation Distribution
FORECAST	Fiber ORientation Estimated using Continuous Axially Symmetric Tensors
fm	forceps major
GCV	Generalized Cross Validation
GFA	Generalized Fractional Anisotropy

GLM	General Linear Model
HARDI	High Angular Resolution Diffusion Imaging
ic	internal capsule
ifo	inferior frontal-occipital fascicules
ilf	inferior longitudinal fascicules
MRI	Magnetic Resonance Imaging
MTSVD	Modified Truncated Singular Value Decomposition
ODF	Orientation Distribution Function
pcg	posterior corona radiata
PAS	Persistent Angular Structure
PDF	Probability Density Function
PGSE	Pulsed Gradient Spin Echo
PPD	Preservation of Principal Direction
PRIDE	Philips Research Imaging Development Environment
QBI	Q-Ball Imaging
RF	Radio Frequency
RMS	Root Mean Square
ROI	Region Of Interest
RSS	Residual Sum of Squares
SENSE	SENSitivity Encoding
scr	superior corona radiata
sfo	superior fronto-occipital fasciculus
SH	Spherical Harmonic

slf	superior longitudinal fasciculus
SNR	Signal to Noise Ratio
SVD	Singular Value Decomposition
SZ	SchiZophrenia
T_1-W	T_1-weighted
T_2-W	T_2-weighted
TGSVD	Truncated Generalized Singular Value Decomposition
unf	uncinate fasciculus

LIST OF SYMBOLS

S	Diffusion weighted signal
S_0	Non-diffusion weighted signal
$tr(\widetilde{b})$	Trace of the diffusion weighting matrix
$\widetilde{b}$	Diffusion weighting matrix
b	Trace of the diffusion weighting matrix
D	Diffusion coefficient, Diffusivity
$\widetilde{D}$	Diffusion tensor
$\vec{r}$	Diffusion gradient direction
$\vec{q}$	Diffusion gradient wave-vector
$\overline{\lambda}$	Mean diffusivity
$\lambda_{\perp}$	Radial diffusivity
L	Maximum order of SH expansion
α	Weighting factor in regularization
$\vec{c}_l$	Convolution kernel expansion coefficients
$\vec{p}_{lm}$	Vector of the expansion coefficients of the FOD
l	Order of spherical harmonic
m	Degree of phase factor
$\vec{s}_{lm}$	Vector of the expansion coefficients of $\vec{S}$
$\vec{S}$	Vector of the diffusion weighted signal
$\widetilde{X}$	Design matrix

$\sigma_{s_0}^2$	Variance of the non-diffusion weighted signal
σ_s^2	Variance of the diffusion-weighted signal
$\vec{r}_i$	i^{th} sampling vector
$\widetilde{M}$	Scatter (second moment) matrix of the sampling points
κ	Intravoxel fiber orientation coherence index
ε_i	Eigenvalues of matrix $\widetilde{M}$
$\bar{\varepsilon}$	Mean of the three eigenvalues of matrix $\widetilde{M}$
$\widetilde{J}$	Jacobian matrix
θ	Polar angle of the spherical coordinates
φ	Azimuthal angle of the spherical coordinates
$P(\theta,\varphi)$	Fiber orientation distribution at angle (θ,φ)
$\widetilde{J}_\Omega$	Angular Jacobian matrix

CHAPTER I

INTRODUCTION

Overview

Diffusion Tensor Imaging (DTI) (1) has become the primary imaging modality for non-invasive characterization of the microstructure of living tissues, particularly of human white matter. The technique is based on the fact that the self-diffusion of water molecules is sensitive to the microscopic composition, structure, and organization of tissues (2,3). Despite its success in research areas such as neural fiber tractography (4-6) and in various clinical applications (7-21), the technique suffers from some fundamental limitations (22). One major problem is that the classic second order tensor model is not able to adequately describe non-Gaussian diffusion, and thus not able to provide reliable estimations of the underlying tissue properties. New imaging techniques such as high angular resolution diffusion imaging (HARDI) (23-27) and new data reconstruction methods such as the Q-ball imaging (QBI) (28-30) have been proposed to address the problem.

This chapter includes: (a) the basic concept of diffusion and the properties of diffusion that are measured and analyzed in this study, (b) the principles of diffusion

tensor imaging, its applications and limitations, (c) a brief introduction to new diffusion MRI techniques including acquisition and data reconstruction methods.

Diffusion and its Properties

Diffusion, also called Brownian motion, refers to the random translational motion of water molecules driven by thermal energy. There are two important aspects in describing diffusion. In a homogeneous medium where water molecules can move freely, the amount of movement is described statistically by the diffusion coefficient, or diffusivity, D, a scalar measure proportional to the mean squared molecular displacement per unit time. Diffusivity relies on several intrinsic properties of the medium: the mass of the molecules, the temperature, and the viscosity. On the other hand, in heterogeneous media, such as a biological sample, the measured diffusivity in an imaging voxel is the ensemble average of all the water molecules within the voxel, which is usually different from the intrinsic diffusion coefficient measured from a homogeneous medium. To distinguish these two concepts, the averaged diffusivity is named the apparent diffusion coefficient (ADC). ADC depends not only on the medium's intrinsic properties, but also on the measurement parameters, such as the voxel size.

In addition to the amount of the displacement, water diffusion has another important property, its directionality. If the averaged displacements are identical in all directions within a given elapsed time, the diffusion is isotropic. Otherwise, the diffusion

is anisotropic if the displacements vary along different directions. One example of isotropic diffusion occurs in the cerebrospinal fluid in the brain ventricles, where water molecules can move freely in any direction within the typical measurement time. In tissues like neural fibers, where the cellular architecture is highly organized, water encounters fewer barriers (such as microfilaments, membranes or myelin) along the primary axis of the fibers than perpendicular to this axis. Therefore, the molecular displacement along the fiber orientation is significantly larger than in other directions, showing strong anisotropy (31,32).

The two properties of water diffusion, the overall diffusivity and its directional dependence, can provide useful information about the microscopic structure of biological tissues. Given an appropriate diffusion time (typically 30~50 ms for human brain diffusion MRI), the random walk of water molecules may reflect restrictions and hindrances by various barriers, such as macromolecules and cellular membranes, resulting in different diffusivity properties from freely diffusing bulk water. The microstructure of the samples can thus be inferred based on the measured diffusivity. In brain white matter, the degree of diffusion anisotropy is mainly determined by the packed and coherent axonal membranes, with some influence from myelin and other intracellular micro structures as well (3). Therefore, diffusion anisotropy provides a unique way to non-invasively probe the neural fibers' structure.

Diffusion Tensor Imaging

Diffusion properties are usually measured with a Pulsed Gradient Spin Echo (PGSE) pulse sequence in MRI experiments (33,34), featuring a pair of identical diffusion sensitizing gradient pulses applied along a prescribed direction before and after the 180º refocusing RF pulse. During the first gradient pulse, molecules at different positions will precess at different frequencies and thus will accumulate phase angles that depend on the molecules' positions along the gradient direction. The 180º RF pulse and the second gradient pulse aim to cancel the position dependent phase angle. The spins that are de-phased by the first pulse will re-phase if they remain stationary during the time between the two gradients. Otherwise, if the water molecules diffuse to different positions, the effect of the first gradient can not be completely reversed by the second one. The de-phased spins will thus result in an attenuated signal intensity compared to the intensity measured without diffusion weighting:

$$S = S_0 e^{-tr(\tilde{b})D} \qquad (1)$$

where S and S_0 are the signal intensity measured with and without the diffusion sensitizing gradients (also known as the diffusion weighted signal and un-weighted signal), respectively. $\tilde{b}$ is the diffusion weighting matrix describing the strength and timing of the diffusion gradients. With negligible gradient ramp times and gradient cross terms, the diffusion sensitivity of the gradients can be represented by the trace of the matrix $\tilde{b}$, $tr(\tilde{b})$, also known as the diffusion weighting factor, or simply the b factor.

According to Eq.(1), the diffusion coefficient D can be calculated with as few as two measurements, one with the diffusion sensitizing gradients, and the other without the gradients.

For isotropic diffusion, the measured ADCs are identical when the diffusion gradients are applied in different directions. For anisotropic diffusion, the greater the diffusion along a certain direction, the more attenuated the measured signal will be along that direction, i.e., the measured ADC depends on the direction of the applied gradients. Therefore, the scalar ADC is not sufficient to fully describe anisotropic diffusion in 3D space. In the early 1990s, the tensor model was proposed to better address this problem (1). Instead of a scalar ADC, the diffusion tensor, a positive definite, symmetric 3×3 matrix with six independent elements is utilized to characterize anisotropic diffusion. To measure the diffusion tensor, at least seven independent measurements are required, six diffusion weighted measurements along six non-collinear directions, plus one un-weighted. If the diffusion gradients are aligned with the sample's natural symmetry axes (also called the principal axes), the resulting tensor is a diagonal matrix, with diagonal elements corresponding to the ADCs along these axes. In most experiments on living samples, the tissues' principal axes are unknown, it is thus impossible to align the diffusion gradients with them. In this case, the eigenvalues of tensor indicate the ADCs along the three principal directions given by the corresponding eigenvectors.

The diffusion tensor provides three kinds of information about the tissue's properties. First, the trace of the tensor describes the overall diffusivity (mean over all

directions) within the imaging voxel. This measure is related to properties such as the cell density, and the volume ratio of intracellular and extracellular space. Second, diffusion anisotropy can be described by various anisotropy indices derived from the tensor. These indices describe how much the diffusion profile deviates from isotropy. Anisotropy is sensitive to important structural properties such as degree of myelination of the neural fibers can be inferred from these indices. One of the most widely used anisotropy indices is Fractional Anisotropy (FA), which can be calculated from the eigenvalues of the tensor and ranges from 0 for isotropic diffusion to 1 for anisotropic diffusion. Third, the eigenvector associated with the largest eigenvalue of the diffusion tensor is assumed to indicate the principal orientation of the underlying structure. Many algorithms have been developed to map neural fiber tracts and study the connectivity between different regions of the brain based on this information (35,36).

Due to the ability of DTI to probe the microstructure of tissues non-invasively, it has been applied to a wide range of research areas such as brain development(7), and aging (13), and a wide range of diseases and injuries including acute stroke (8,14,15), multiple sclerosis (9,16-18), epilepsy (10,19) and brain tumors (12,20,21) and treatment evaluation (37,38) (for a review of the clinical applications, see (39)).

Although the diffusion tensor model works fairly well in identifying fiber orientations in some parts of the brain, it fails in other regions. One of the most significant limitations of DTI is its inability to describe diffusion where orientation heterogeneity occurs within an image voxel (22,40).

One reason for this problem is the size mismatch between the imaging voxel and the underlying structures. The typical neural axon diameter ranges from less than 1 micron to more than 30 microns in human brain (41), while the typical voxel size in the clinical and research environment is on the scale of millimeters. Therefore, it is inevitable that some of the voxels contain fibers of heterogeneous diffusion properties. Several different situations may occur. First, multiple fiber populations of different orientations may show up within one voxel, for example, the so-called fiber crossing, 'kissing', and joining configurations. Second, fiber populations of the same orientation but different intrinsic diffusion properties may occur, for example, when one of the fiber bundles is affected by some disease. Third, even a single fiber bundle may change its orientation within one voxel, which is referred to as fiber bending. Fourth, intra-axonal and extra-axonal spaces with different diffusion properties may share a voxel. All these possibilities complicate the interpretation of the diffusion tensor. The conventional second-order tensor model is based on the single Gaussian diffusion assumption, which gives only one principal direction of the diffusion displacements, the tensor model is therefore insufficient in describing diffusion with multiple preferential directions.

This limitation results in two major problems of the tensor model in areas where complicated structures are present. First, the principal eigenvector associated with the largest eigenvalue can no longer be assumed to be the dominant diffusion direction, which makes fiber tracking based on the tensor model unreliable. Second, the anisotropy

indices derived from the tensor model may be misinterpreted when two fiber bundles with different anisotropy share a voxel (22,42).

High Angular Resolution Diffusion Imaging

To address the limitations of DTI and provide more accurate measurements of diffusion, new imaging techniques, as well as new data reconstruction methods, have been proposed. A straightforward way to reveal more details of the diffusion process is to obtain measurements in more directions and with more levels of diffusion sensitivity (multiple *b* values). One example is diffusion spectrum imaging (DSI) (30,43,44), which collects diffusion measurements by sampling a three-dimensional Cartesian grid in q-space, which can be used to estimate the spin displacement probability density function (PDF) from the signal through a Fourier transform (45). The spin displacement orientation distribution function (ODF) is then reconstructed by a radial projection of the PDF. The peaks of the estimated ODF provide directional information on the underlying structures. Since DSI is model-independent, it is capable of resolving multiple intravoxel fiber populations. However, in order to collect signals at all points of the Cartesian lattice to satisfy the Nyquist condition, DSI requires strong diffusion gradients and long image acquisition times. Both of these drawbacks limit its widespread clinical application.

To accommodate the usual requirements of the clinical environment: short imaging time and modest gradient strength, an alternate imaging method termed high

angular resolution diffusion imaging was developed (23-27). Taking the middle ground between DTI and DSI, this technique obtains a number of measurements along directions evenly distributed on a spherical shell in q-space (i.e., in more than six directions with a single *b* value), and thus achieves a balance between the requirements for detailed angular information and for long imaging time and strong gradients.

Various data reconstruction schemes have been developed to extract diffusion properties and reveal tissue structural information from the HARDI signal. A straightforward extension of the single Gaussian tensor model is multiple tensor fitting (23,46), which approximates the diffusion function as a mixture of multiple Gaussian tensors in voxels containing more than one fiber component. However, this method faces two major difficulties, model selection (the number of component tensors in each voxel needs to be determined before the fitting) and non-linear fitting (an optimization technique is needed to determine the best proportion for each component tensor). Another approach includes spherical harmonic (SH) decomposition of the ADC (24,47), which expresses the ADC profile function as a series of harmonic coefficients, and the generalized tensor model (26,48) , which expresses the diffusivity profile as a tensor of higher rank (>2). The major limitation of these methods is their inability to provide directional information on the underlying structures, since the maxima of the diffusion profile may not necessarily correspond to the principal directions of fast diffusion (49). Persistent angular structure (PAS) (27), a function on the sphere which extracts the angular information from the spin displacement probabilities, provides one way to infer

the directional structure being imaged. Since the calculation of PAS involves numerical integration and non-linear optimization, this method is computationally intensive. Phase analysis of diffusion circular spectrum (50) is another way to identify multiple intravoxel fiber orientations by utilizing the phase information of the circular spectrum of the ADC profiles. The accuracy of the estimated fiber orientations is limited by its major assumption of an orthogonal crossing angle between two fiber components of equal volume fractions, which is hard to guarantee in *in vivo* data. The diffusion orientation transform (DOT) (51) provides another model-free way to transform diffusion profiles into probability profiles. However, this method is based on the assumption of mono-exponential signal decay along each sampling vector in the q-space, which is not always valid. Q-Ball imaging (QBI) (28-30) is particularly popular due to its straightforward, model-independent reconstruction. Based on the Funk-Radon transformation, the fiber orientation distribution function along any direction γ is estimated directly by integration of the diffusion weighted signal measured along directions perpendicular to γ. Since the reconstruction of the ODF makes no *a priori* assumption about the distribution of the underlying diffusion process, QBI is able to reveal multiple fibers within a voxel. One drawback of QBI is that it usually requires a relatively high *b* value to achieve acceptable angular resolution.

An alternative strategy to resolve multiple intravoxel fibers is spherical harmonic deconvolution (52-54). Making the assumption that all fiber components sharing a voxel have the same intrinsic diffusion properties, the observed diffusion signal can be

expressed as a convolution of a single fiber response function and a fiber distribution function. Once the response function is estimated, the fiber distribution can be reconstructed by spherical deconvolution. This method provides a direct estimate of the fiber orientation distribution, which is not available from the other methods mentioned above. The implementation proposed by Tournier (53) is limited in that a fixed response function is used for the whole dataset, which is equivalent to assuming the intrinsic diffusion properties are the same for all the fiber populations in the entire brain.

Although the techniques mentioned above are capable of resolving multiple intravoxel fibers, none of them, except for the multiple tensor model and generalized tensor model, provides information about the intrinsic diffusion properties within each voxel. In certain developmental or pathological conditions, the change of intrinsic diffusivity (for example, due to changes in cell density, or damage to the myelin layers) could result in decreased FA values. Decrease of coherence in fiber orientation could also reduce the FA. None of these data analysis approaches is able to distinguish the possible causes.

CHAPTER II

ESTIMATION OF WHITE MATTER PROPERTIES USING THE FORECAST MODEL

Overview

A new HARDI data reconstruction method termed Fiber ORientation Estimated using Continuous Axially Symmetric Tensors (FORECAST) (54) has been proposed. Compared with other reconstruction methods, FORECAST is able to provide a more accurate description of diffusion properties, especially in complex areas where the classic tensor model fails.

This chapter includes: (a) a brief introduction to the FORECAST model, (b) optimization of the FORECAST analysis based on numerical simulations, and (c) an introduction to an intravoxel fiber orientation coherence index.

The FORECAST model

FORECAST is a HARDI data reconstruction technique based on a multiple tensor model. It assumes that within a voxel, different fiber components have the same proton density, the same relaxation properties, and negligible exchange between the components within the given diffusion time. The model further assumes that the diffusion tensor for each

fiber component is axially symmetric, with one larger eigenvalue and the other two equal and smaller. The measured signal is the sum of contributions from all the individual tensors. With a further assumption of uniform mean and radial diffusivity ($\bar{\lambda}$ and $\lambda_{\perp}$, respectively) within a voxel, the diffusion weighted signal can be expressed as a convolution of the fiber orientation distribution (FOD) function and the response function from an ideal single fiber. Instead of using a single response function for the entire brain as proposed in the other spherical convolution method (53), FORECAST estimates the response function for each voxel. The single fiber response function depends on the *b* value, the mean and radial diffusivities, and the angle between the diffusion gradient direction and the fiber orientation. By expressing the functions in terms of spherical harmonics, the convolution relationship between the measured signal and the fiber angular distribution becomes a simple algebraic equation in terms of spherical harmonic coefficients. Once the radial diffusivity is estimated from the relation between the signals, the *b* value and the presumed mean diffusivity, the single fiber response function is obtained. The fiber angular distribution function can then be recovered. The peaks of the FOD function provide information about the underlying fiber components. The orientation of each peak estimates the primary orientation of the fiber, and the magnitude of each peak is assumed to be proportional to the volume fraction of the corresponding fiber.

Table 1. Comparisons of diffusion imaging techniques.

Method	Number of directions		Model
	Min.	Typical	
DTI	6	30	$S(\vec{r}) = S_0 \cdot \exp(-b \cdot \vec{r}^T \widetilde{D} \vec{r})$
QBI	18	252	$\psi(\vec{r}) = \int_{\vec{q} \perp \vec{r}} S(\vec{q}) d(\vec{q})$
FORECAST	18	92	$S(\theta,\varphi) = S_0 \cdot \exp(-b\lambda_\perp) \int_0^{2\pi} \int_0^{\pi} P(\theta',\varphi') \cdot \exp(-3b \cdot (\overline{\lambda} - \lambda_\perp) \cos^2 \beta) \sin\theta' d\theta' d\varphi'$

Note: S and S_0 are diffusion weighted and non-diffusion weighted signal, b is the diffusion weighting factor. In the DTI model, $\widetilde{D}$ is the diffusion tensor. $\vec{r}$ is the diffusion gradient direction. In the QBI model, $\vec{q}$ is the diffusion gradient wave-vector, ψ is the orientation distribution function. In the FORECAST model, θ and φ are the polar and azimuthal angles of the diffusion gradient direction, $P(\theta',\varphi')$ is the fiber distribution in the direction (θ',φ'), $\overline{\lambda}$ and $\lambda_\perp$ are the mean and radial diffusivity, β is the angle between (θ,φ) and (θ',φ').

The FORECAST model has several advantages over the QBI method. First, at moderate b levels accessible to common clinical routines, FORECAST can not only better recover multiple fibers within a voxel (54), it is also capable of resolving topological ambiguities such as fiber crossing, kissing, joining, and bending (55). Second, by estimating both the radial diffusivity and fiber angular distribution in each voxel, FORECAST is capable of distinguishing two different causes of decreased FA: fiber coherence change versus fiber intrinsic diffusivity change (see the last section of this chapter for further details). Third, by expressing functions in terms of SHs, the FORECAST model is computationally efficient, involving only linear matrix calculation, avoiding integration or interpolation. Note that recently QBI ODF reconstruction algorithms have also adopted the SH approach. (54,56,57).

Optimization of the FORECAST analysis

One problem with the spherical deconvolution technique is its high susceptibility to noise. High order SH approximation of the FOD function is desirable in order to achieve high angular resolution (54) so that fibers with small orientation differences within a voxel can be distinguished. However, the higher order the SH expansion is, the higher is its susceptibility to noise. In order to reduce the effect of noise and enhance the solution robustness, several techniques have been developed, including an order-dependent low pass filter (53), minimum entropy minimization (58), and Tikhonov regularization (56,57,59-61). Selective filtering, by empirically choosing small weighting factors for high-order items and large weightings for low-order items, attenuates the high frequency noise, at the cost of reduced angular resolution. The automatic entropy method eliminates user interaction, but the non-linear optimizer does not guarantee a globally optimized solution.

Tikhonov regularization is a popular method to enhance the numerical stability of least squares problems by imposing additional constraints on the solution. Different types of constraints have been proposed. The simplest one is to minimize the Euclidean norm of the solution. Descoteaux and coworkers defined a cost function describing the roughness of the FOD surface (57). Alternatively, one can minimize the magnitude of the negative peaks of the FOD, which represent noise (59). There are several computational methods to obtain the regularized solution: directly solving the least-squares equations,

or converting the equations into a generalized form and finding the least-squares solution in an iterative manner (61), or choosing from the Singular Value Decomposition (SVD) based methods, including Damped SVD (DSVD), Modified Truncated SVD (MTSVD), Truncated Generalized SVD (TGSVD) and others (57,62). To determine the optimal regularization weighting factor α, one can choose a value empirically (59,61), by the L-curve method (57), or by Generalized Cross Validation (GCV) (60). There is a freely-available MATLAB regularization software package, including the abovementioned computational methods based on SVD, the L-curve and GCV methods, that can be used to choose the regularization parameter (63). Though improvements brought by various regularization techniques have been demonstrated for other spherical harmonic reconstruction methods (56,57,59-61), none has been reported for the FORECAST model.

The main goals of this study include: 1. to quantify the effects of regularization on the FORECAST model's robustness to noise. We aim to determine the optimal cost function, computational methods and algorithm to determine the optimal regularization parameter. 2. To explore the FORECAST model's performance, specifically its dependence on the regularization method. 3. To determine the optimal parameters (for both imaging and data reconstruction) for FORECAST analysis of clinical studies of white matter diseases.

Methods

Negative peak regularization

The reconstructed fiber distribution function from spherical deconvolution may contain negative values in some orientations due to noise and SH truncation. Because the FOD gives the estimated volume fraction of fibers along each orientation, a negative FOD value is certainly non-physical, and should be eliminated (59). To identify the orientations along which the estimated FOD has negative magnitudes, the FOD is estimated in 1002 directions evenly distributed over a sphere (generated by 10^{th} order icosahedral tessellation of the sphere). The sum of the negative FOD values can then be used as the cost function in the Tikhonov regularization. The position and magnitude of the negative FOD lobes can vary depending on the maximum order SH used, leading to different constraint and regularization results. In this study, we tested the regularization algorithm in two different schemes. In the first, referred to as 'same-order' regularization, the regularization term is based on the FOD estimated to the same maximum order L as the fitting error term and the final FOD. In the second scheme, termed 'lower-order' regularization, proposed by Tourier et al. (59), the maximum order of the SHs in the regularization term is $(L-2)$ instead of L.

In addition to the FOD negative values, other cost functions including the Euclidean norm of the FOD coefficients and the roughness of the FOD surface, combined with various computational methods and algorithms to determine the regularization

parameter were tested. The MATLAB routines provided by Hansen (63) were adapted and applied to evaluate these. Since the routines work for real matrices, complex SH were converted into real SH according to (64). Based on our preliminary results (not shown), the discussion will be focused on regularization based on negative peak minimization and solved in two ways, direct least-squares solution combined with empirically chosen α, and DSVD combined with GCV.

Monte Carlo simulation and figures of merit for performance evaluation

Two fibers with equal volume fraction and crossing angle ranging from 60º to 90º were simulated with $\overline{\lambda} = 0.9 \times 10^{-3} mm^2/s$ and $\lambda_{\perp} = 0.54 \times 10^{-3} mm^2/s$. For each structure, different values of three key imaging parameters were tested (b=1000, 2100, and 3250s/mm^2, number of diffusion gradient directions (32, 92, and 252), and SNRs varied from 10 to 100 in steps of 10). For each SNR (signal to noise ratio) level, random noise with zero mean and standard deviation of S_0/SNR, where S_0 is the ideal signal without diffusion weighting, was added to the ideal signal (both the diffusion weighted and un-weighted). For each combination of the given structure and imaging parameters, 500 Monte Carlo trials were performed. For each resulting dataset, FORECAST analysis was applied using various parameters, including the maximum fitting order (4th or 6th order), the regularization order (same-order or lower-order) for negative peak regularization, and the method of regularization and determination of the weighting factor α (DSVD+GCV,

or direct least-squares calculation with a preset value ranging from 0.0001 to 1). The mean and standard deviation of the estimated radial diffusivity were compared. The mean and standard deviation of the FODs over 500 trials were calculated. The angular bias of the mean FODs from the true fiber orientation was compared. In addition, the mean and standard deviation of the following figures of merit for each configuration were compared.

i). Angular deviation of the FOD peaks from the true fiber orientation.

ii). Angular Correlation Coefficient (ACC) between the estimated FOD and the true FOD. The ACC is a natural similarity measure concerning both the shape and orientation between two spherical functions, ranging from -1 (perfect negative correlation) to 1 (exactly identical) (54). According to our preliminary studies, an ACC value of at least 0.8 is desirable for reproducible estimation of the FOD.

Since the FOD depends on the estimated radial diffusivity, to investigate if improved estimation of $\lambda_\perp$ will help better estimate the FOD, we re-ran the simulations replacing the estimated $\lambda_\perp$ by the true $\lambda_\perp$ value. The resulting FODs were compared to the FODs obtained using the original algorithm.

Human data acquisition and analysis

In addition to the numerical simulation, we validated the techniques using *in vivo* human data. HARDI data from a normal subject were acquired with informed consent on a

Philips 3T scanner (Philips Healthcare, Andover, MA). A single-shot EPI sequence was employed with $\mathrm{TE} = 48\mathrm{ms}$, $\mathrm{TR} = 10{,}000\mathrm{ms}$. The dataset contains $96 \times 96 \times 55$ isotropic voxels at the spatial resolution of 2.5 mm. Diffusion weighting (b=1000s/mm^2) was applied along 92 directions given by the 3rd order icosahedral tessellation of a sphere (these 46 directions and their opposites give 92 directions). Sensitivity encoding (SENSE) was used with a SENSE factor of 3 in order to reduce total imaging time. Four identical scans were acquired for the purpose of studying reproducibility.

FORECAST analysis was performed with negative peak regularization using the optimal parameters determined by simulations (shown in the next section). Furthermore, the bootstrap method (65) was applied in order to investigate the reproducibility of fiber orientation. For each voxel, a set of 92 diffusion weighted signals was drawn randomly from the pool consisting of the 4 acquisitions, and the process was repeated for a total of 500 trials. FORECAST analysis was performed on the 500 re-sampled datasets, and on the high-SNR dataset achieved by averaging the 4 acquisitions. For each voxel, the FOD calculated from the high-SNR dataset was considered to be the 'gold standard', and the peaks of the FOD were assumed to indicate the 'true' fiber orientation. The fiber orientations estimated by each of the 500 FODs from the re-sampled dataset were compared to the ‘true FODs’. The mean and standard deviation of the FOD surfaces over the 500 re-samples were also calculated for visual inspection.

Results

Results of simulations

i). Effect of negative peak regularization

The mean FOD surfaces and the mean plus one standard deviation (mean+std) FOD surfaces in Figure 1 and 2 demonstrate that with the proper choice of the regularization order and the weighting factor α, regularization based on negative peak minimization is able to reduce the effects of noise and help to reveal the true peaks of FODs. Comparisons of the figures of merit further confirms the improvement by regularization in terms of lower mean angular error, higher mean ACC and smaller angular bias of the mean FOD maxima, as shown in Figure 3. The improvement is prominent at low *b* values, small numbers of diffusion gradient directions, and low SNRs. For example, for the 60º-crossing-fiber structure acquired using 92 diffusion directions, b=1000s/mm^2 and SNR=30, the 6th order fitting with proper regularization (lower-order regularization with α=0.03) is able to reach a mean angular error of 13º compared to 36º without regularization, a mean ACC of 0.64 compared to 0.05, an angular bias of the mean FOD peaks of 1.3º compared to 4.5º.

The results also show that the lower-order regularization outperforms the same-order regularization compared for matching imaging parameters, in that it better separates the crossing fibers, provides lower mean angular error, higher mean ACC and smaller angular bias of the mean FOD maxima.

The key problem associated with regularization is the choice of the weighting factor α. For all the imaging conditions and the range of α tested here, the optimal value of α for negative peak regularization depends on imaging parameters such as the *b* value, number of diffusion gradient directions, and the fitting order, as well. Choosing the optimal α from a range of preset values is a trade off among all the figures of merit, requiring considerable user interaction. For example, the peaks of the mean regularized FOD are narrower with α=0.006 than with α=0.01, but the angular bias from the true orientations and the mean angular error is larger. In general, the higher the *b* value, and/or the larger the number of diffusion directions, the smaller α is needed. Table 2 summarizes the optimal value of α under the imaging situations tested here. Note that within the range of the SNR tested, especially when higher than 30, the optimal value of α does not vary much.

Table 2. Optimal weighting factor α under various imaging situations (SNR>=30).

Number of directions	*b* value (s/mm^2)		
	1000	2100	3250
32	0.03	0.03	0.02
92	0.03	0.02	0.02
252	0.01	0.01	0.01

GCV provides an automatic way to determine the regularization weighting factor. Based on simulations at moderate to high SNRs, the combination of DSVD and GCV is able to provide similar regularization as using the value chosen as above. In fact, the optimal α value for each imaging situation determined by DSVD+GCV is close to (most of the time somewhat smaller than) the one chosen based on Monte Carlo simulations. At a low SNR level (<30), however, the α value determined by DSVD+GCV has large variations, and hence unstable regularization performance. Figure 1 compares the optimal α value determined under various imaging situations.

Different options for the constraint functions (the solution norm, the FOD surface roughness, the negative FOD peaks), computational methods (direct least-squares, DSVD, TGSVD and other SVD based methods), and ways to determine the regularization parameter (L-curve, GCV) were combined and their performance was tested by Monte Carlo simulation and compared with the negative peak regularization. The results (not shown) indicate that the negative peak regularization outperforms other methods, at least in the tested conditions, in terms of the overall shape of the mean FOD and the relatively small standard deviation. It appears that the L-curve approach generates too large a value for α, resulting in over-regularization, independent of the cost function, or calculation method used. On the other hand, the optimal α determined by GCV seems to be a bit too small, which leads to under-regularization and large variance of FODs.

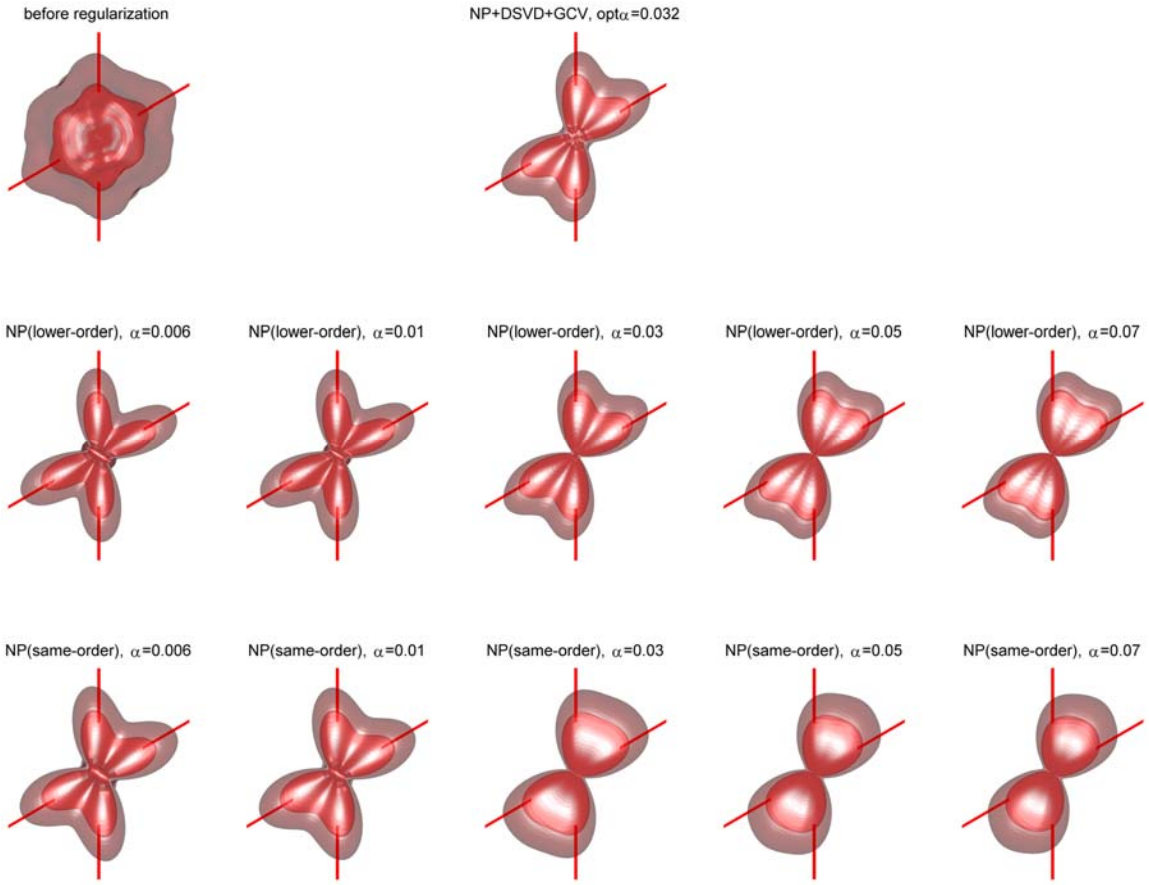

Figure 1. The mean (opaque) and the mean+standard deviation (transparent) FOD surfaces regularized by different methods and different weighting factors. Data were simulated at b=1000s/mm^2, 92 diffusion directions, SNR=30, analyzed through 6th order. The red lines denote the true fiber orientations. The title of each subplot gives the corresponding cost function and the α value. For NP+DSVD+GCV, the α value is the mean over the 500 trials. (regularization methods: NP=Negative Peak, DSVD=Damped Singular Value Decomposition, GCV=Generalized Cross Validation).

ii). Effect of the fitting method

Theoretically speaking, higher order SH gives higher angular resolution, at the cost of higher susceptibility to noise. The simulation results in Figure 2 and 3 show that without regularization, FODs fitted through 6th order are much noisier than those through 4th order.

However, with proper regularization, the 6th order fitting can give sharper peaks and lower angular error.

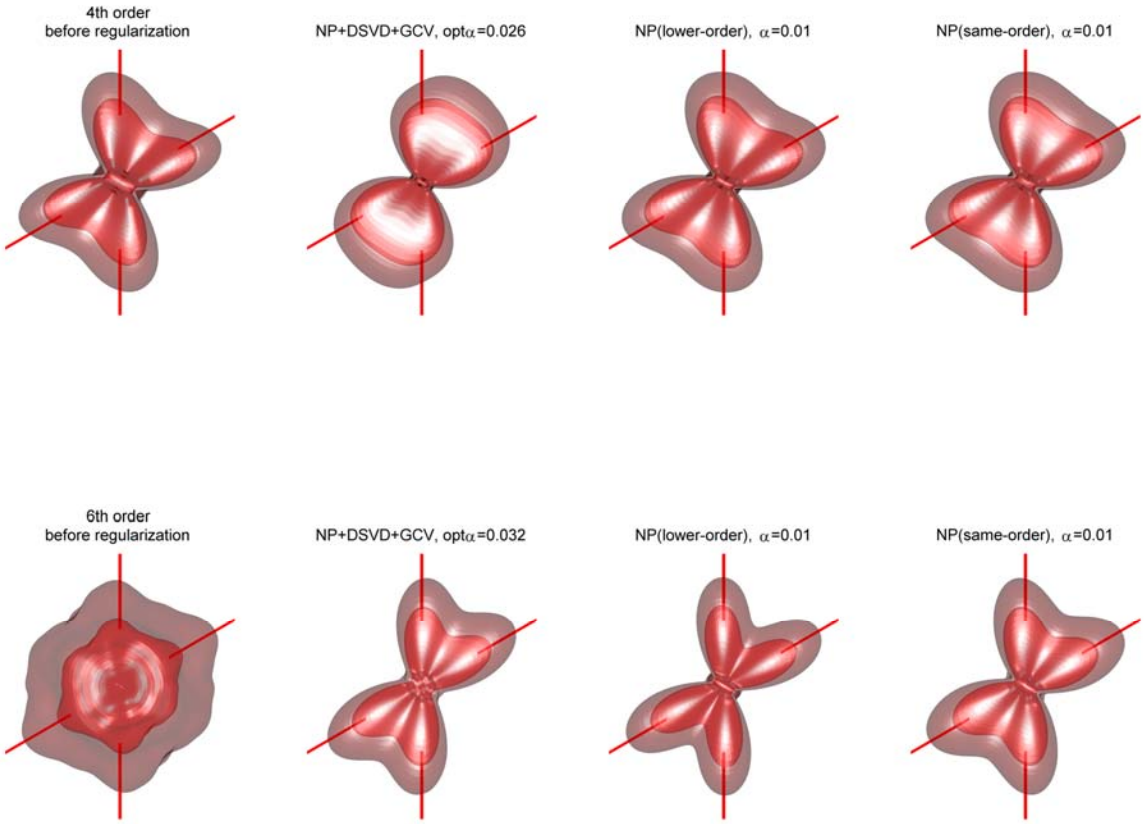

Figure 2. The mean (opaque) and the mean+standard deviation (transparent) FOD surfaces regularized by different methods and different weighting factors (each column) and fitted through different maximum orders (each row). Data were simulated at b=1000s/mm^2, 92 diffusion directions, SNR=30. The red lines denote the true fiber orientations. The title of each subplot gives the corresponding regularization method and the α value. For NP+DSVD+GCV, the α value is the mean over the 500 trials.

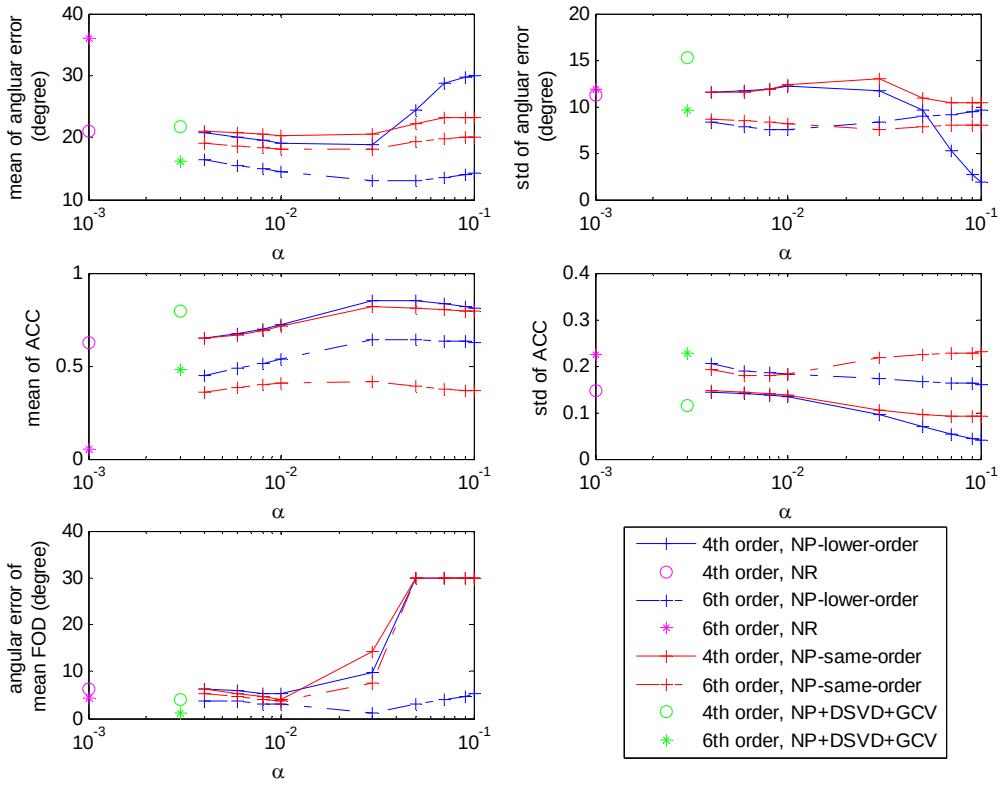

Figure 3. Dependence on analysis parameters for two fibers crossing at 60º. Each subplot shows one figure of merit vs. α regularized by different methods and fitted through different maximum orders. Angular error measures the difference in orientation between an FOD peak and the true fiber. In each subplot, solid lines and circle denote a maximum order of 4, dash-dot lines and star denote a maximum order of 6. Color denotes regularization methods: magenta (non-regularized, NR, displayed on the vertical axis for reference), green (NP+DSVD+GCV), blue (NP-lower-order), and red (NP-same-order). (ACC=angular correlation coefficient).

iii). Effect of the number of diffusion directions

Figure 4 and 5 show the dependence of FORECAST performance on imaging parameters. As expected, the 252-direction acquisition outperforms the 92-direction acquisition, which in turn is better than the 32-direction acquisition. This confirms the hypothesis that

the more measurements acquired, the higher the achievable angular resolution will be as a matter of practice. The advantages are more prominent at low SNR levels. Since the acquisition time for HARDI is proportional to the number of diffusion directions, the time for 92-direction scan roughly allows for three 32-direction scans. According to theory, the SNR of the averaged three 32-direction datasets should be about 1.7 times that of a single image of the 92-direction dataset without averaging, i.e., the results from the 92-direction data at a SNR level of 20 should be comparable to the results from the 32-direction data at a SNR level of 34. Our simulation results at b=1000s/mm^2 show close agreement with this prediction in terms of the angular error and ACC measures. In fact, the 92-direction acquisition outperforms the imaging-time-matched 32-direction measurement, while the 252-direction measurement achieves a mixed performance (higher angular error and higher ACC) compared to the imaging-time-matched 92-direction measurement, and better compared to the imaging-time-matched 32-direction measurement. Furthermore, as the b value increases from 1000s/mm^2 to 3250s/mm^2, the advantage of the high number of diffusion measurements over low number of measurements becomes more obvious, probably because the benefit of high diffusion sensitivity overrides the effect of the increased SNR achieved by image averaging. Another possible explanation is the non-linear relationships between the SNR and the evaluation figures of merit.

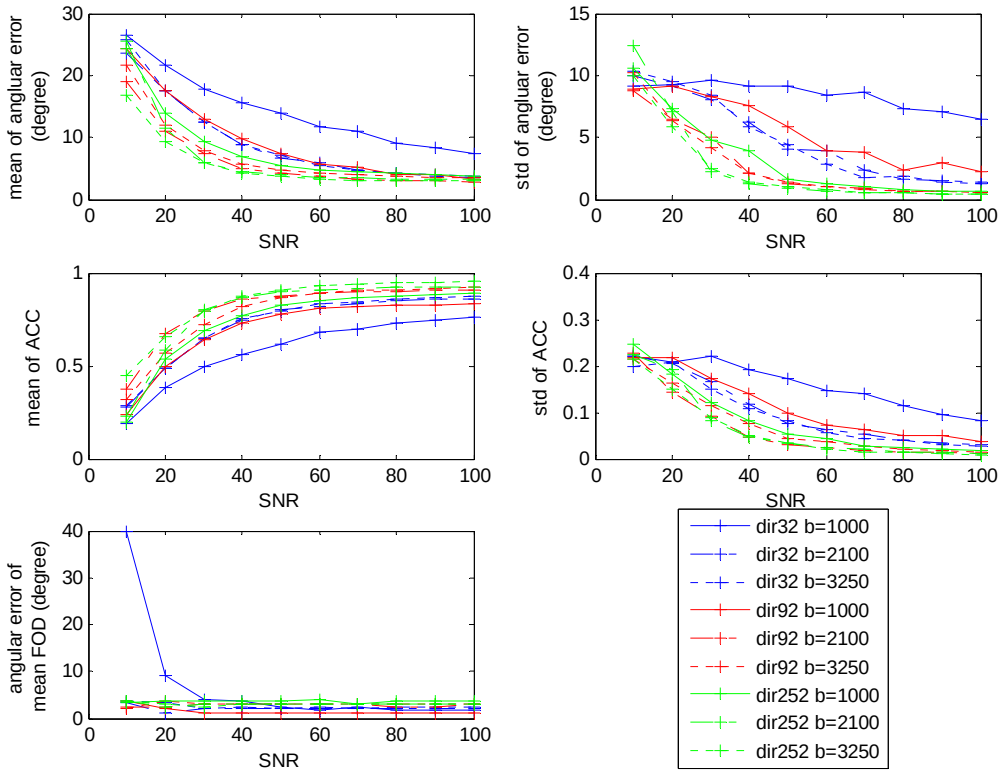

Figure 4. Dependence on imaging parameters for two fibers crossing at 60º, fitted through 6th order, regularized by the lower-order NP regularization and the optimal α value chosen for each configuration (Table 1). Each subplot shows one figure of merit vs. SNR at various numbers of measurement directions and *b* values. In each subplot, solid lines, dashed lines, and dotted lines denote *b* values of 1000, 2100 and 3250s/mm^2, respectively. Blue, red, and green denote 32, 92, and 252-direction measurements, respectively.

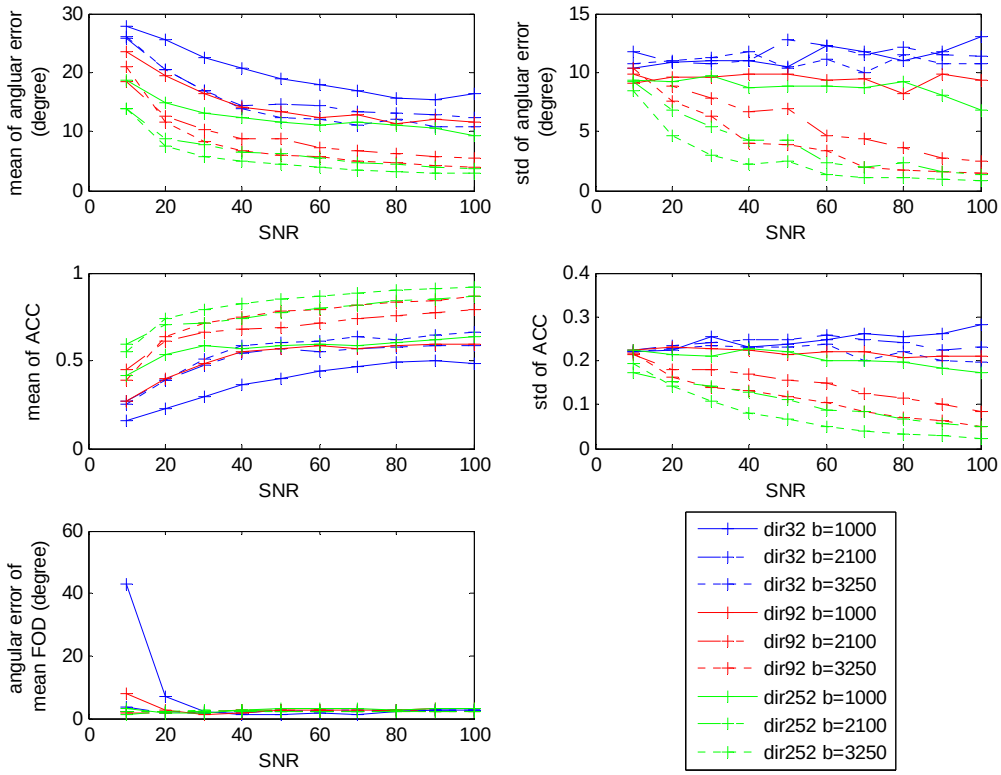

Figure 5. Dependence on imaging parameters for two fibers crossing at 60º, fitted through 6th order, regularized by the lower-order NP regularization and the optimal α value determined by DSVD+GCV. Each subplot shows one figure of merit vs. SNR at various measurement numbers and *b* values. In each subplot, solid lines, dashed lines, and dotted lines denote *b* values of 1000, 2100 and 3250s/mm^2, respectively. Blue, red, and green denote 32, 92, and 252-direction measurements, respectively.

iv). Effect of the b value

The simulation results also demonstrate that when data are analyzed through 4th order, measurements at $b = 2100 s/mm^2$ and $b = 3250 s/mm^2$ produce similar performance, both significantly better than measurements at $b = 1000 s/mm^2$ (results not shown). When analyzed through 6th order, however, a *b* value of 3250s/mm^2 provides the lowest

angular deviation and the highest ACC among the 3 b values, though the differences between $b = 2100 s/mm^2$ and $b = 3250 s/mm^2$ are not large.

v). Effect of the SNR

As expected, the simulations demonstrate that the higher the SNR, the lower the angular deviation and angular bias of the mean FOD, and the higher the ACC. Generally, a SNR level no less than 30 is required to separate 2 fibers crossing at 60º.

vi). Comparison to QBI

We also compared the performance of the FORECAST FOD and QBI ODF based on signals simulated using a high b value (3250s/mm^2). Results are shown in Figure 6. It is obvious that the FORECAST FOD is able to reveal the true fiber orientations better than the QBI ODF.

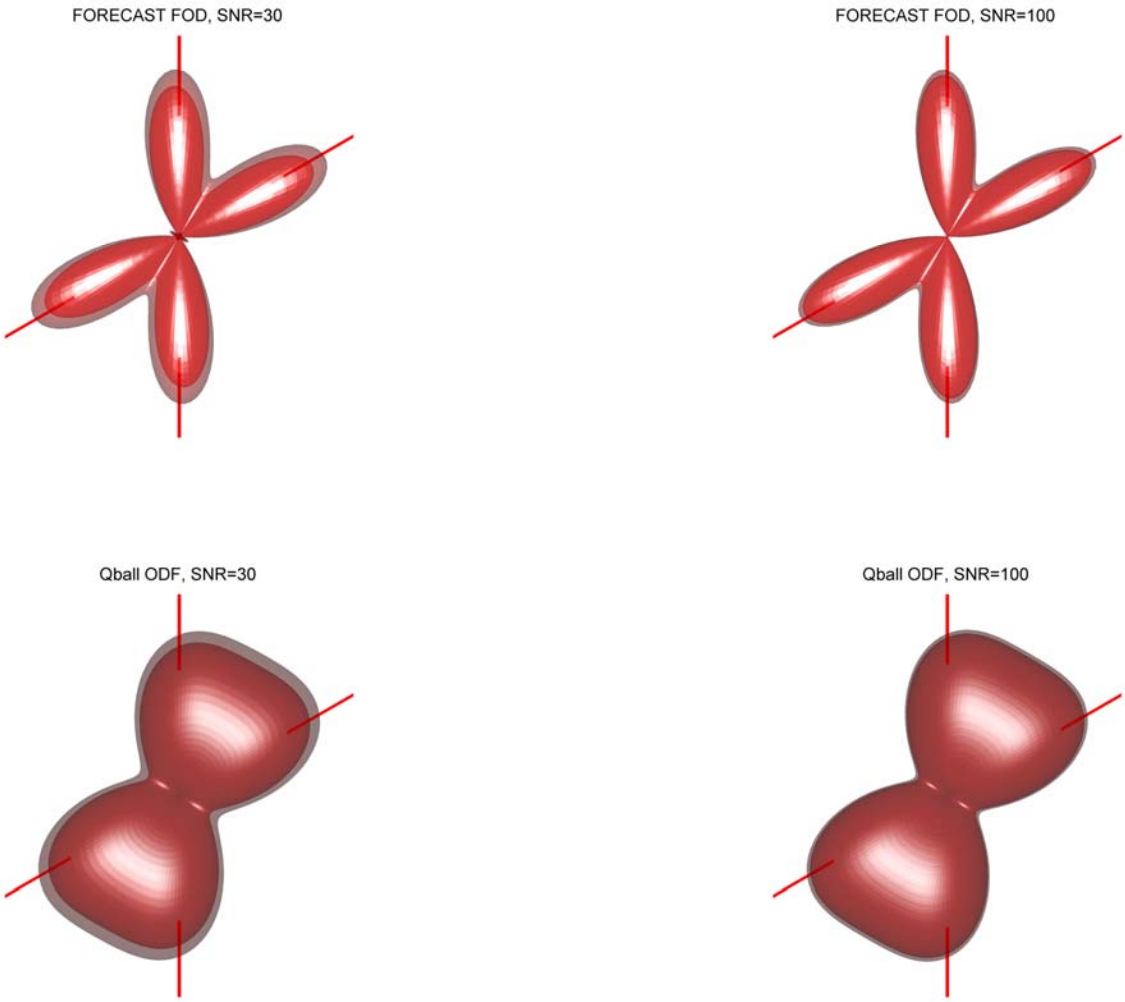

Figure 6. Top: the mean (opaque) and the mean+standard deviation (transparent) FOD surfaces by FORECAST. Bottom: the mean (opaque) and the mean+standard deviation (transparent) ODF surfaces by QBI. The red lines denote the true fiber orientations. Data were simulated at b=3250s/mm^2, 252 diffusion directions, SNR=30, 100, respectively, and fitted through 6th order. The FORECAST FODs were regularized using lower-order NP regularization with the optimal α value determined as in Table 1.

vii). Estimation of the radial diffusivity

As shown in Figure 7, the FORECAST model over-estimates the radial diffusivity under the tested conditions. The bias does not vary much with a SNR level above 30, though the

standard deviation becomes smaller with higher SNR. For the same number of diffusion directions, the higher the *b* value, the smaller the bias. For the same *b* value, 32-direction acquisition gives the smallest bias. The 92 and 252-direction acquisitions provide comparable bias, but the larger the number of diffusion directions, the smaller the standard deviation of the estimated $\lambda_\perp$. Using $b = 1000 s/mm^2$ and 92 diffusion directions, the radial diffusivity is over-estimated about 19%.

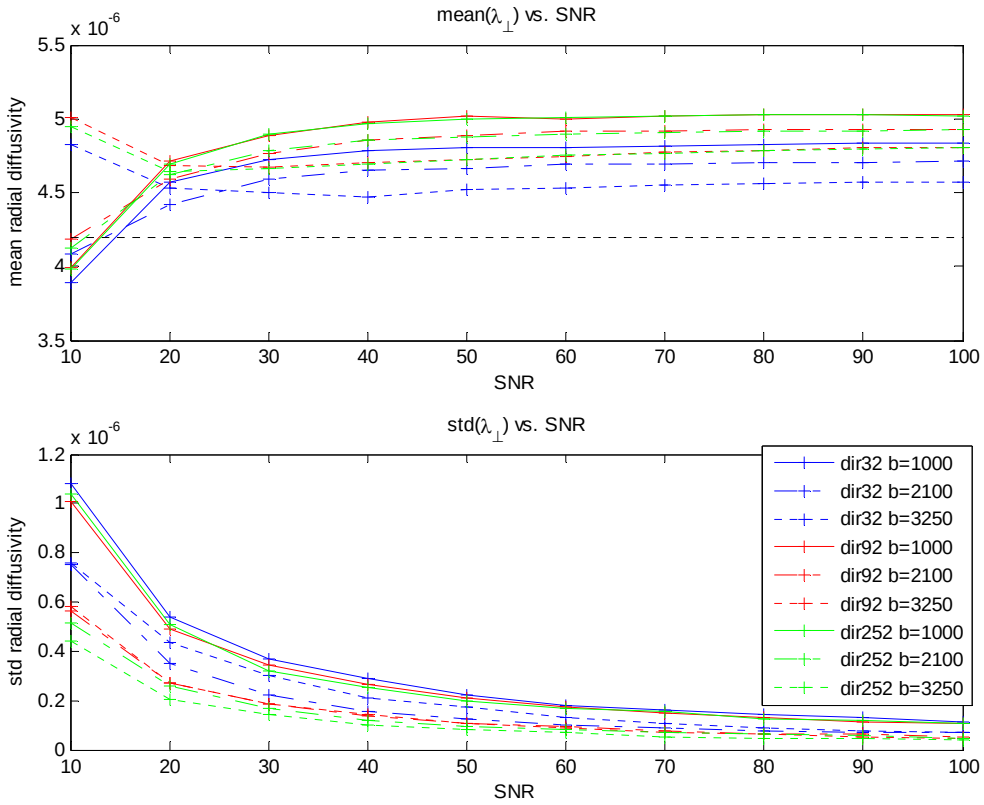

Figure 7. The mean (top) and standard deviation (bottom) of radial diffusivity over 500 trials estimated using various imaging parameters. The black dotted line denotes the true radial diffisivity.

The re-calculation of FOD using the true radial diffusivity shows that a more accurate estimation of $\lambda_\perp$ is able to improve the estimation of fiber orientations. While the improvement is obvious before regularization, it becomes negligible after proper regularization (see Figure 8).

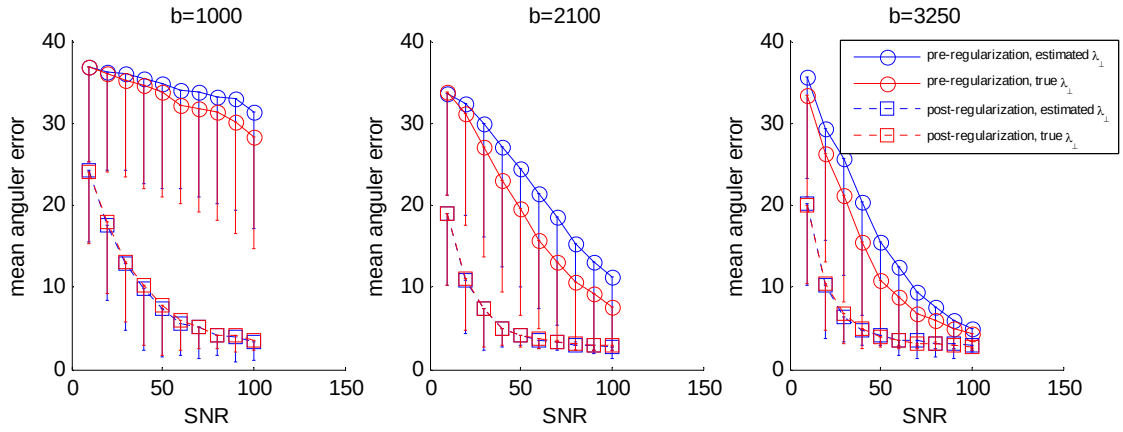

Figure 8. Comparison of fiber orientation accuracy between simulations using the estimated and true radial diffusivity values, and between pre and post regularization. Data were simulated using 92 diffusion direnctions and 3 different *b* values (see each panel), with the SNR level ranging from 10 to 100. FODs were approximated to 6^{th} order and regularized by minimizing negative peaks of the 4^{th} order FODs with α=0.03.

Results for in vivo human data

FORECAST analysis was performed on the *in vivo* dataset acquired. The SNR was estimated to be about 40 for a single acquisition based on the Residual Sum of Squares (RSS, i.e., estimating the noise based on the residuals of a 6^{th} order SH fit of the signal as a function of orientation). According to the simulation results, the optimal analysis

parameters were chosen as follows: the 6th order fitting and lower-order negative peak regularization with $\alpha = 0.03$, or with α determined by DSVD+GCV. Both methods were applied and the results were compared.

Figure 9 compares the FODs regularized by the two methods on one axial slice of the averaged high SNR data. The α value chosen by DSVD+GCV for that slice ranges from 0.00015 to 0.11, with a mean value of 0.013 and a median value of 0.0076. The FODs regularized with the fixed α value (0.03) tend to be slightly 'over-regularized', while those with α chosen by DSVD+GCV for each voxel appear to be 'under-regularized'. Taking the example of the genu of the corpus callosum *(cc*) (e.g., in the yellow ellipse in Figure 9), the FODs regularized by the individually determined α contain extra lobes in the anterior-posterior orientation with significant magnitudes, even in the position of the median line. These small lobes do not agree with the known anatomy, and therefore are considered noise. Another example of under-regularization is the second fiber component in the left-right direction among the anterior-posterior oriented superior fronto-occipital fasciculus (*sfo*) (e.g., in the blue ellipse in Figure 9).

The results in Figure 9 also demonstrate that in regions where fiber bundles with different orientations cross, the FORECAST model is able to distinguish the fiber components. For example, in the voxels containing both corpus callosum fibers and cingulum (*cg)* fibers, the estimated FODs show clearly two peaks oriented in the left-right and anterior-posterior directions, respectively, indicating the orientation of the two fiber bundles (see the orange ellipse in Figure 9). In the area where the *sfo* (in the

anterior-posterior direction), corticopontine tract/corticospinal tract (*cpt/cst*) (in the superior-inferior direction), and the local association fiber (in left-right direction) meet, the FODs exhibit three distinct peaks each giving the principal orientation of these tracts (see the purple ellipse in Figure 9).

The mean and mean+std of the FOD surfaces over the 500 bootstrap resamples in the same ROI regularized by the two methods are compared in Figure 10. The maps of the mean angular deviation from the 'true' fiber orientations over the 500 resamples are shown in Figure 11. Figure 12 compares the mean ACC over the resamples with respect to the ‘true’ FODs in the same slice. These results further illustrate that a fixed α value of 0.03 produces more stable results than DSVD+GCV, in terms of smaller variation in the FOD surfaces, more consistent fiber orientation (for example, see the *sfo* highlighted in the red ellipses in Figure 10), smaller angular deviation from the 'true' fiber orientations, and higher similarity to the ‘true’ FODs.

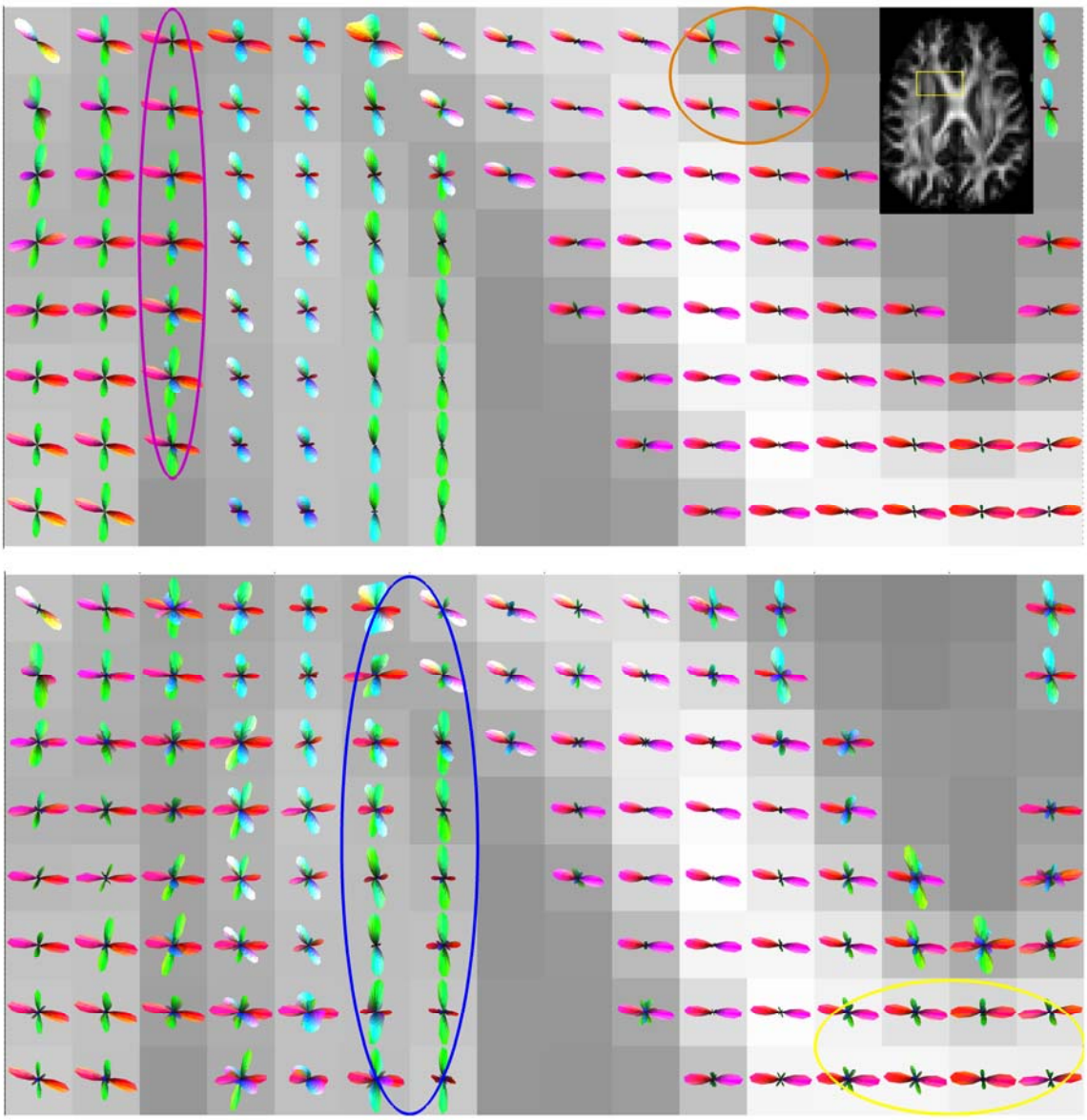

Figure 9. FORECAST analysis on averaged images. Inset: FA map with ROI highlighted in the yellow box. Top: FODs regularized with α=0.03. Bottom: FODs regularized with α determined individually for each voxel by DSVD+GCV. The FODs in voxels with low FA (<0.2) are not shown.

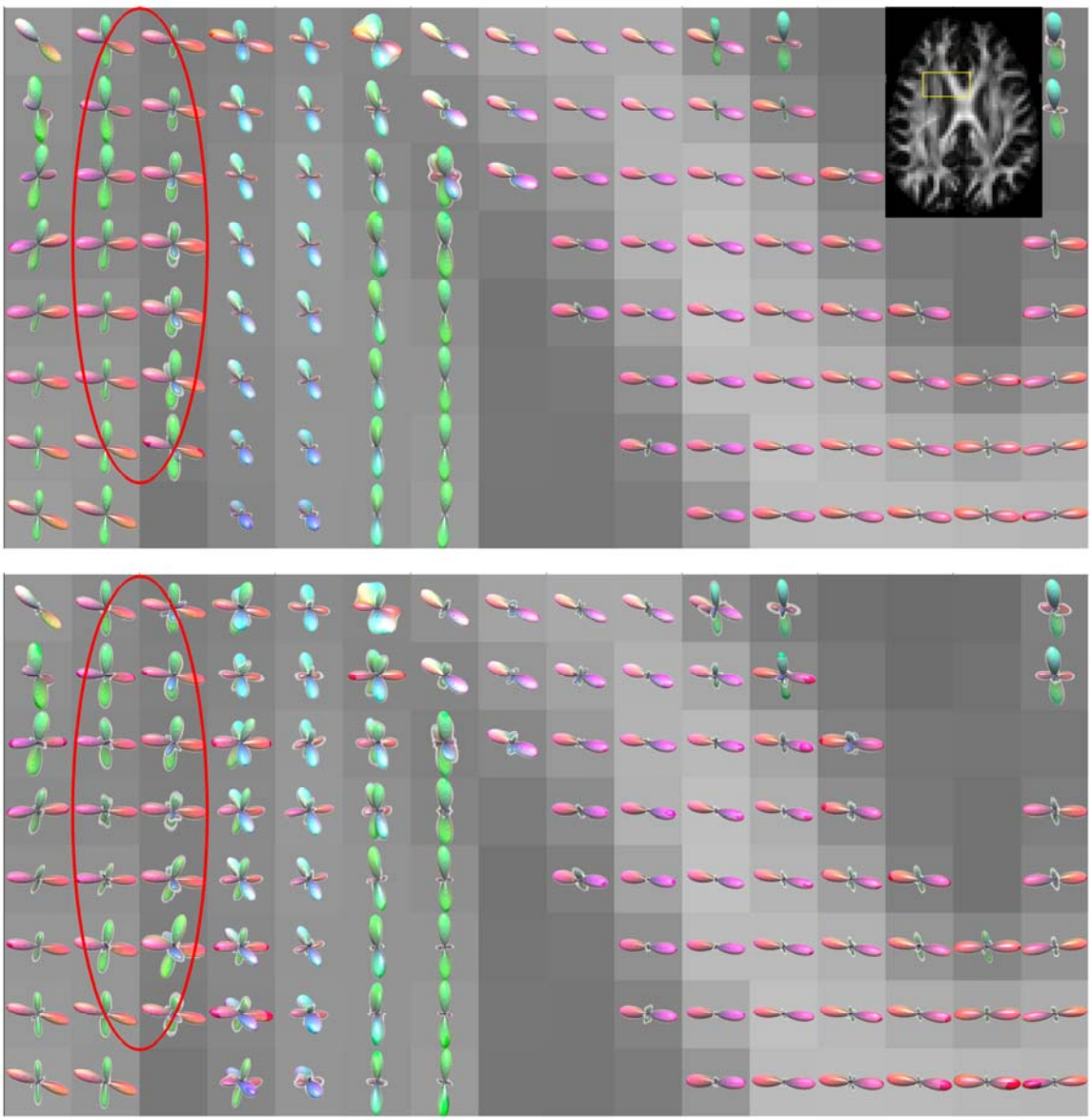

Figure 10. Bootstrap results: the mean (opaque) and the mean+standard deviation (transparent) FOD surfaces. Inset: FA map with ROI highlighted in the yellow box. Top: regularization with α=0.03. Bottom: regularization with α determined individually for each voxel by DSVD+GCV. The FODs in voxels with low FA (<0.2) are not shown.

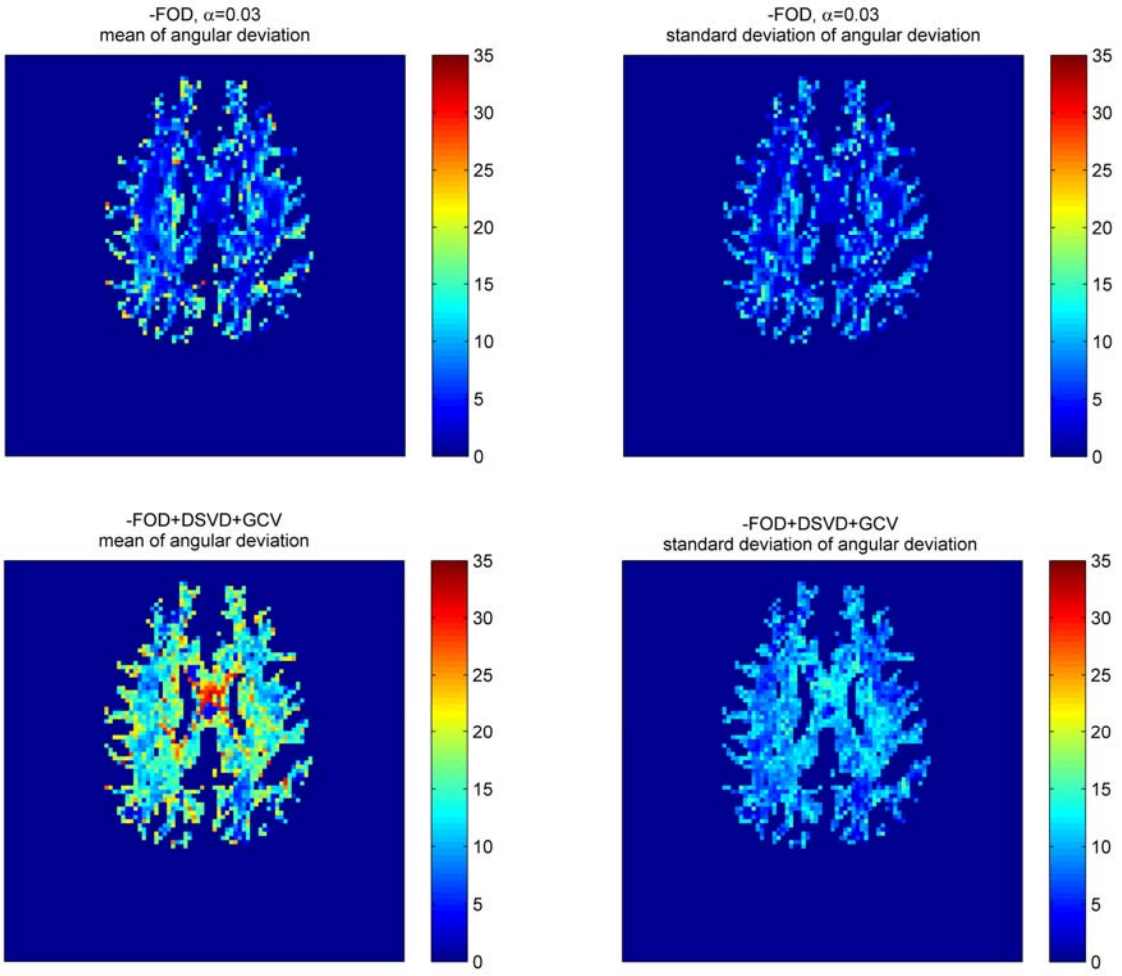

Figure 11. Maps of the mean and standard deviation of the voxel-wise fiber orientation error. Top: results with α=0.03. Bottom: results with α determined individually for each voxel by DSVD+GCV.

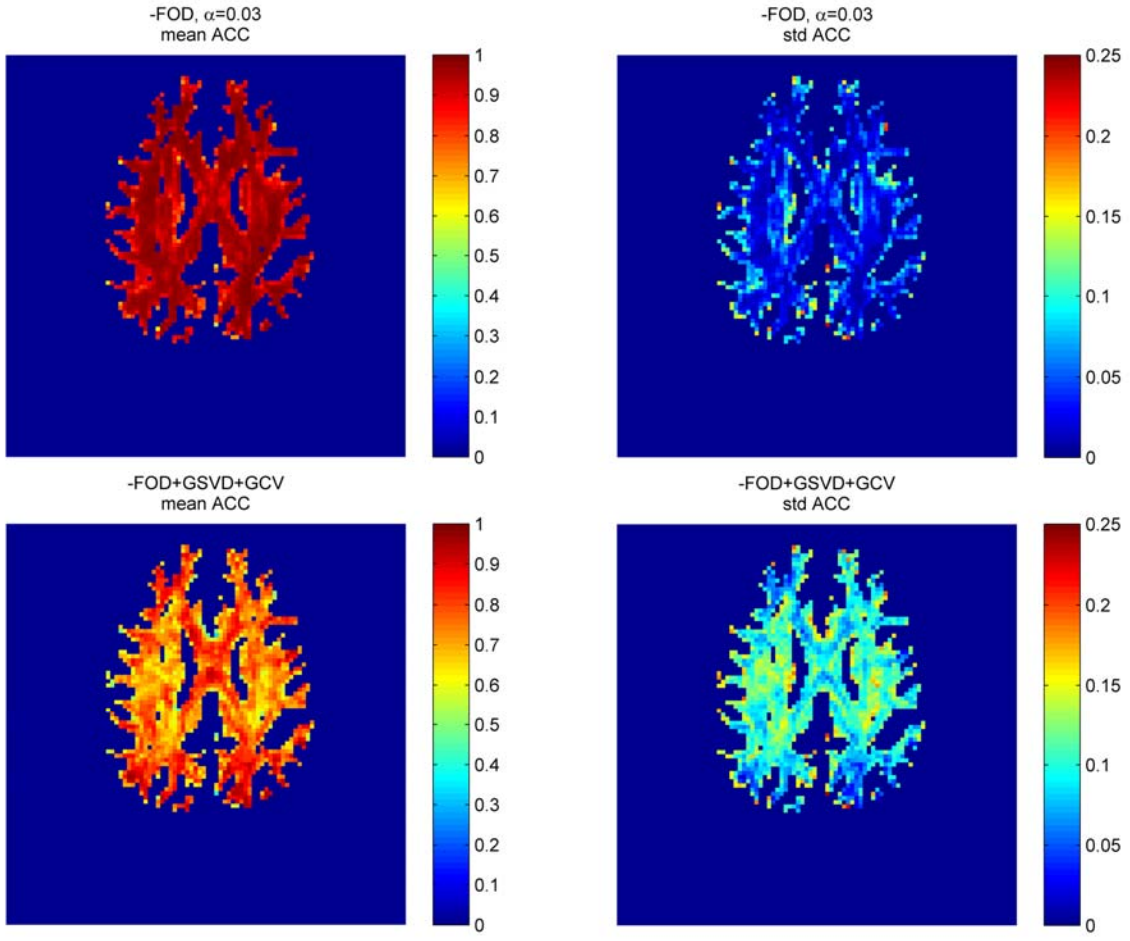

Figure 12. Maps of the mean and standard deviation of ACC. Top: results with α=0.03. Bottom: results with α determined individually for each voxel by DSVD+GCV.

Discussion

The simulation results indicate that the 6th order FORECAST analysis is able to provide reliable estimates of the fiber orientation, at least for up to two fibers in a voxel, and in the *b* value and the SNR range tested. In theory, high order SHs contain high spatial frequency components of the approximated functions. Therefore, the higher the fitting

order, the narrower the angular point spread function, and the higher the angular resolution. On the other hand, the HARDI measurement is sensitive to noise. The high order fitting will be more sensitive to high frequency noise. To overcome the effect of noise and achieve satisfactory results with the 6^{th} order fitting, a higher *b* value and/or a higher SNR is required. With data acquired at low *b* values and low SNRs, one way to improve the estimation is regularization. The simulations demonstrate the improvements by Tikhonov regularization based on minimizing the negative peak of the 4^{th} order FOD.

The *in vivo* data acquired and analyzed using the optimal parameters chosen by the simulations further demonstrates the feasibility of the FORECAST analysis on clinical data. In this study, a dataset with a low *b* value of 1000s/mm^2, 92 diffusion gradients, and a SNR level of above 30 was acquired within 17 minutes, which is achievable in the common clinical environment. The FORECAST analysis with proper regularization is able to produce reliable estimates of the fiber orientations (less than 10º error in most white matter voxels).

When choosing the best α from a range of preset values, the weighting of each figure of merit for overall performance evaluation is somewhat arbitrary. In order to minimize the effects of the individual analyzer and to reduce the processing time, it is desirable to develop an automatic algorithm for the choice of α. The software package by Hansen (63) provides some automatic methods. Among them DSVD+GCV seems to work the best for the FORECAST model based on our simulations. However, the *in vivo* data analysis shows that the α value automatically determined by DSVD+GCV tends to

be too small, even for data with a high SNR level estimated to be around 80. The small mean/median α value (smaller than the empirically chosen one) explains the under-regularization, and the large variation in the α value leads to unstable regularization performance. Despite these shortcomings, the optimal α value estimated by DSVD+GCV could serve as a reference in the future development of a better algorithm.

According to the simulations, to achieve estimates of the fiber orientations as accurate as possible within limited imaging acquisition time, it seems better to acquire a larger number of diffusion directions than to repeat a smaller number of directions. The simulation results also indicate that when data are analyzed through 4^{th} order, measurements with b values of 2100s/mm^2 or 3250s/mm^2 produce lower angular deviation and higher ACC than at a b value of 1000s/mm^2. When analyzed through 6^{th} order, the higher the b value (among these 3 values), the better the performance. This result can be explained by the relationship between the convolution kernel expansion coefficients $\vec{c}_l$ and the b value, and the relationship between the theoretical variance of $\vec{c}_l$ and $\vec{p}_{lm}$ (the SH coefficients of the FOD, where the non-negative integer l denotes the SH order, and the integer m denotes the degree or phase factor). $\vec{c}_l$ depends on the b value, $\lambda_\perp$ and the fitting order. Using the 6^{th} order fitting $|c_l|$ reaches its maximum at $b = 3200 s/mm^2$ for the value of $\lambda_\perp$ used in this study. The theoretical variance of $\vec{p}_{lm}$ is proportional to $1/|c_l|$ (see APPENDIX B for detailed derivation). Therefore, for a given $\lambda_\perp$ and the 6^{th} order fitting, $b = 3200 s/mm^2$ gives the smallest variance of $\vec{p}_{6m}$, which produces the most reliable FOD estimates. For 4^{th} order fitting, a b value of

3250s/mm^2 gives performance similar to that of 2100s/mm^2, even though $|c_l|$ reaches its maximum at $b = 2100 s/mm^2$. One possible explanation is the difference of $|c_l|$ at these two b values are small.

A factor affecting the conclusions of this study is the possible violation of the assumptions of the FORECAST model. The FORECAST model assumes that diffusion within a fiber is cylindrically symmetric and within each voxel all fiber components share the same radial diffusivity, which is not always true. Studies suggest that in some regions, the diffusion profile of a coherent fiber bundle may be oblate instead of prolate (40). In addition, fiber components within a voxel may have unequal radial diffusivities. Nevertheless, violation of the identical radial diffusivity assumption affects the volume fraction more than the fiber orientation estimation (54). In the two-fiber simulation of this study, in order to make the analysis simple, the radial diffusivities and the volume fractions of the two fibers were set to be the same. Further investigation needs to be done in the future to explore how to make the estimation more reliable when these assumptions are violated.

Another limitation of the FORECAST model is that estimation of the FOD is dependent on estimation of the radial diffusivity, i.e., errors in the estimated $\lambda_\perp$ may lead to errors in the FOD. According to our simulations, FORECAST tends to over-estimate $\lambda_\perp$, the bias is about 15% under our usual imaging situations ($b = 1000 s/mm^2$, 92 diffusion measurements, SNR=30). More accurate estimation of

$\lambda_\perp$ leads to obvious improvement in the estimation of the FOD without regularization. After regularization, however, the improvement is not obvious. In spite of this, improving the estimation of $\lambda_\perp$ will be helpful in clinical studies of white matter disease.

An intravoxel fiber coherence index

In addition to the partial volume effect, another limitation of the tensor model is the interpretation of the fractional anisotropy. FA is generally interpreted as reflecting the 'integrity' of neural fibers. During the period of brain development or degeneration, or in certain pathological conditions, the organization of fiber bundles, as well as the intrinsic diffusivity of fibers (affected by factors such as the axon diameter, the cell number/density, and thickness of the myelin layer) may change, leading to FA alterations detected by DTI. However, the tensor model is not able to distinguish these possible causes. By estimating both the radial diffusivity and fiber orientation distribution in each voxel, FORECAST has the potential to distinguish between changes in fiber microstructure and fiber organization in cases where anisotropy is altered.

To describe the degree of fiber coherence, some coherence measures based on the eigenvectors of a group of neighboring tensors have been proposed (32,66,67). However, they are not able to describe the degree of coherence within a voxel. Furthermore, in regions with heterogeneous fiber orientations where the tensor eigenvectors do not correspond to the fiber axes, these measures become unreliable.

HARDI techniques provide detailed information of the fiber distribution. A scalar, rotationally invariant measure is needed to describe the degree of fiber coherence based on HARDI data at sub-voxel level. Similar to the definition of FA based on the normalized standard deviation of the tensor eigenvalues, generalized fractional anisotropy (GFA) was defined as the normalized standard deviation of the QBI ODF (29). Although GFA is a good anisotropy measure of the QBI ODF, it is not able to characterize the FORECAST FOD function as well. For example, GFA of the FORECAST FOD does not monotonically decrease as the angle between the two fibers increases. We aim to define an intravoxel coherence measure whose features include rotational invariance, values ranging from 0 to 1, and monotonic dependence on the number of fibers and their crossing angles.

In order to describe quantitatively the degree of fiber orientation coherence within a voxel, we developed a coherence index (κ) based on the fiber orientation distribution function. Calculation of the coherence index is performed in 3 steps:

1. The FOD function is sampled in a number (*N*) of directions evenly distributed over a unit sphere, resulting in N points $\vec{r}_i = [x_i, y_i, z_i], i = 1...N$.
2. A scatter (second moment) matrix of these sampling points, $\widetilde{M}$, is constructed as follows (68):

$$\widetilde{M} = \sum_{i=1}^{N} \vec{r}_i^{\,T} \cdot \vec{r}_i \qquad (2)$$

3. The coherence index is calculated based on the eigenvalues of the scatter matrix in a way similar to the calculation of FA based on the eigenvalues of the tensor matrix.

$$\kappa = \sqrt{\frac{3\sum_{i=1}^{3}(\varepsilon_i - \bar{\varepsilon})^2}{2\sum_{i=1}^{3}\varepsilon_i^2}} \tag{3}$$

where $\varepsilon_i, i = 1,2,3$ are the eigenvalues of matrix $\tilde{M}$, and $\bar{\varepsilon} = \frac{1}{3} \cdot \sum_{i=1}^{3} \varepsilon_i$ is the mean of the three eigenvalues.

The coherence index κ is a scalar, ranging from 0 to 1. Completely incoherent fiber distributions have $\kappa = 0$, whereas parallel fibers have $\kappa = 1$. Examples of simulated intravoxel fiber structures with various crossing angles, their corresponding FODs and κ values are shown in Figure 13.

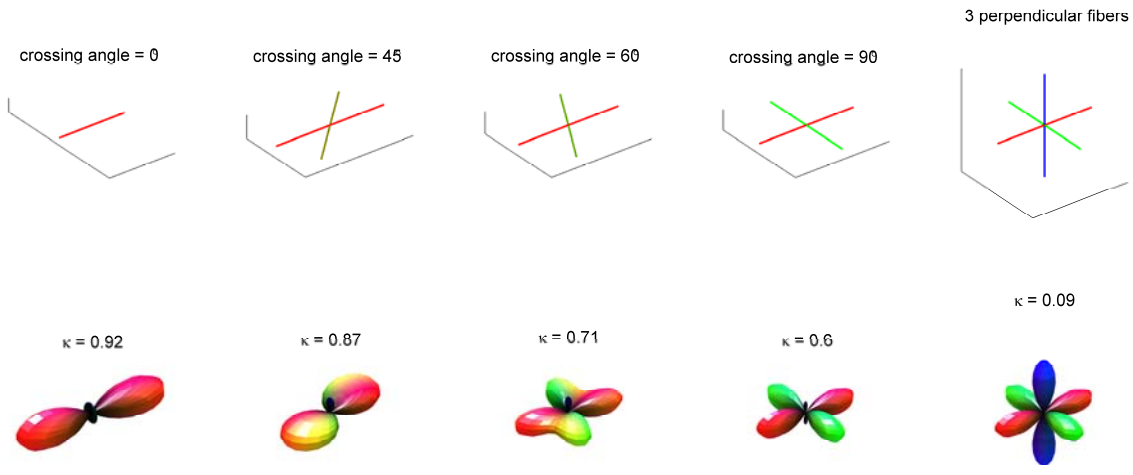

Figure 13. Examples of intravoxel fiber structure (top) and the corresponding FODs and coherence indices.

The relationship between FA, radial diffusivity and κ is of particular interest since FA is thought to reflect both the radial diffusivity and fiber coherence. We investigated the relationship in *in vivo* data. HARDI images of a normal subject were acquired with informed consent on a Philips Intera Achieva 3T scanner, using the following imaging parameters: a single-shot EPI sequence, b=1000s/mm^2, 92 diffusion-sensitizing directions, $\mathrm{TE} = 48\mathrm{ms}$, $\mathrm{TR} = 10{,}000\mathrm{ms}$, SENSE factor $= 3$, $96 \times 96 \times 55$ matrix size, and 2.5mm isotropic voxel size. Four repeats were acquired and averaged to obtain images of a higher SNR. In the remainder of this section the non-averaged and averaged images are referred to as dataset1 and dataset2, respectively. Maps of FA, $\lambda_\perp$ and κ were generated for all the white matter voxels in each slice (segmented by a FA threshold of 0.2). The correlations between FA and κ, and between FA and $\lambda_\perp$ were calculated. Figure 14 shows examples of several slices. As expected, $\lambda_\perp$ appears negatively correlated with FA, and κ is positively correlated with FA, though the correlation between $\lambda_\perp$ and FA is stronger than that between κ and FA.

Figure 14. Examples of FA map, $\lambda_\perp$ map, and κ map of white matter for three axial slices of human data. r and p are the correlation coefficient and the corresponding p value with respect to FA.

We further investigated the variations of $\lambda_\perp$, κ, and FA along a fiber tract. Fiber tracking along the posterior part of the corpus callosum was performed on the above-mentioned *in vivo* dataset using the Philips Research Imaging Development Environment (PRIDE) software by Philips. Then the FA, $\lambda_\perp$, and κ were calculated for each voxel along the tract. Figure 15 shows the FODs and these three measures plotted against position along the tract. It is obvious that radial diffusivity is negatively correlated with FA. In the central segment of the fiber tract, where the coherence is relatively

constant, FA change is mostly due to radial diffusivity change. At the two ends of the tract, however, both increased radial diffusivity and decreased coherence contribute to the reduction of FA.

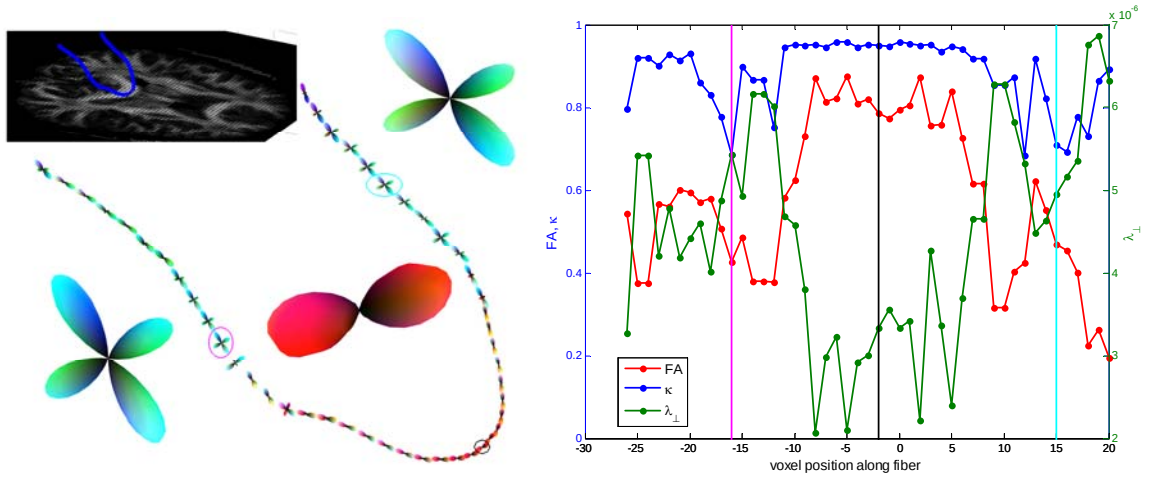

Figure 15. Left: the FODs along a fiber in the corpus callosum (as shown in blue in the FA map). Typical voxels in the middle and at the two ends of the fibers are highlighted. Right: FA, $\lambda_{\perp}$, and κ as functions of the voxel position along the fiber.

CHAPTER III

SPATIAL NORMALIZATION OF THE FIBER ORIENTATION DISTRIBUTION BASED ON HARDI DATA

Overview

Comparison of high angular resolution diffusion imaging measurements between subjects or between time points for the same subject are facilitated by spatial normalization. In this chapter, an algorithm is developed to transform the fiber orientation distribution function, based on HARDI data, taking into account not only translation, but also rotation, scaling, and shearing effects of the spatial transformation. The algorithm is tested using simulated data, and intra-subject and inter-subject normalization of *in vivo* human data. All cases demonstrate reliable transformation of the FOD. This technique makes it possible to compare the intravoxel fiber distribution between subjects, between groups, or between time points for a single subject, which will be helpful in HARDI studies of white matter disease.

This chapter includes: (a) a brief introduction to the challenges that need to be addressed when performing spatial transformation of fiber orientation distribution functions, (b) the concept and detailed algorithm proposed to solve the problems, (c) implementation and results of the experiments with digital simulations and *in vivo* data,

and (d) discussion of factors that may possibly affect the transformation results and the limitations of this algorithm.

Introduction

Diffusion MRI is a useful tool to study the structure and organization of human brain white matter. Due to anatomical differences between individual brains, spatial normalization of the data is usually needed to make comparisons between subjects, especially for voxel-based analysis. However, simple normalization of diffusion weighted (DW) images is not sufficient to retain the orientation information of the underlying structure. The preservation of principal direction (PPD) algorithm (69,70) has been proposed to rotate the diffusion tensor so that the principal directions of the tensor are preserved relative to local anatomical structures. This algorithm is limited since it is based on the tensor model which is not able to resolve multiple fibers within a voxel. In addition, the rotation does not account for possible shearing and isotropic scaling effects. Compared with diffusion tensor imaging, high angular resolution diffusion imaging is able to provide more accurate estimates of the distribution of fiber orientations within a voxel. However, effective spatial normalization of HARDI data has not yet been demonstrated. Figure 16 illustrates the limitations of the PPD algorithm.

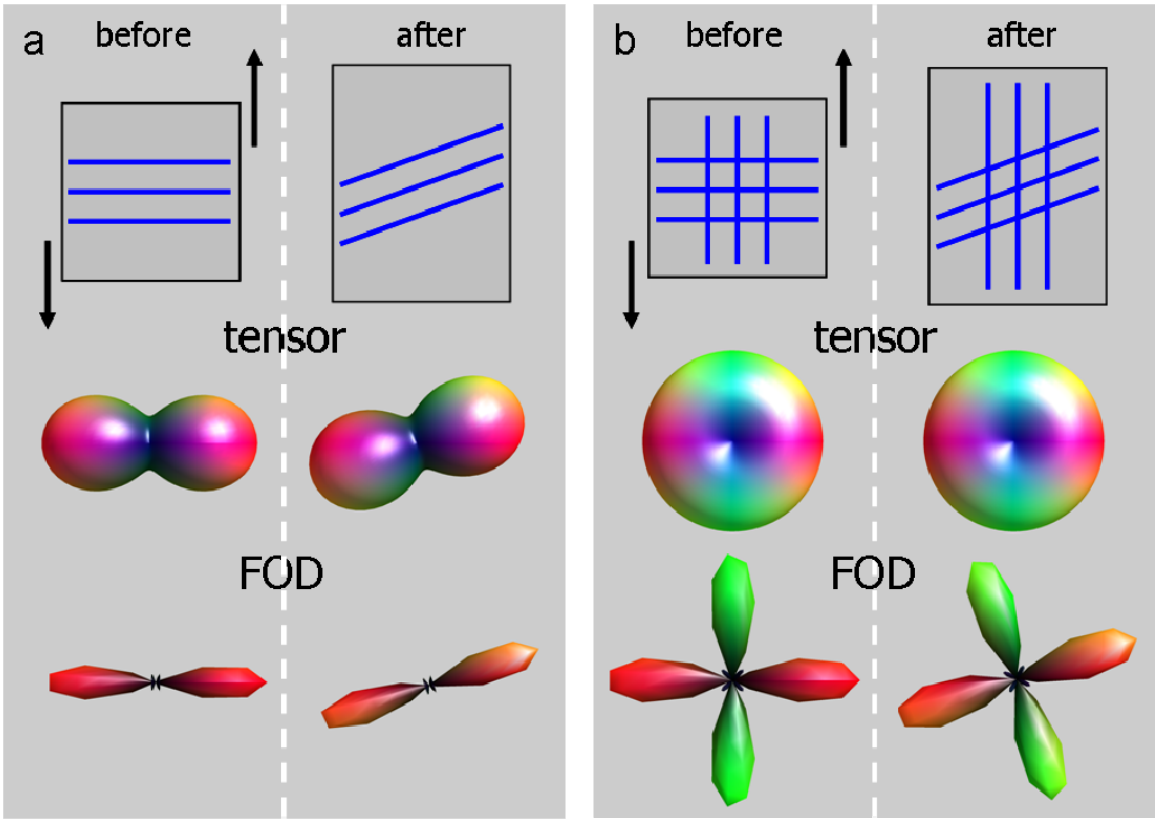

Figure 16. Illustration of the limitations of the PPD algorithm. (a). an example of a single-fiber voxel before and after a vertical shearing effect. (b) a voxel with two perpendicular fibers before and after the same vertical shearing effect. In each panel, the top row shows the simulated intravoxel fiber structure. The middle row shows the tensors before and after the PPD transformation. The bottom row shows the FORECAST FODs before and after the PPD transformation. The PPD algorithm inappropriately rotates the entire FOD in (b).

In this study we propose an algorithm to transform the FOD function based on HARDI data, taking into account not only translation, but also rotation, scaling, and shearing effects. The algorithm is tested with transformations of both simulated data and *in vivo* human data.

Methods

FOD transformation

The FOD derived from spherical deconvolution methods (52-54) is a function on the unit sphere. The peaks of the FOD provide information about the underlying fiber components. The orientation of each peak indicates the orientation of a fiber, and the magnitude of each peak is proportional to the volume fraction of the corresponding fiber. When sampled in a number of directions evenly distributed over a sphere, the FOD function can be approximated by the values it takes in those directions. This can be represented by a set of sampling vectors, the lengths of which represent the fiber volume fractions along the corresponding directions.

From the deformation field that registers the DW images, a Jacobian matrix $\tilde{J}$ can be derived for each voxel, which represents the local deformation at that point. The path taken by a fiber through the voxel can be approximated by a series of line segments, written $d\vec{r}_i = [dx_i, dy_i, dz_i]^T$ for the i^{th} segment. Under the local deformation, these segments transform to $d\vec{r}_i' = J \cdot d\vec{r}_i$. Since every fiber passing through the voxel is subject to the same Jacobian, the FOD must also be transformed using $\tilde{J}$. Applying $\tilde{J}$ to the sampling vectors of the corresponding FOD will give the new orientations of these vectors, and hence a discrete approximation of the transformed FOD.

The integral of the FOD over a unit sphere equals to 1, which is a basic property of a distribution function, and should be retained after transformation. The value of the

FOD at polar angle θ and azimuthal angle ϕ is written $P(\theta,\phi)$. The volume fraction of fibers with orientation near (θ,ϕ) equals $P(\theta,\phi)\cdot d\Omega$, where $d\Omega = \sin\theta d\theta d\phi$ is the element of solid angle describing the neighborhood (see Figure 17). The volume fraction of fibers oriented toward this small patch $d\Omega$ must remain the same after the patch is transformed:

$$P(\theta,\phi)d\Omega = P'(\theta',\phi')d\Omega' \tag{4}$$

where the unprimed and primed symbols represent the corresponding quantities before and after transformation, respectively. Equivalently,

$$P(\theta,\phi)\sin\theta d\theta d\phi = P'(\theta',\phi')\sin\theta' d\theta' d\phi' \tag{5}$$

Therefore, the length of the transformed vectors should be adjusted to guarantee that:

$$P'(\theta',\phi') = P(\theta,\phi)\frac{\sin\theta d\theta d\phi}{\sin\theta' d\theta' d\phi'} \tag{6}$$

According to the substitution rule for multiple variables,

$$d\theta' d\phi' = \left|\det(\tilde{J}_\Omega)\right| d\theta d\phi \tag{7}$$

where $|\cdot|$ denotes absolute value, $\det(\cdot)$ denotes the determinant, and

$$\tilde{J}_\Omega = \begin{bmatrix} \frac{\partial\theta'}{\partial\theta} & \frac{\partial\theta'}{\partial\phi} \\ \frac{\partial\phi'}{\partial\theta} & \frac{\partial\phi'}{\partial\phi} \end{bmatrix} \tag{8}$$

which is the Jacobian of the angular transformation from (θ,ϕ) to (θ',ϕ'). Substituting this relation into Eq.(6), we have

$$P'(\theta',\phi') = P(\theta,\phi)\frac{\sin\theta}{\sin\theta'}\frac{1}{\left|\det(\tilde{J}_\Omega)\right|} \tag{9}$$

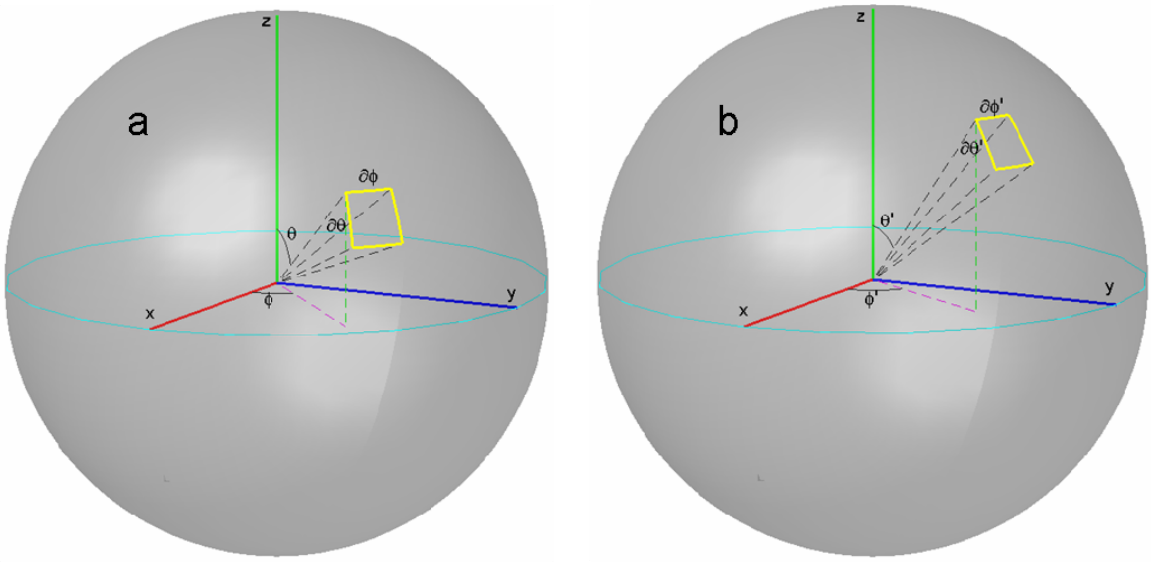

Figure 17. A small patch on the unit sphere before (a) and after (b) transformation, with solid angles $d\Omega = \sin\theta d\theta d\phi$ and $d\Omega' = \sin\theta' d\theta' d\phi'$, respectively.

To calculate $\widetilde{J}_\Omega$, let $r = P(\theta,\phi)$ and $r' = P'(\theta',\phi')$ be the FOD magnitudes along the original direction (θ,ϕ) and the corresponding transformed direction (θ',ϕ'), respectively. Since $\widetilde{J}$ is most naturally expressed as a 3×3 matrix in Cartesian space, we must convert from spherical to Cartesian coordinates,

$$\begin{cases} x = r\sin\theta\cos\phi \\ y = r\sin\theta\sin\phi \\ z = r\cos\theta \end{cases} \tag{10}$$

before applying the spatial normalization Jacobian $\widetilde{J}$, then convert the results back to spherical coordinates,

$$\begin{cases} r' = \sqrt{x'^2 + y'^2 + z'^2} \\ \theta' = \cos^{-1}\left(\dfrac{z'}{r'}\right) \\ \phi' = \tan^{-1}\left(\dfrac{y'}{x'}\right) \end{cases} \tag{11}$$

The Jacobians of these two transformations are

$$\widetilde{J}_1 = \begin{bmatrix} \dfrac{\partial x}{\partial r} & \dfrac{\partial x}{\partial \theta} & \dfrac{\partial x}{\partial \phi} \\ \dfrac{\partial y}{\partial r} & \dfrac{\partial y}{\partial \theta} & \dfrac{\partial y}{\partial \phi} \\ \dfrac{\partial z}{\partial r} & \dfrac{\partial z}{\partial \theta} & \dfrac{\partial z}{\partial \phi} \end{bmatrix} = \begin{bmatrix} \sin\theta\cos\phi & r\cos\theta\cos\phi & -r\sin\theta\sin\phi \\ \sin\theta\sin\phi & r\cos\theta\sin\phi & r\sin\theta\cos\phi \\ \cos\theta & -r\sin\theta & 0 \end{bmatrix} \tag{12}$$

and

$$\widetilde{J}_3 = \begin{bmatrix} \dfrac{\partial r'}{\partial x'} & \dfrac{\partial r'}{\partial y'} & \dfrac{\partial r'}{\partial z'} \\ \dfrac{\partial \theta'}{\partial x'} & \dfrac{\partial \theta'}{\partial y'} & \dfrac{\partial \theta'}{\partial z'} \\ \dfrac{\partial \phi'}{\partial x'} & \dfrac{\partial \phi'}{\partial y'} & \dfrac{\partial \phi'}{\partial z'} \end{bmatrix} = \begin{bmatrix} \dfrac{x'}{r'} & \dfrac{y'}{r'} & \dfrac{z'}{r'} \\ \dfrac{x'z'}{\sqrt{x'^2 + y'^2}\cdot r'^2} & \dfrac{y'z'}{\sqrt{x'^2 + y'^2}\cdot r'^2} & \dfrac{-\sqrt{x'^2 + y'^2}}{r'^2} \\ \dfrac{-y'}{x'^2 + y'^2} & \dfrac{x'}{x'^2 + y'^2} & 0 \end{bmatrix} \tag{13}$$

respectively. The total transformation consists of 3 parts:

$$[r,\theta,\phi] \xrightarrow{\widetilde{J}_1} [x,y,z] \xrightarrow{\widetilde{J}_2 = \widetilde{J}} [x',y',z'] \xrightarrow{\widetilde{J}_3} [r',\theta',\phi'] \tag{14}$$

so that

$$[r,\theta,\phi] \xrightarrow{\widetilde{J}_{\text{total}}} [r',\theta',\phi'], \text{ where } \widetilde{J}_{\text{total}} = \widetilde{J}_3 \cdot \widetilde{J}_2 \cdot \widetilde{J}_1 = \begin{bmatrix} \dfrac{\partial r'}{\partial r} & \dfrac{\partial r'}{\partial \theta} & \dfrac{\partial r'}{\partial \phi} \\ \dfrac{\partial \theta'}{\partial r} & \dfrac{\partial \theta'}{\partial \theta} & \dfrac{\partial \theta'}{\partial \phi} \\ \dfrac{\partial \phi'}{\partial r} & \dfrac{\partial \phi'}{\partial \theta} & \dfrac{\partial \phi'}{\partial \phi} \end{bmatrix} \tag{15}$$

Therefore, for a direction (θ,ϕ), the angular Jacobian, $\widetilde{J}_\Omega$, of the total transformation to (θ',ϕ') is given by the lower right 2×2 part of $\widetilde{J}_{\text{total}}$.

In summary, the transformation of an FOD is performed in 4 steps:

1. A Jacobian matrix $\tilde{J}$ for each voxel is derived from the deformation field of the spatial normalization transformation applied to the DW images.
2. Each FOD is represented by a number of sampling vectors evenly distributed over a sphere. For each sampling vector, $\tilde{J}$ is applied to transform the orientation from (θ,ϕ) to (θ',ϕ').
3. For each sampling vector, $\left|\det(\tilde{J}_\Omega)\right|$ is calculated for the pair of directions (θ,ϕ) and (θ',ϕ'), and the length of the vector is adjusted according to Eq.(9).
4. Finally, the transformed FOD is approximated by the set of transformed, length-adjusted sampling vectors.

Note that noise and truncation artifacts may cause the FOD to have negative values along some orientations. These negative vectors are transformed in the same way as positive vectors in order to maintain the unit integral of $P(\theta,\phi)$.

Numerical simulations

The proposed algorithm was tested using numerical simulations. Four intravoxel fiber structures with crossing angle varying from 0º to 90º were chosen. The corresponding FODs were simulated using the FORECAST spherical deconvolution method (54) through 6th order. Two transformations were applied to the FODs: a horizontal stretch

$\begin{bmatrix} 1.5 & 0 & 0 \\ 0 & 1 & 0 \\ 0 & 0 & 1 \end{bmatrix}$ and a vertical shear $\begin{bmatrix} 1 & 0 & 0 \\ -\tan(\frac{\pi}{10}) & 1 & 0 \\ 0 & 0 & 1 \end{bmatrix}$ (see Figure 18 part a). The integrals of the transformed FODs were tested against the expected value 1. Performance was evaluated by the angular error between the peaks of the transformed FODs and the true transformed fiber orientations. Four different numbers of sampling points, 92, 252, 1002, and 4049, all generated by icosahedral tessellation of the unit sphere (71), were tested in each case.

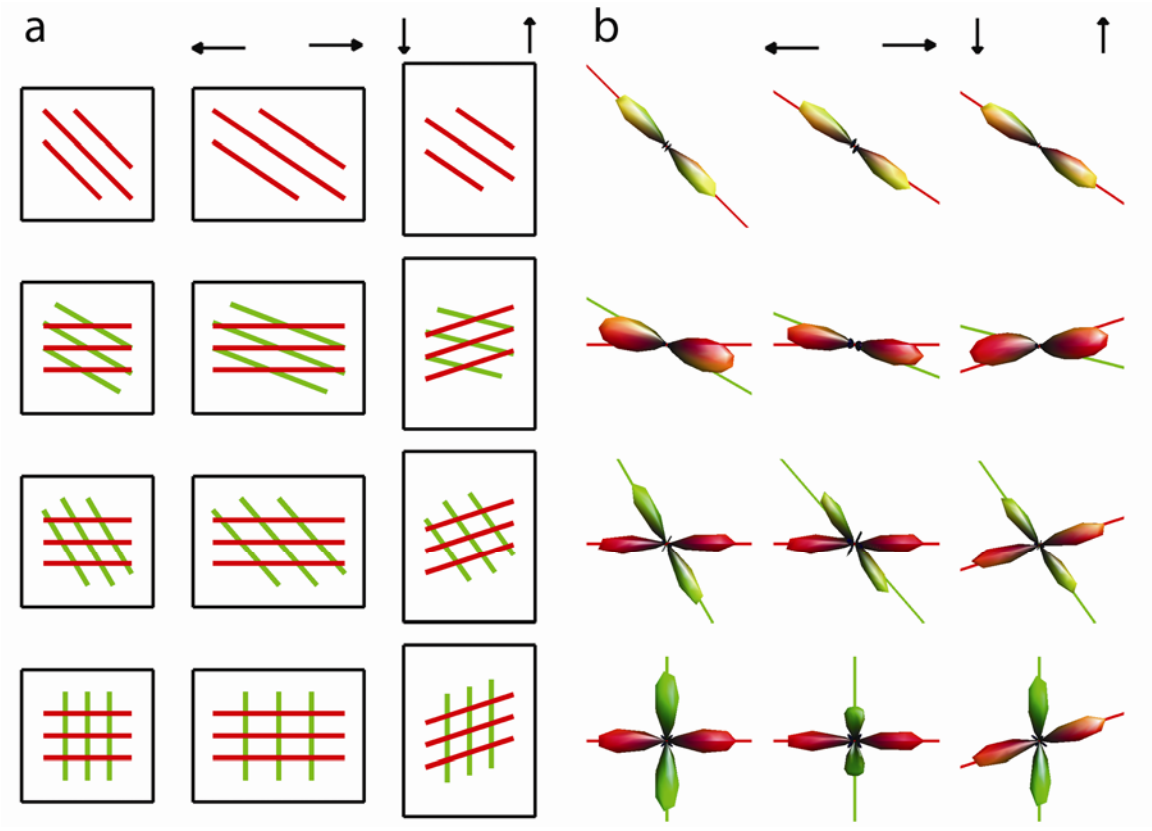

Figure 18. Simulated intravoxel fiber structures (a) and the corresponding FODs (b). (a). From top to bottom the crossing angle between fibers increases from 0º to 30º, 60º, and 90º. The Left column gives the original fiber structure. The middle and right columns illustrate the fiber structures after a horizontal stretch and a vertical shear, respectively (denoted by the black arrows). (b). Corresponding FODs with the true fiber orientations plotted in the solid lines.

Image acquisition and registration

In addition to numerical simulations, this algorithm was also tested by transformation of *in vivo* human data. Two intra-subject experiments and one inter-subject experiment were performed. All scanning procedures were approved by the Vanderbilt University Institutional Review Board and performed on a Philips Intera Achieva 3T scanner. High-performance gradient coils (80 mT/m gradient strength and 100 mT/m/ms slew-rate) and an 8 channel SENSE head coil were used. In the first intra-subject experiment, a healthy subject rotated his head in the scanner between scans, first around the left-right, then around the superior-inferior axis. HARDI images were acquired (by single-shot EPI and SENSE) in all the three head positions, using the following imaging parameters: b=1000s/mm^2, 92 diffusion-sensitizing directions (the 46 directions given by 3rd order icosahedral tessellation of a sphere (71) and their opposites), $\mathrm{TE} = 48\mathrm{ms}$, $\mathrm{TR} = 10{,}000\mathrm{ms}$, SENSE factor $= 3$, $96 \times 96 \times 53$ matrix size, and 2.5mm isotropic voxel size. For each head orientation, high resolution T_2-weighted (T_2-W) images (TE = 80 ms, TR = 6000 ms, $512 \times 512 \times 53$ matrix size, $0.45 \times 0.45 \times 2.5$ mm voxel size) were also obtained with a turbo spin echo sequence at the same slice positions for registration purposes. The total imaging time was about 1 hour. A second intra-subject experiment was performed on another healthy subject using the same imaging parameters, but data were collected in only two head orientations which differed by rotation around the anterior-posterior axis. For the inter-subject experiment, HARDI images were acquired

from a group of 23 schizophrenia outpatients and 20 healthy controls using the following imaging parameters: b=1000s/mm^2, 92 diffusion-sensitizing directions, $\mathrm{TE} = 48\mathrm{ms}$, $\mathrm{TR} = 10{,}000\mathrm{ms}$, SENSE factor $= 3$, $96 \times 96 \times 55$ matrix size, and 2.5mm isotropic voxel size. High resolution T_2-W images ($\mathrm{TE} = 80\mathrm{ms}$, $\mathrm{TR} = 6{,}000\mathrm{ms}$, $512 \times 512 \times 55$ matrix size, $0.45 \times 0.45 \times 2.5$ mm voxel size) and T_1-weighted (T_1-W) images (using a multi-shot gradient echo sequence with $\mathrm{TE} = 4.6\mathrm{ms}$, $\mathrm{TR} = 8.9\mathrm{ms}$, SENSE factor $= 2$, $256 \times 256 \times 176$ matrix size, $1 \times 1 \times 1$ mm voxel size) were also obtained for registration purposes. Eddy current distortion correction (72) was performed on each set of HARDI images prior to further analysis.

The $b = 0$ images in each HARDI data set have higher image contrast than the individual DW images, therefore they were used in the image normalization process and the resulting transformation was then applied to the DW images for each diffusion direction. Image normalization for each experiment was performed in a series of steps, involving registration of the $b = 0$ images to their corresponding anatomical image volumes and then registration of the anatomical volumes to a common image space. Both linear (73) and nonlinear (74) registration algorithms were used. The process for each experiment is described below.

For the intra-subject experiment with three head positions, one head position was designated as the target to which the remaining positions (denoted as source images) were registered through the following steps. First, the $b = 0$ images for each head position were registered to the corresponding high resolution T2-W volume by a non-linear

transformation, initialized using parameters from rigid registration between the two image sets. Then a similar two-step transformation was carried out between the T2-W images of each source and the target. Finally, the two transformations between the source $b = 0$ images and the source T2-W images, the two transformations between the source T2-W images and the target T2-W volume, and the inverse of the two transformations between the target $b = 0$ images and the target T2-W volume were combined to form the total transformation between the source $b = 0$ images to the target $b = 0$ images. The $b = 0$ images from the two head positions in the second intra-subject experiment were co-registered in the same manner, where one position was selected as the target, and the other position was the source image.

The data collected for the inter-subject experiment were originally co-registered for use in a voxel-based analysis of fractional anisotropy measures derived from a diffusion tensor analysis of the HARDI data. The normalization process consisted of two main steps: creation of a study-specific FA template and co-registration of the individual FA maps to the FA template. This was done in an attempt to minimize potential bias in the normalization results due to selecting a single subject as the target image. The study-specific template was created by a set of 3 registration steps. First, nonlinear registration, initialized by rigid registration, between the $b = 0$ images of each subject and the corresponding high-resolution, slice matched T2-W images was performed to reduce image distortion due to susceptibility artifacts. Second, rigid registration between the T2-W images and T1-W images of each subject was performed.

Third, nonlinear registration, initialized by rigid registration, between the T1-W images of each subject and the T1-W image volume of a target subject (chosen from the control group) was performed. The resulting transformations were combined to create a single transformation for each subject, which was applied to the subject's FA map. The normalized FA maps from all subjects were averaged to create the study-specific template. Finally, each subject's original FA map was then registered to the FA template through both rigid registration with scaling and nonlinear registration. The resulting transformations were combined to create the transformation applied to the DW images in this study. Compared to simpler schemes, this multistep approach was found to provide more robust inter-subject registration (for more details see (75)).

In each experiment, the total transformation was applied to the DW images for each diffusion direction. Based on the transformed HARDI images, FODs were calculated using the FORECAST spherical deconvolution method through 6^{th} order. To reduce the effects of noise, the FODs were regularized by minimizing the negative values (59) with a fixed weighting factor (α=0.3, which was chosen to optimize reproducibility based on Monte Carlo simulations). The Jacobian matrix for each voxel was calculated based on the deformation field of the total transformation, and was used to transform the FODs as described above. For the intra-subject experiments, the FODs in the target image, and in the transformed source image before and after adjusting the FOD orientation and shape were compared. The similarity between two FODs was evaluated by the angular correlation coefficient and the root mean square (RMS) error of the

point-wise FOD values. For the inter-subject experiment, the transformed FODs from different subjects were compared. The mean and standard deviation of the transformed FODs over the control group (excluding the target subject) were derived, and the ACC and RMS error for each subject relative to the group mean were also calculated.

Results

Simulation results demonstrate the ability of the proposed method to handle non-rigid transformations in spatial normalization which can not be fully accounted for by a simple rotation. The transformed FOD is able to provide reliable estimates of the transformed fiber orientation when the number of sampling points is sufficient. In our test, 92 sampling points gives poor performance in terms of high angular error and large deviation from the unit integral. When the number increases to 252 and above, the angular error drops to acceptable levels (for example, a mean error of 5º in the horizontal stretch of the 60º-crossing case), and the unit integral is preserved. There is no significant difference in the angular accuracy achieved when the number of sampling points increases beyond 252. Parts of the simulation results are shown in Figure 18.

An example of the intra-subject transformation is shown in Figure 19. It is obvious that the FODs derived from the transformed HARDI images maintain their orientations in the original source image, and do not agree with the fiber tracts in the target image. After transformation, the FODs indicate the correct orientation of the

corpus callosum and the cingulum bundle, and the similarity to the corresponding target FODs becomes higher. The mean ACC across all the white matter voxels in the slice is raised from 0.53 before transformation to 0.70 after transformation. The mean RMS error is lowered from 0.26 to 0.20. Figure 20 shows an example of different fiber tracts (the right internal capsule) and rotation axis from the other intra-subject transformation, where the mean ACC increases from 0.56 before transformation to 0.78 after transformation and the mean RMS error decreases from 0.25 to 0.17.

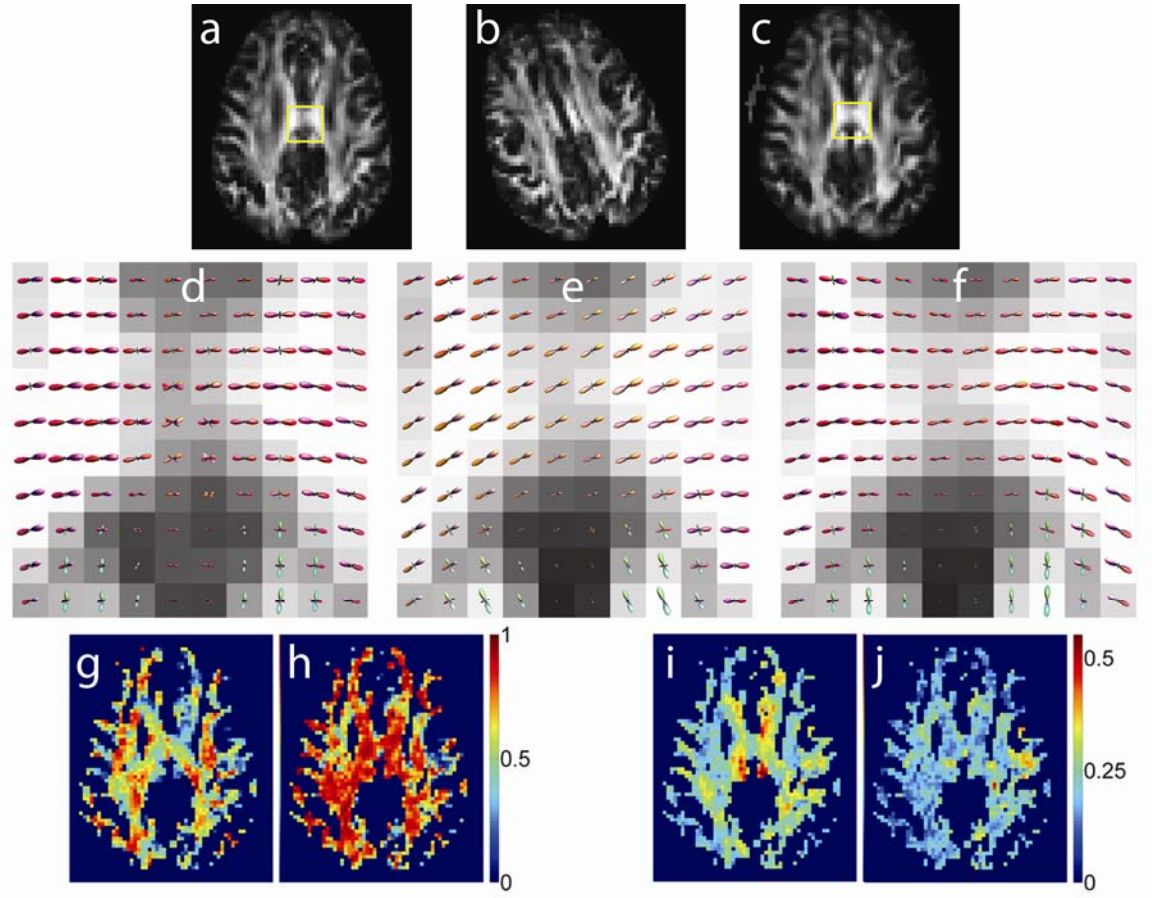

Figure 19. Example of intra-subject normalization of data acquired after in-plane head rotation. The FA is shown in one slice of the target (a), source (b), and transformed source (c) datasets. FODs in the ROI (highlighted in the yellow box) overlaid on the FA map in the target image (d), in the transformed image before (e) and after (f) FOD transformation. ACC between source and target FODs before (g) and after (h) transformation. RMS error with respect to the target FODs for the source FOD before (i) and after (j) transformation. Note that a white matter mask was applied (FA $\geq$ 0.25). The size of each FOD is scaled by the corresponding FA value.

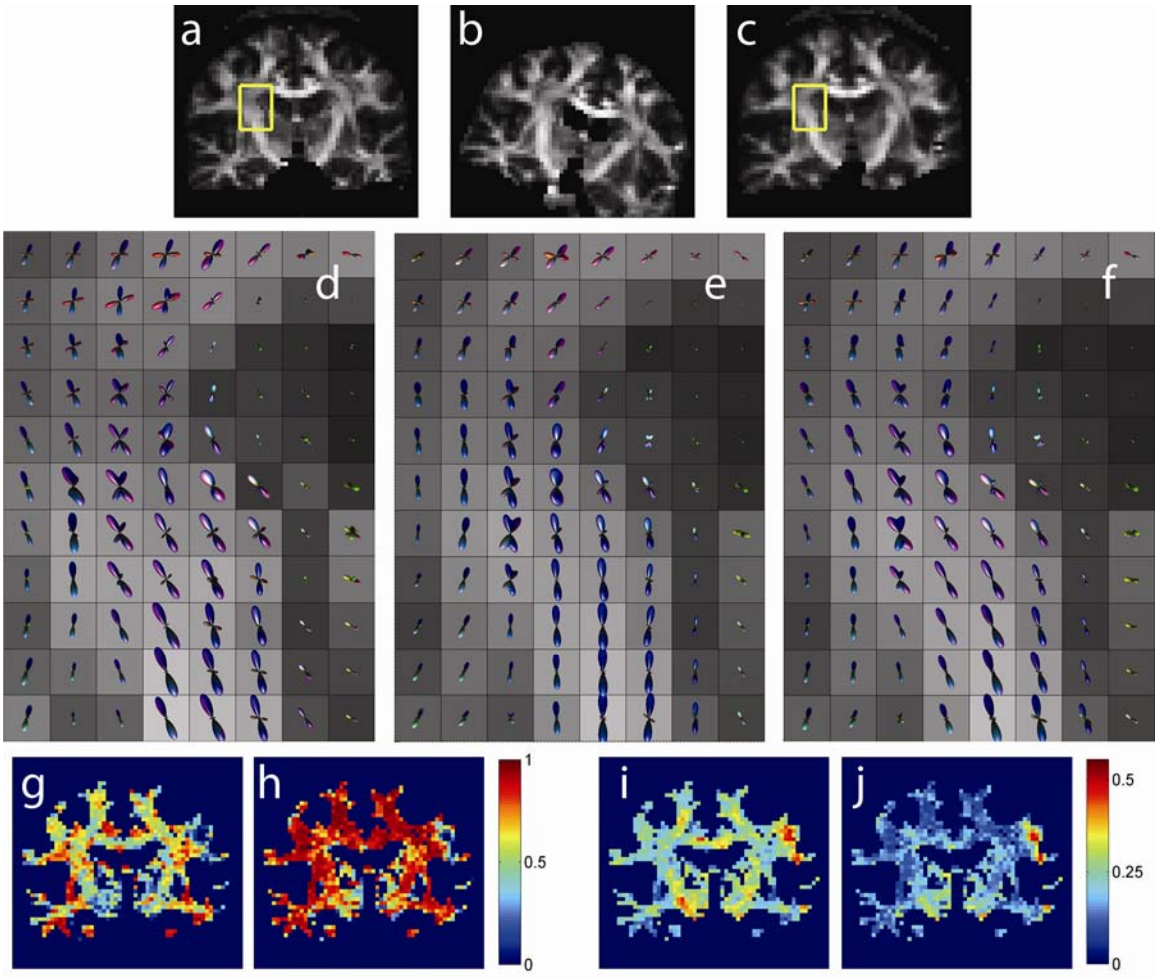

Figure 20. Example of intra-subject normalization of data acquired after through-plane head rotation. The FA is shown in one coronal slice of the target (a), source (b), and transformed (c) image. Note that images were acquired axially. FODs in the ROI (highlighted in the yellow box) overlaid on the FA map in the target image (d) and in the source image before (e) and after (f) FOD transformation. ACC between source and target FODs before (g) and after (h) transformation. RMS error with respect to the target FODs for the source FODs before (i) and after (j) transformation. Note that a white matter mask was applied (FA $\geq$ 0.25). The size of each FOD is scaled by the corresponding FA value.

The transformation results between subjects are demonstrated in Figure 21 and 22. Figure 21 compares the FODs along part of the left cingulum from two subjects before and after transformation. It is clear that the FODs derived from the transformed DW

images without adjustment still take the orientation of the fiber before registration, not the transformed fiber. After transformation, the FODs are more consistent with the transformed cingulum bundle.

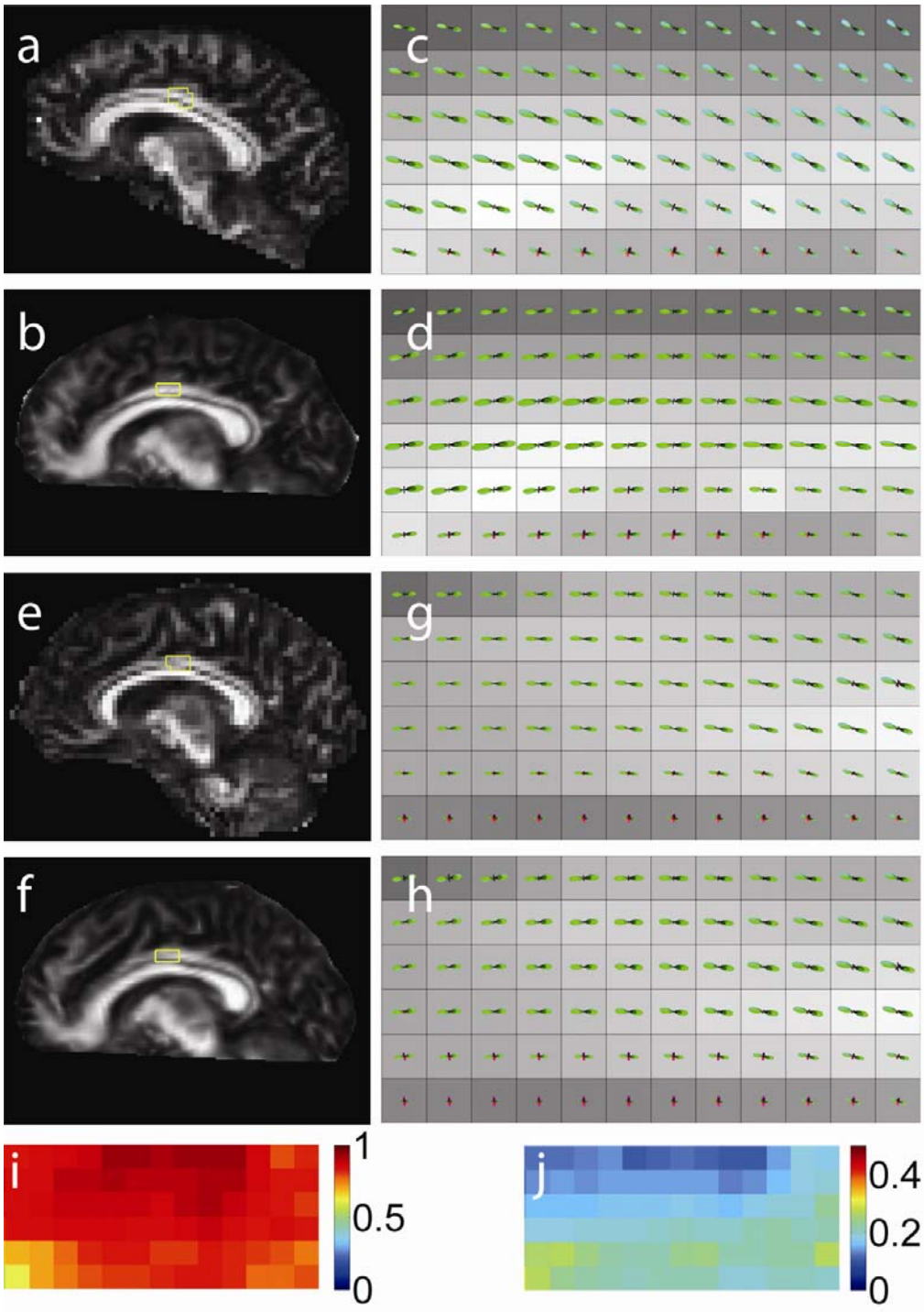

Figure 21. Example of inter-subject normalization. (a)-(d): results for subject A. FA map in the native (a) and common (b) space, with corresponding ROI highlighted in the yellow box. FODs in the ROI before (c) and after (d) transformation, overlaid on the FA map. (e)-(h): results from subject B in the same ROI: native (e) and common (f) space FA maps and ROI FODs before (g) and after (h) transformation. The similarity between subject A and B FODs in the ROI is shown in ACC (i) and RMS deviation (j) maps. The size of each FOD is scaled by the corresponding FA value.

Figure 22 shows the mean and standard deviation of the transformed FODs over the control group of 19 subjects. The region of interest (ROI) was chosen to include voxels containing single fiber and multiple fiber orientations. The variation of the transformed FODs across subjects is small, but relatively higher at the boundary between white matter and cerebrospinal fluid, or the boundary between two distinct fiber bundles.

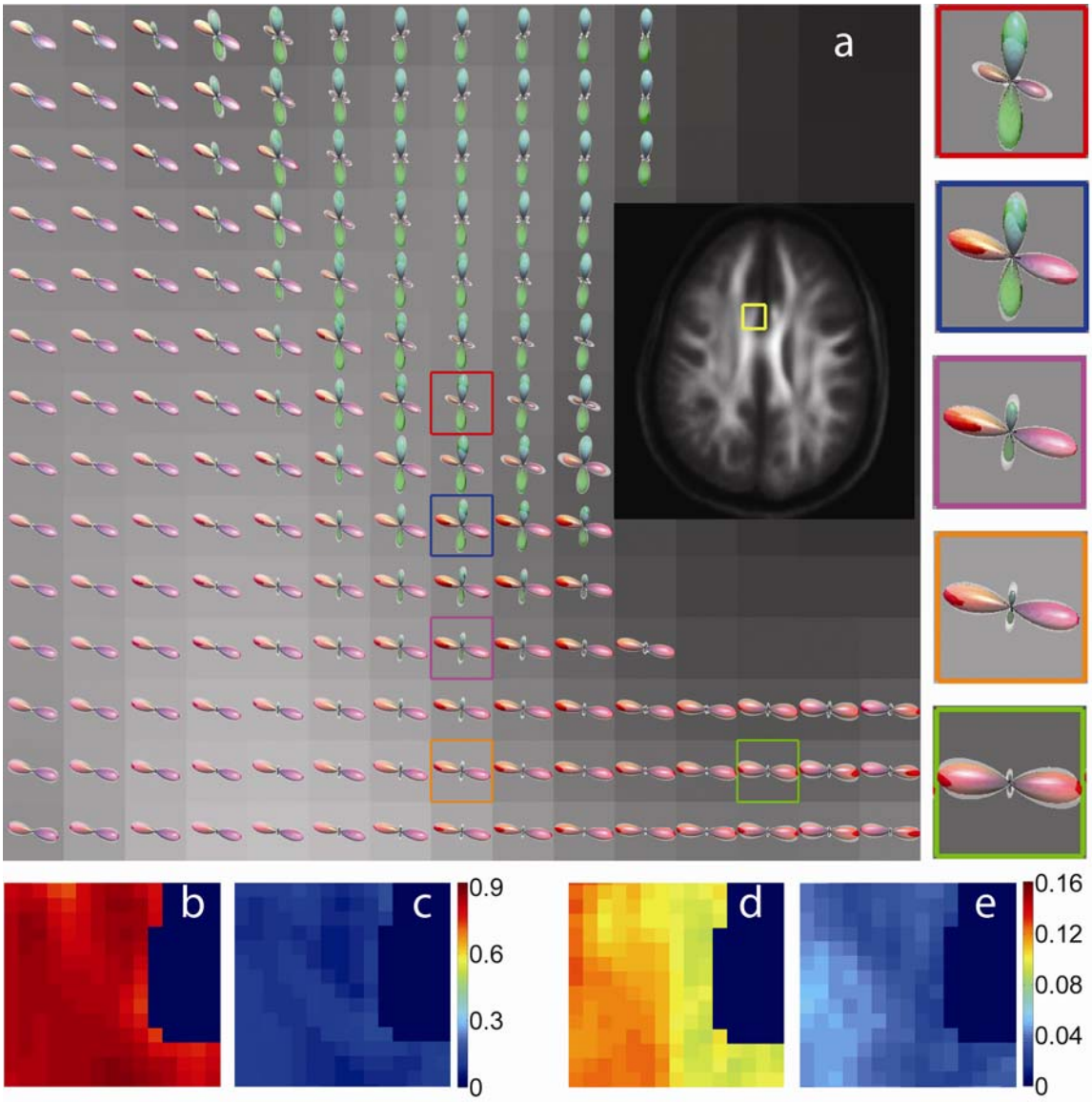

Figure 22. Example of group data transformed to the common space. (a): The mean (opaque) and mean+std (transparent) FODs over a group of 19 subjects normalized to a common space. The inset shows the ROI (yellow box) in the averaged FA map and enlarged FODs from 5 representative voxels highlighted in colored boxes. The mean (b) and std (c) ACC maps in the ROI were calculated across all subjects (relative to the group mean FOD). The mean (d) and std (e) RMS error maps are also shown. Note that in all cases a white matter mask was applied (averaged FA $\geq$ 0.25).

Discussion

Spatial normalization of brain MR images, especially those between subjects, usually involves scaling and shearing due to anatomic differences between individual brains. These factors, in addition to the relatively simple case of rotation, may change not only the orientation, but also the overall shape of the fiber orientation distribution within an imaging voxel. Therefore, it is necessary to take into account scaling and shearing effects in order to obtain accurate transformed FODs. This is demonstrated by the numerical simulations and the high similarity achieved in our between-subject normalization results.

Recently Chiang and coworkers proposed a fluid registration method for HARDI data, in which the principal direction of the diffusivity function is estimated using principal component analysis, and its reorientation is performed using a rotation derived from the PPD algorithm (76). This method is limited in that the principal direction of the diffusivity function is not able to fully describe multiple fiber orientations within a voxel. Also, a rotation is not sufficient to represent the non-rigid transformations involved in the normalization process. By contrast, the algorithm proposed in our study not only takes advantage of HARDI data by working on the FOD functions, but also successfully addresses the problem of non-rigid deformation.

Although the normalization algorithm was demonstrated using the FOD derived from the FORECAST model, the method is applicable to FOD functions derived from other spherical deconvolution approaches as well. Similarly, the orientation distribution

function (ODF) derived from Diffusion Spectrum Imaging (28,44) or Q-Ball imaging (29) gives the probability that spin displacement lies in a particular direction. This is also an angular distribution function on the unit sphere that can be transformed according to the proposed method.

For simple spatial normalization where only rigid rotation is involved, the reorientation of the FOD function can be achieved in two ways: calculating the FOD based on rotated diffusion gradient directions, or simply rotating the FOD calculated using the original gradient directions. These two are equivalent because the relationship between the FOD and measured DW signal is linear and shift-invariant, where shifts on a sphere are equivalent to rotations. For non-rigid spatial transformation, however, the first approach does not work even if the original deconvolution kernel is used (results not shown). This is because non-rigid transformations are not shift-invariant on the unit sphere and therefore do not preserve the convolution relationship between the FOD and measured signal. Similarly, transforming the diffusion gradient directions does not give the correctly transformed ODF of QBI, since non-rigid transformation does not preserve Funk-Radon transform relationships.

Since the FOD function is expressed in terms of spherical harmonic expansion coefficients, the highest expansion order determines its angular resolution. One factor that will possibly affect the accuracy of the transformed FOD is the SH expansion order. Due to the scaling and shearing effects possibly included in the image registration process, especially for inter-subject cases, the transformed FOD may take a different shape (for

example, a narrower peak), which may require higher order SH expansion in order to be fully described. Insufficient SH order may lead to error in both the shape and orientation of the resulting FOD. In this case, expressing the FOD through a higher order may be helpful. Take the example in the simulation study where a voxel with two fibers crossing at 60º undergoes a stretch (see Figure 18 part b row 3 column 2) and results in a smaller crossing angle. The transformed FOD fitted through 6^{th} order gives a mean angular error of 4.6º, which is reduced to 1.5º when fitted through 8^{th} order. Note that a higher SH order can provide higher angular resolution at the cost of introducing high frequency noise (which may also affect the accuracy of FODs), somewhat longer computational time and larger data storage space. The optimal SH order depends on both the original fiber configuration and the nature of the spatial normalization. Here in our *in vivo* data, we chose to use the same SH order for both the target and transformed FODs in order to facilitate the comparison between them.

The number of sampling points is another factor that may affect the accuracy of the transformation algorithm. According to the simulations, 252 sampling points evenly distributed over a unit sphere are able to achieve satisfactory results. A higher number improves the performance slightly, but at the cost of longer computation time.

Although the transformation is successful in most voxels (high similarity between the transformed source and the target FODs), there are some regions where the transformation is less accurate. One example is the small lateral region in the left hemisphere (right side of the image) in Figure 19 (see part j, for example), where the

ACC between the transformed source and target FODs is relatively low and the RMS error is relatively high. The low similarity stems from shape and orientation differences between the FODs: the target FODs clearly show two fiber components with different orientations, while most of the original and transformed source FODs contain only one fiber along the mean orientation of the two fibers in the target image (details not shown here). Generally speaking, the discrepancy could result from three possible causes. It may be due to any one of them, or more likely, a combination of some or all of them. First, FODs from either the target or the source image or both might not be reliable due to limitations of the FORECAST model. This model assumes a single radial diffusivity for all fibers within a voxel (i.e., a single kernel for spherical deconvolution within a voxel) (54). Violation of this assumption may cause errors in the estimated fiber volume fractions. Based on simulations, the error could be about 25% at the current SNR level of 30~50 under the imaging protocols used in this study (results not shown). Also, errors in the estimated FOD may be due to noise or image artifacts, which were not completely removed by the eddy current distortion correction and the regularization process. Since interpolation is involved in the image registration process, the transformed image is in fact spatially smoothed, resulting in a higher SNR level (and partial volume averaging) than the target image, and hence likely requires a smaller regularization weighting factor. Even though the regularization weighting factor was chosen carefully based on Monte Carlo simulations and the chosen value is considered proper for the SNR range here, the fixed value might still under-regularize the target FODs and over-regularize the

transformed FODs. Alternative methods were tested to objectively determine the regularization weighting factor for each voxel, such as the generalized cross validation (GCV) (60) and the L-curve method (57). Both methods gave discrepant results between the target and the transformed source, similar to those using the fixed factor, and none of them gave better overall regularization than the fixed value. A better FOD regularization method will be helpful in the validation of the transformation technique. However, the problem of regularization is beyond the scope of this study.

Second, the discrepancy may come from local image registration errors. Registration based on FA maps (rather than $b = 0$ images) was tested, but this gave similar results. Note that the region in question is at the edge of the brain, containing complex gyral and sulcul structures, which may vary drastically between subjects. This presents a major challenge for accurate registration, even with the sophisticated nonlinear registration method used in this study. The adaptive bases algorithm (74) uses regularly spaced radially symmetric basis functions to model the deformation field and works on a multi-resolution scale, allowing fine adjustments within local regions. The initialization parameters for the algorithm (a total of 14 levels with number of basis functions increasing from 3 to 40 along each dimension) were selected based upon prior experience with the algorithm to provide the best possible match throughout the brain without introducing registration artifacts such as tearing and folding. Close inspection of the corresponding FODs in the target and source images and the neighborhood indicates that this is likely one cause of the FOD discrepancy in this region since transformed FODs

with high similarity to the corresponding target FODs can be found in the near neighborhood (about 1~2 voxels away, details not shown). More advanced image registration methods may improve the results of our method in the future.

Third, the discrepancy may be due to sampling differences between the two acquisitions. For example, consider the possible sandwich-like topology of fiber mixing, which is not positioned exactly in the same way in the target and source image voxels. Suppose one fiber bundle lies inferior to another with different orientation and the mixing area is thin relative to the slice thickness. One axial slice of the target image is centered exactly between the two bundles and thus the FODs fully capture the fiber mixing, while in the source image two neighboring slices happen to lie just superior and inferior to the mixing plane, and thus the FODs in each slice reveal just one of the fiber bundles (as illustrated in Figure 23). In this case, even if the FODs give reliable orientations of the fiber tracts and the image registration is accurate, the transformation algorithm can not provide satisfying results since the source and target FODs contain different fiber populations. Inspection of the neighboring slices indicates that this is likely another cause of the FOD discrepancy in this region (data not shown).

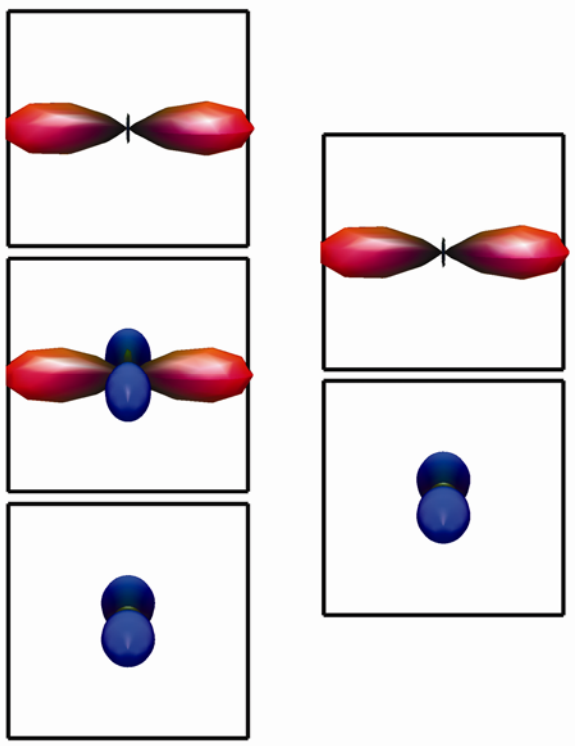

Figure 23. Illustration of the possible FOD sampling differences. Left column: FODs in the target image where the voxel in the middle slice captures the fiber crossing. Right column: FODs in the source image where the neighboring slices miss the fiber crossing.

Conclusion

We developed an algorithm to perform spatial normalization of the FOD function derived from HARDI data, which makes it possible to compare the intravoxel fiber distribution between subjects, between groups, or between two image sets acquired at different time points for the same subject. This is an important step forward from spatial normalization of scalar images and diffusion tensors, since the FOD function derived from HARDI provides more detailed information about intravoxel fiber structure than scalar measures

such as FA, and the diffusion tensor. This technique will likely be helpful in clinical studies that make use of HARDI data to assess white matter disease.

CHAPTER IV

WHITE MATTER ALTERATIONS IN SCHIZOPHRENIA

Overview

Schizophrenia is a severe mental disease affecting about 1% of the population. Previous DTI studies in schizophrenia have reported white matter alterations as measured by changes in fractional anisotropy. However, DTI analysis is not capable of distinguishing between possible causes of these changes. Both intrinsic fiber properties (e.g., axon packing density and myelination) and fiber coherence (the degree to which fibers are parallel within a voxel) influence fractional anisotropy. To distinguish these effects, we performed a group comparison of radial diffusivity and intravoxel fiber coherence estimated by spherical deconvolution analysis of HARDI images, aiming to reveal more details about the white matter abnormalities in schizophrenia.

This chapter includes: (a) a brief introduction to current investigations on schizophrenia using diffusion MRI, (b) our experiment including data acquisition, preprocessing, and analysis, and (c) observed results, discussion and conclusion.

Introduction

Schizophrenia is a severe mental disorder affecting about 1% of the population. Early conventional MRI studies found volume increase in the ventricles and reduction in the frontal and temporal regions in people with schizophrenia (77-79). These findings inspired investigations of anatomic connectivity between these brain regions. In addition, functional studies of the brain revealed multiple cortical and subcortical regions affected by schizophrenia (80-82), suggesting disturbed connections among those functionally related regions. Abnormalities associated with myelin found in postmortem brains (83-85) and genetic studies (86-88) provide further supporting evidence for the hypothesis of white matter involvement in schizophrenia.

Diffusion tensor imaging (2) is a useful tool for non-invasive characterization of the microstructure of white matter. Fractional anisotropy is the most widely used measure to describe white matter integrity in DTI analysis. A number of DTI studies on schizophrenia have reported altered diffusion properties in widespread white matter regions (89-93), as well as some major fiber tracts including the corpus callosum (90,92,94-96), the cingulum bundles (97-99), the arcuate fasciculi (92,96,100,101), the uncinate fasciculi (95,100-102), and the internal capsules (92,96,103,104). However, findings reported in the literature are not consistent regarding the locations, size, and extent of the observed abnormalities, largely due to the complicated and variable nature of this disease, and the differences in the way the data were acquired and analyzed (for a

review, see (105)). Furthermore, many DTI studies are limited by small sample size, low magnetic field strength, low angular resolution, anisotropic voxel size, etc. Most importantly, the underlying mechanism of the altered FA remains unclear since the tensor model is insufficient to distinguish the possible causes, such as a change in the fiber orientation coherence, a change in the intrinsic diffusivity of the fibers, or both. In this study, we aim to address this problem by utilizing more extensive imaging data and more sophisticated analysis methods.

High angular resolution diffusion imaging takes a step forward from diffusion tensor imaging by acquiring diffusion measurements along more directions and reconstructing data by more advanced models, and hence is able to reveal more details of the diffusion process. Fiber orientation estimated using continuous axially symmetric tensors (54) is a HARDI data reconstruction technique based on spherical deconvolution. With an assumption of uniform mean and radial diffusivity for each fiber component within a voxel, the diffusion weighted signal can be expressed as a convolution of the fiber orientation distribution function and the response function from an ideal single fiber. FORECAST is able to recover multiple intravoxel fibers at moderate *b* levels feasible in common clinical protocols. Furthermore, by estimating both the radial diffusivity and fiber orientation distribution in each voxel, FORECAST is capable of distinguishing two different causes of altered FA: fiber coherence or fiber intrinsic diffusivity change. Recently a spatial normalization of the FOD function based on HARDI data was proposed (106), which makes it possible to compare the intravoxel fiber distribution

between subjects in a common space. Utilizing the set of advanced techniques mentioned above, the aim of this work is to reveal more detailed information of the white matter alterations in schizophrenia than conventional DTI is able to provide.

Methods

Subjects

Imaging data were acquired for a group of 33 patients with schizophrenia (SZ) and a group of 22 normal controls (CO). An additional normal subject, who was a 36 year old, right-handed female, was scanned using the same protocol and assigned to be the initial target for image registration, and excluded from group comparison. All patients were on antipsychotic medication at the time of investigation. Informed consent was obtained from each subject, and all scanning procedures were approved by the institutional review board. Datasets of 2 patients were excluded from analysis due to severe movement artifacts, SENSE artifacts, and poor registration (see the section *Image pre-processing and registration* for explanations). The remaining subject's information is summarized in Table 3.

Table 3. Subject demographics.

Feature \ Group		CO			SZ		
		Female	Male	Total	Female	Male	Total
Number		12	10	22	14	17	31
Age (years)	Range	26~53	22~51	22~53	23~54	23~52	23~54
	Mean ± std	36 ± 8	35 ± 10	36 ± 9	44 ± 9	36 ± 9	40 ± 10
Handedness	Left	1	0	1	2	3	5
	Right	11	10	21	12	13	25
	Ambidextrous	0	0	0	0	1	1

Image acquisition

All images were acquired using an 8 channel SENSE head coil on a Philips Intera Achieva 3T scanner with high-performance gradient coils (80 mT/m gradient strength and 100 mT/m/ms slew-rate). A single-shot EPI sequence was used to acquire HARDI images with the following parameters: b=1000s/mm^2, 92 diffusion-sensitizing directions (the 46 directions given by 3rd order icosahedral tessellation of a sphere (71) and their opposites), $\mathrm{TE} = 48\mathrm{ms}$, $\mathrm{TR} = 10{,}000\mathrm{ms}$, $\text{SENSE factor} = 3$, $96 \times 96 \times 53$ matrix size, and 2.5mm isotropic voxel size. For image registration purposes, high resolution T_1-weighted and T_2-weighted images were also obtained for each subject. T_2-weighted images were acquired at the same slice positions as the HARDI images using a turbo spin

echo sequence with the following parameters: $TE = 80ms$, $TR = 6{,}000ms$, $512 \times 512 \times 53$ matrix size, $0.45 \times 0.45 \times 2.5$ mm voxel size. T_1-weighted images were acquired using a multi-shot gradient echo sequence with $TE = 4.6ms$, $TR = 8.9ms$, SENSE factor $= 2$, $256 \times 256 \times 176$ matrix size, $1 \times 1 \times 1$ mm voxel size. The total imaging time for all three scans was about 26 minutes.

Image pre-processing and registration

Prior to further analysis, two pre-processing steps were performed on each set of HARDI images in order to reduce the effects of noise and artifacts. Since the HARDI images in this study were acquired using EPI sequence, they were susceptible to eddy current distortion, especially in the direction of phase encoding (107). Eddy current distortion and bulk subject motion were corrected by registering each diffusion weighted image to the corresponding $b = 0$ image via an affine transformation using an algorithm described by Netsch and van Muiswinkel (72).

Another problem of the EPI acquisition is interference from the extracranial fat signal, which may be incompletely suppressed. The problem may become more severe and affect more brain voxels if parallel imaging techniques, such as SENSE, are employed, as in this study. If fat suppression varies between image volumes (due to diffusion gradient-driven eddy currents, for example), then fat signal aliased into the head can produce high signal variance in the affected voxels. A voxel-wise wild bootstrap

analysis on the FA value was performed. Those voxels in which FA uncertainty (measured as the standard deviation of the re-sampled values) exceeded a user-defined threshold (0.065 for this study) were identified as corrupted by artifacts and excluded from further analysis (more details of this algorithm are described in (75)).

The image registration process consisted of two main steps: creation of a study-specific FA template and co-registration of the individual FA maps to the FA template. This was done in an attempt to minimize potential bias in the normalization results due to selection of a single subject as the target image. The study-specific template was created by a set of 3 registration steps. First, nonlinear registration, initialized by rigid registration, between the $b = 0$ images of each subject and the corresponding high-resolution, slice matched T2-W images was performed to reduce image distortion due to susceptibility artifacts. Second, rigid registration between the T2-W images and T1-W images of each subject was performed. Third, nonlinear registration, initialized by rigid registration, between the T1-W images of each subject and the T1-W image volume of the target subject was performed. The resulting transformations were combined to create a single transformation for each subject, which was applied to the subject's FA map. The normalized FA maps from all subjects were averaged to create the study-specific template. Finally, each subject's original FA map was then registered to the FA template through both rigid registration with scaling and nonlinear registration. The resulting transformations were combined to create the transformation applied to the DW images in this study. Compared to simpler schemes, this multistep approach was found to provide

more robust inter-subject registration. A white matter mask was obtained by applying a threshold of 0.2 to the averaged FA map across all subjects. Statistical analysis was performed on white matter voxels only.

FORECAST analysis

For each subject the total transformation was applied to the DW images for each diffusion direction. Based on the transformed HARDI images, radial diffusivity, $\lambda_{\perp}$, and FOD for each voxel were calculated using the FORECAST spherical deconvolution method. To reduce the effects of noise, the FODs were regularized by minimizing the negative values (59) with a fixed weighting factor (α=0.3, which was chosen to optimize reproducibility based on Monte Carlo simulations). The Jacobian matrix for each voxel was calculated based on the deformation field of the total transformation and was used to transform the FODs as described in (106). Both the pre- and post-transformed FODs were expanded through 6^{th} order spherical harmonics.

To describe the degree of fiber orientation coherence within a voxel, a coherence index, κ, was calculated based on the variance of the eigenvalues of the scatter (i.e., the second moment) matrix of the FOD function (108). The coherence index is a scalar, ranging from 0 to 1. Completely incoherent fiber distributions have $\kappa = 0$, whereas parallel fibers have $\kappa = 1$.

In addition, the number of intravoxel fiber components was determined based on the number of distinct FOD peaks. If the estimated FOD contained more than one peak, and the magnitude of a particular peak was too small relative to the largest one within the same voxel, this peak was considered false, produced by either imaging noise, or contamination from neighboring tissues with isotropic diffusion properties (such as cerebrospinal fluid or gray matter), or truncation artifact from the SH fitting. Those false peaks were ignored. The magnitude ratio threshold was set to 1/5 to best catch the false peaks based on our preliminary results. For voxels with more than one fiber, the crossing angle between the largest two fiber components was also calculated.

To evaluate the quality of the HARDI images, signal to noise ratio was also calculated for each voxel based on the residual sum of squares (i.e., estimating the noise based on the residuals of a 6^{th} order SH fit of the signal as a function of orientation). Then the mean SNR over all white matter voxels was obtained for each subject.

Statistical analysis

T-test was carried out to compare the mean age between the two groups. In addition, z-test was performed to compare gender and handedness. In addition, a voxel wise t-test of group differences in FA was performed in each white matter voxel. The significance level was set at 0.01. In order to further reduce false positive error, a threshold for cluster size of 6 contiguous voxels was applied. In clusters with significant FA differences

between groups, follow-up t-tests on $\lambda_\perp$ and κ were conducted for each voxel, as well as for the mean over each cluster, with the significance level set at 0.05. Furthermore, a general linear model (GLM) between FA, $\lambda_\perp$, and κ was applied for each voxel in those clusters.

In voxels with group difference in fiber coherence, we further tested if there are differences in the number of fibers between groups by performing z-tests on the proportions of single-fiber, two-fiber, and three-fiber voxels. Moreover, we separated the data in each cluster according to the number of fibers, and tested if fiber coherence is different between groups for voxels with the same number of fibers. The threshold for all follow-up tests was set at 0.05.

Results

There are no significant differences in age (p=0.17), gender (p=0.25), or handedness (p=0.095) between the patients and the controls. The HARDI images of the patient group have significantly lower SNR compared with the control group (p=0.0014). The mean and standard deviation of the SNR are 31.21±4.44 for the patients and 34.93±3.59 for the controls, respectively. Significantly lower FA in SZ is found in multiple white matter regions including the right uncinate fasciculus (*unf*), the left corticopontine tract/corticospinal tract (*cpt/cst*), the left posterior limb of internal capsule (*ic*), the posterior part of bilateral interior frontal-occipital/inferior longitudinal fascicules (*ifo/ilf*),

right anterior corona radiata/corpus callosum (*acr/cc*), right forceps major (*fm*), the posterior part of the left superior longitudinal fasciculus (*slf*), the splenium of corpus callosum and adjacent cingulum (*cc/cg*) bilaterally, the left superior corona radiata (*scr*), and the left medial superior part of the anterior/posterior central gyri (*acg*/*pcg*). These locations are shown in Figure 24. Note that clusters that appeared to be affected by artifacts were discarded. One example is the cluster in the inferior genu of the cc (see parts b and c in Figure 24), which is contaminated by cerebrospinal fluid.

In each cluster, the mean radial diffusivity over all voxels is found significantly higher in SZ. All voxels in the left posterior *ifo/ilf*, right *acr/cc*, left *acg/pcg* show significantly elevated $\lambda_{\perp}$, while fewer than half of the voxels in other clusters show significant group difference in $\lambda_{\perp}$. In all regions except for the left posterior *ifo/ilf*, the left posterior *cc/cg*, the left *cpt/cst*, and the left *scr*, the mean fiber coherence is significantly lower in SZ. At the voxel level, only a few voxels in the left *ic*, the right *fm*, the left posterior *slf*, the right posterior *cc/cg*, and the right *unf*, and more than half of the voxels in the left *acg/pcg* exhibit significantly lower κ, no voxel in right posterior *ifo/ilf* and the right *acr/cc* shows significant group differences. Table 4 summarizes the t-test results of all regions at the cluster level.

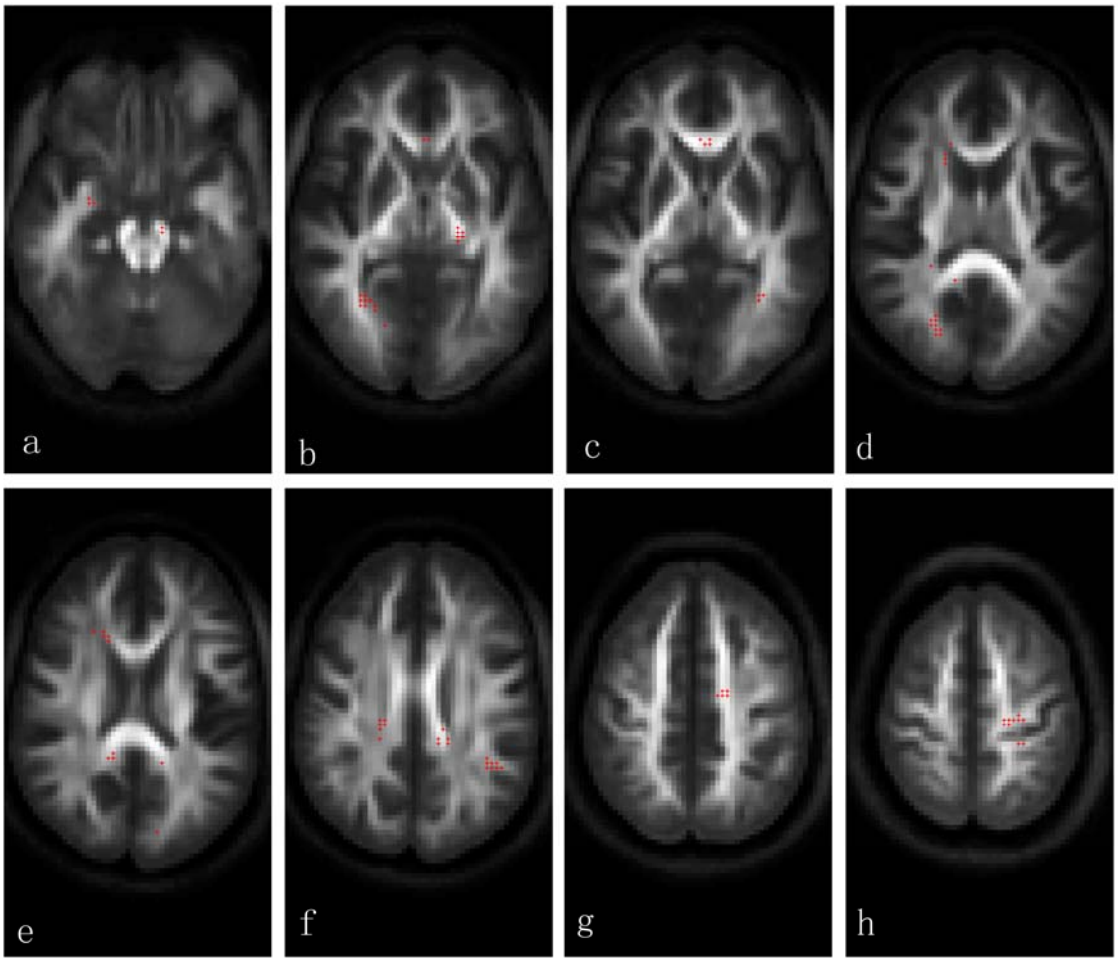

Figure 24. Voxels with significant FA differences between groups are highlighted in red on averaged FA maps. From top to down, and left to right: (a) right uncinate and left corticopontine tract/corticospinal tract, (b) the genu of the corpus callosum, left posterior limb of the internal capsule, and the posterior part of the right interior frontal-occipital/inferior longitudinal fasciculus, (c) the genu of the corpus callosum and the posterior part of the left interior frontal-occipital/inferior longitudinal fasciculus, (d) right anterior corona radiata/corpus callosum, right forceps major, (e) right anterior corona radiata/corpus callosum and bilateral cingulum, (f) the posterior part of the left superior longitudinal fasciculus and the posterior part of bilateral cingulum and adjacent corpus callosum, (g) left superior corona radiata, (h) the left superior medial part of the anterior/posterior central gyri. These slices are not equally spaced.

Table 4. t-test results at the cluster level.

Locations	Cluster size	Mean FA		p(FA)	Mean $\lambda_\perp$ ($10^{-5}cm^2/s$)		p($\lambda_\perp$)	Mean κ		p(κ)
		SZ	CO		SZ	CO		SZ	CO	
l. *ic*	9	0.56	0.59	0.0021	0.48	0.45	0.0065	0.82	0.84	0.0020
l. *ifo/ilf*	7	0.45	0.50	0	0.65	0.57	0.0001	0.84	0.84	0.53
r. *ifo/ilf*	33	0.29	0.35	0	0.81	0.69	0	0.83	0.86	0
r. *acr/cc*	21	0.31	0.35	0	0.65	0.61	0	0.90	0.91	0.0058
r. *fm*	31	0.44	0.52	0	0.53	0.49	0	0.86	0.88	0
l. *slf*	13	0.34	0.40	0	0.55	0.52	0	0.81	0.84	0
l. *cc/cg*	15	0.51	0.55	0	0.52	0.49	0	0.81	0.82	0.64
r. *cc/cg*	30	0.44	0.48	0	0.56	0.53	0	0.85	0.86	0.0002
r. *unf*	7	0.33	0.38	0	0.65	0.62	0	0.81	0.86	0
l. *cpt/cst*	11	0.48	0.53	0	0.51	0.49	0.0047	0.79	0.81	0.12
l. *acg*	19	0.35	0.43	0	0.59	0.49	0	0.84	0.89	0
l. *pcg*	6	0.36	0.45	0	0.56	0.49	0	0.90	0.93	0
l. *scr*	7	0.45	0.50	0	0.50	04.8	0	0.87	0.87	0.69

GLM analysis finds strong correlation between FA and $\lambda_\perp$ at both the voxel and cluster levels in all regions, even after controlling for fiber coherence variation. The

correlation between FA and κ after controlling for $\lambda_\perp$ variation is found to be strong at the cluster level in all regions. At the voxel level, however, only the left posterior *ifo/ilf* , the right *fm*, and the right uncinate fasciculus exhibit significant correlation between FA and κ in all voxels in the cluster, while the right posterior *ifo/ilf* and the left *pcg* have more than half of the voxels with significant correlation. In all other regions no more than half of the voxels reach significance.

According to the z-tests few voxels show significant group difference in the fractions of single-fiber, two-fiber, and three-fiber voxels in each cluster. Among the clusters where the mean coherence is significantly lower in SZ, the left *ic*, the right posterior *ifo/ilf*, the left posterior *slf*, the right posterior *cc/cg*, the right *unf*, the left *acg/pcg*, and the right *fm* exhibit significantly lower coherence in the two-fiber voxel and/or the three-fiber voxel subgroup. No significant coherence difference in the single-fiber voxel subgroup is found in any cluster.

Figure 25 shows scatter plots of $\lambda_\perp$ vs. FA and κ vs. FA in the left posterior *slf* for data points pooled together and grouped by the number of fibers. Since there is no significant group difference in the number of fibers or coherence in the single-fiber and three-fiber voxels, the lower mean coherence in the entire cluster in SZ is mainly attributed to the large fraction of two-fiber voxels and their reduced coherence. It is obvious that in this region FA is strongly correlated with $\lambda_\perp$. The reduced FA in SZ is mainly due to the increased $\lambda_\perp$, and the decreased κ in the two-fiber voxels also plays a role in the FA abnormalities. Similar results are found in the left posterior *ic* and the right

posterior *cc/cg*, the right posterior *ifo/ilf*, the right *fm*, the right *unf*, and the left *acg/pcg*. In the right *fm*, coherence in single-fiber and two-fiber voxels is almost the same for the two groups, and the cluster difference mainly comes from the three-fiber voxels even though the number of these voxels is much smaller than that of two-fiber voxels. In the right *ifo/ilf* and the left post central gyrus both the two-fiber and three-fiber subgroups contribute to the significant group difference in κ.

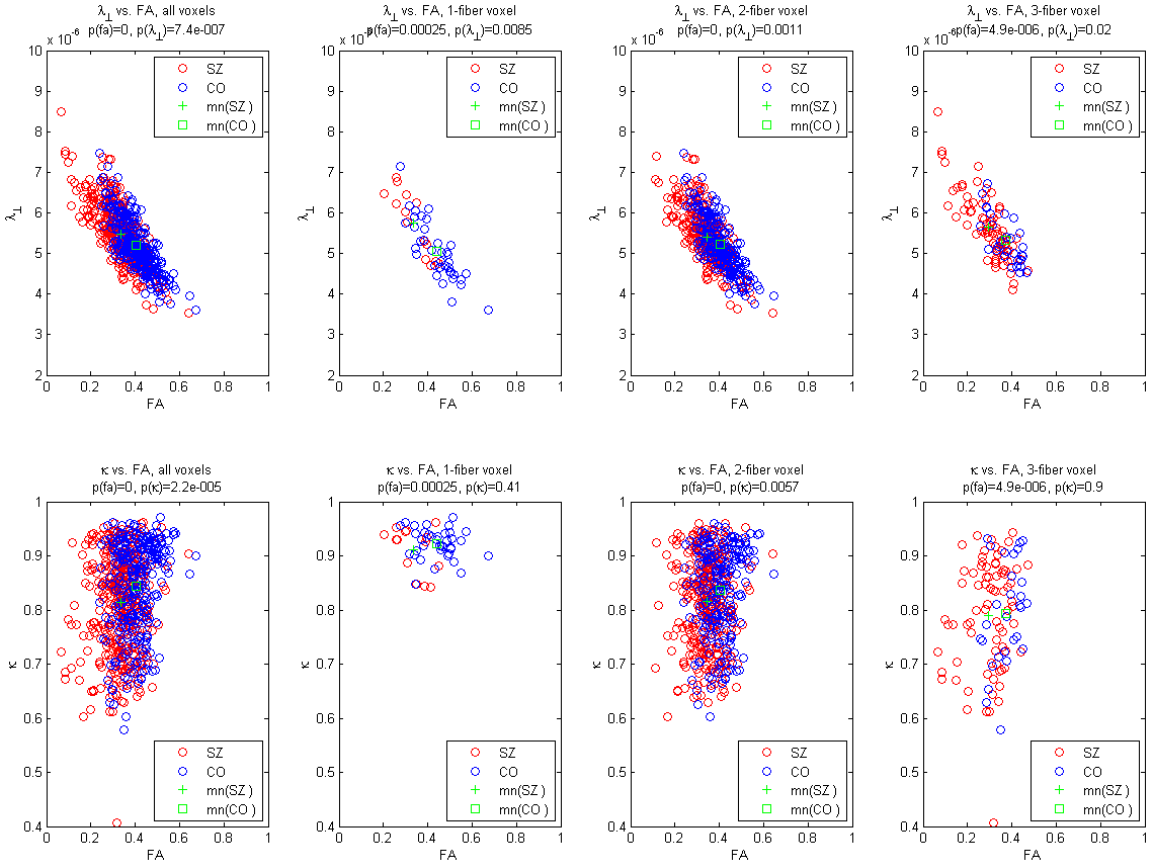

Figure 25. Scatter plots of $\lambda_{\perp}$ vs. FA (top) and κ vs. FA (bottom) in left posterior *slf* for all voxels in the cluster (1st column), for the subgroups of single-fiber voxels (2nd column), two-fiber voxels (3rd column), and three-fiber voxels (4th column). The P values of t-tests are shown in titles. The green cross denotes the mean of the SZ group and the green square denotes the mean of the CO group.

Discussion

The frontal and temporal lobes are two major regions where patients with schizophrenia have shown abnormalities in structure, neuropathology, and function. Examples are white matter volume reduction (77), total volume reduction (79), interstitial neuron misdistribution (109), abnormal metabolic rate (103), and magnetization transfer ratio reduction (96,110). Diffusion MRI provides another line of evidence for the white matter abnormalities in these regions. Our findings of FA reduction in the right anterior corona radiata/corpus callosum agree with the previous DTI investigation of Ardekani et al. (94). Also, our findings in the bilateral interior frontal-occipital/inferior longitudinal fasciculi in the temporal regions are consistent with previous reports (96,101).

In addition to the white matter projected into or past the frontal and temporal lobes from other brain regions, the fibers connecting these two areas directly are proposed to play an important role in the neuropathology of schizophrenia. There are three major fiber bundles connecting the frontal and temporal lobes: the uncinate fasciculi, the superior longitudinal fasciculus, and the cingulum bundles. In our study, patients with schizophrenia show decreased FA values in the right uncinate fasciculus. Kubicki et al. (102) showed a significant correlation between the FA values in the right uncinate fasciculus and visual attention in patients with schizophrenia, though the FA values did not differ from healthy controls. Larger sample size and more advanced imaging and

analysis techniques may explain why our study appears to have higher sensitivity in detecting abnormalities in the fiber tract.

We also found FA reduction in the left *slf* in the patient group. Left *slf* is the major fiber pathway connecting Wernicke's and Broca's areas, two important cortical regions involved in language processing. A number of functional studies have suggested a link between language disturbance in SZ and dysfunction in these two areas (111-115). Earlier DTI studies in SZ also reported abnormalities in the left *slf*, (96,100,101). Our results support the hypothesis that both these cortical regions and the fiber pathway between them may contribute to the verbal deficits in SZ patients.

Several previous DTI studies have revealed decreased FA value in the anterior and/or middle part of the cingulum bundles (96,98,99). In our patients, however, the anterior and middle parts of the cingulum bundles do not differ in FA compared with the controls, while the posterior part of the *cg* and the adjacent corpus callosum seem to be affected. Nevertheless, our findings, together with the structural, neuropathological, and functional abnormalities mentioned above, suggest that disturbed communication within and between the frontal and temporal lobes may play an important role in the pathology of schizophrenia.

The corpus callosum is the major fiber bundle connecting the left and right hemispheres. Previous DTI investigations in schizophrenia have revealed FA reduction in the genu (90,95) and the body (96) of the *cc*. Our finding of abnormalities in the *cc* provides another line of evidence for the hypothesis that inefficient communication may

be related to functional asymmetry of the two hemispheres (116) and many cognitive deficits in schizophrenia (117).

Our finding of decreased FA in the right *fm* agrees with earlier DTI studies that identified the splenium of the *cc* and the adjacent occipital area (90,94), suggesting an association with impaired early visual processing in schizophrenia (118).

Abnormalities in the internal capsules in schizophrenia have been demonstrated in several reports. The abnormalities include reduced FA in the anterior limb of the *ic* bilaterally (92,96), and in the left alone (104). Increased FA in the posterior limb of the *ic* has also been found (92). Our finding of reduced FA in the posterior limb of the *ic* is of interest. The thalamus is an important structure relaying information between cortical and subcortical regions, as well as between cortical regions. Structural and functional alterations in the thalamus have been reported in schizophrenia (for a review, see (119)). The abnormalities observed in the current study, suggesting an association with the thalamocortical somatosensory radiations which cross the posterior limb of the *ic*, warrant further investigations.

Our study not only shows reduced FA values in multiple white matter regions in schizophrenia, which replicated the findings of previous DTI investigations, but also analyzed the intravoxel radial diffusivity and fiber coherence, providing further details of the structural alterations which are not available from conventional DTI. To the best of our knowledge, this is the first HARDI analysis applied to schizophrenia.

We found significantly elevated radial diffusivity in each affected region in the patient group, and strong correlations with the decreased FA values. There are several possible causes of the changes in radial diffusivity, such as changes in the axon diameter, in the fiber density, or damage to the myelin layer. Abnormal number and density of interstitial white matter neurons in schizophrenia have been reported based on postmortem tissues in the temporal region (84) and in the prefrontal region (85). Also, postmortem histology (83,120) and magnetization transfer ratio studies (96,110) have provided direct evidence of myelin sheath damage, as well as indirect evidence from abnormalities in oligodendrocytes. Furthermore, genetic studies (86-88) have detected abnormal oligodendrocyte-related and myelination-related gene expression in schizophrenia. These findings all support our results of radial diffusivity elevation.

In addition to the increased radial diffusivity, decreased intravoxel fiber coherence is found in most of the regions with reduced FA values, though the degree of alteration varies for different tracts. Note that in our samples the FA differences between groups are found in areas where multiple fiber bundles with different orientations either cross (e.g. the *cc/cg*, *acr/cc*), or converge/diverge (e.g., the *cpt/cst*). Moreover, in regions where decreased coherence is detected in patients, no significant group difference is found on the numbers of fibers, or fiber coherence in the single-fiber voxels. These results suggest that the observed coherence differences are likely related to the way multiple fibers share a region, rather than the way fibers with similar orientations pack into a bundle.

By transforming the FOD functions from each subject's native space into a common space, it is possible to compare the three-dimensional intravoxel fiber distribution directly between subjects. In the present study we considered only the scalar coherence index derived from the FOD function. To investigate more details of fiber crossing, future work may extend to compare the full FOD functions, or even individual fiber tracts obtained in the common space.

There are several limitations to the current study. First, in our FORECAST analysis there are possible violations of the assumption that different fiber components within a voxel share the same radial diffusivity. Since radial diffusivity is affected by a number of factors, such as the fiber density, and axon diameter, and the myelin thickness, it is possible that two fiber bundles sharing the same region have different radial diffusivities. Violations of this assumption may affect the estimated volume fractions of each fiber components within a voxel (54), and hence the shape of the estimated FOD function and the intravoxel coherence index. Note that in the present study, reduced coherence in multiple-fiber voxels are observed in patients, while no group difference in either the number of fibers, or the crossing angles is detected. Therefore, except for the 'true' differences in the way multiple fiber bundles meet, another possible cause of the observed coherence abnormalities is a difference in the estimated volume fraction of one of the fiber components, which may actually result from changes in radial diffusivity of one bundle. The original FORECAST model under the single radial diffusivity assumption is not able to distinguish between these two cases. A more advanced model

has been proposed to estimate multiple radial diffusivities and FODs within a voxel (62,121). However, the method was demonstrated on high-SNR data not achievable in typical clinical environments. Further investigations will be needed to understand the coherence abnormalities.

In the present study, voxel-based t-tests were performed to detect FA differences between groups. In general, voxel-based analysis relies on accurate image registration, and misregistration may lead to false positive (and false negative) results. We carefully developed a multistep registration process, taking into account not only the inter-subject variations in brain anatomy, size, and orientation, but also factors such as subject movement and susceptibility artifacts, which may affect accuracy of intra-subject registration. Although this method provided robust performance for large fiber bundles, in regions where fibers tracts branch off into the gray matter and present large anatomical variations between subjects, the results are not as satisfactory. Thus caution should be taken when interpreting statistical results in these areas. Misregistration may be part of the reason group differences in fiber coherence are not detected at the individual voxel level.

In order to further control false positive error, we set a small threshold of p-values (0.01) and a threshold of 6 continuous voxels for the cluster size, aiming to balance between low false positive error and high sensitivity.

Other limitations include a possible confound from the duration of illness and antipsychotic medication, which are not taken into account in our analysis. A longitudinal

study of first-episode patients before and after antipsychotic treatments, or comparisons between medicated and unmedicated patients may be helpful in understanding the white matter alterations that occur with disease progression and how they are affected by medication.

Conclusion

In summary, we performed voxel-based comparisons between healthy controls and patients with schizophrenia on diffusion properties derived from FORECAST analysis of HARDI images. Decreased FA and elevated radial diffusivity were found in a number of white matter regions in patients. Our results also suggest that increased radial diffusivity is the major contributor to the FA reduction, while decreased intravoxel fiber coherence also plays a role in the white matter alterations. The set of techniques employed in this work, as a step forward from conventional DTI analysis, will likely be helpful in clinical study of other white matter diseases as well.

.

CHAPTER V

CONCLUSION

FORECAST is an advanced spherical deconvolution method for the reconstruction of HARDI data. Analysis based on the FORECAST model is used to characterize the structure and organization of brain white matter. By estimating both the radial diffusivity and the fiber orientation distribution within a voxel, the FORECAST model provides detailed information about the underlying structures, which is otherwise not available from the conventional second order tensor model. The radial diffusivity describes intrinsic structural properties such as the axon diameter, the neuron number/density, and the thickness of the myelin layer. The fiber orientation distribution function provides information about the organization of the intravoxel fiber components including the orientation and the volume fraction. Based on the shape of the FOD function, we developed a scalar index to help quantitatively describe the fiber coherence within a voxel.

Using Monte Carlo simulations, we investigated the performance of the FORECAST model in terms of estimating intravoxel fiber structure using various imaging and analysis parameters. Based on the results of the simulation, as well as bootstrap analysis of *in vivo* human data, the optimal imaging and processing parameters

for conducting the FORECAST analysis within typical clinical constraints were determined, and the accuracy of the model was estimated.

In order to compare the fiber distribution between subjects, it is necessary to transform the FOD functions into a common space. We developed an algorithm of spatial normalization of the FOD function, which accounts for not only translation, but also rotation, scaling, and shearing effects of the transformation. This technique may be helpful in detecting organizational differences in white matter between groups.

Finally, we applied the techniques mentioned above to study white matter alterations in schizophrenia. Voxel-based comparisons between the patients group and the control group reveal decreased FA and increased radial diffusivity in a number of white matter regions in the patients. Our results also suggest that the FA reduction is mainly attributed to the increased radial diffusivity, while decreased intravoxel fiber coherence also contributes to the white matter alterations associated with schizophrenia. This set of techniques, as a step forward from conventional DTI analysis, will be helpful in clinical studies of white matter diseases besides schizophrenia.

APPENDIX A

THIRTY-TWO DIFFUSION DIRECTIONS

Table 5. List of the Cartesian coordinates of the 32 unit vectors uniformly distributed over a sphere used by the Philips scanner system.

x	y	z	x	y	z
1	0	0	0.7771	0.4707	-0.4178
0	1	0	0.9242	-0.1036	-0.3677
0	0	1	0.4685	-0.7674	-0.4378
-0.0424	-0.1146	-0.9925	0.8817	-0.1893	-0.4322
0.1749	-0.2005	-0.9639	0.6904	0.7062	-0.1569
0.2323	-0.1626	-0.959	0.2391	0.7571	-0.608
0.3675	0.0261	-0.9296	-0.0578	0.9837	0.1703
0.1902	0.3744	-0.9076	-0.5368	0.8361	-0.1135
-0.1168	0.8334	-0.5402	-0.9918	-0.1207	-0.0423
-0.2005	0.2527	-0.9466	-0.9968	0.0709	-0.0379
-0.4958	0.1345	-0.858	-0.8724	0.4781	-0.1014
-0.0141	-0.6281	-0.778	-0.2487	0.9335	0.2581
-0.7445	-0.1477	-0.6511	0.1183	0.9919	-0.0471
-0.7609	0.3204	-0.5643	0.3376	0.8415	0.4218
-0.1809	0.9247	-0.3351	0.5286	0.8409	0.1163
-0.6796	-0.4224	-0.5997	0.9969	0.055	-0.0571

APPENDIX B

THEORETICAL PREDICTION OF THE VARIANCE OF p_{lm}

According to the FORECAST model, the convolution relationship between the diffusion weighted signal S and the FOD function P can be expressed as a simple algebraic equation in terms of their SH coefficients $\vec{s}_{lm}$ and $\vec{p}_{lm}$:

$$p_{lm} = \frac{s_{lm}}{s_0 c_l} \tag{16}$$

where the non-negative integer l denotes the SH order, and the integer m denotes the degree or phase factor (for each l, m ranges from $-l$ to l). S_0 is the signal without diffusion weighting. c_l is the convolution kernel expansion coefficients determined by the order l, the b value, the mean diffusivity $\overline{\lambda}$, and the radial diffusivity $\lambda_\perp$ (54). Therefore, assuming that c_l is known,

$$
\begin{aligned}
\sigma_{p_{lm}}^2 &= \left(\frac{\partial p_{lm}}{\partial s_{lm}}\right)^2 \sigma_{s_{lm}}^2 + \left(\frac{\partial p_{lm}}{\partial s_0}\right)^2 \sigma_{s_0}^2 \\
&= \left(\frac{1}{c_l s_0}\right)^2 \sigma_{s_{lm}}^2 + \left(-\frac{s_{lm}}{c_l {s_0}^2}\right)^2 \sigma_{s_0}^2 \\
&= \left(\frac{1}{c_l s_0}\right)^2 \sigma_{s_{lm}}^2 + \left(-\frac{p_{lm}}{s_0}\right)^2 \sigma_{s_0}^2 \\
&= \left(\frac{s_{lm}}{c_l s_0}\right)^2 \frac{\sigma_{s_{lm}}^2}{s_{lm}^2} + p_{lm}^2 \frac{\sigma_{s_0}^2}{s_0^2} \\
&= p_{lm}^2 \cdot \left(\frac{\sigma_{s_{lm}}^2}{s_{lm}^2} + \frac{\sigma_{s_0}^2}{s_0^2}\right) \\
&= p_{lm}^2 \frac{\sigma_{s_0}^2}{s_0^2}\left(1 + \frac{\sigma_{s_{lm}}^2}{\sigma_{s_0}^2} \cdot \frac{s_0^2}{s_{lm}^2}\right)
\end{aligned}
\tag{17}
$$

The diffusion weighted signal $\vec{S}$ can be expressed in terms of its SH expansion coefficients $\vec{s}_{lm}$ as

$$\vec{S} = \widetilde{X} \cdot \vec{s}_{lm} \tag{18}$$

where $\widetilde{X}$ is the design matrix comprised of spherical harmonics. The $\vec{s}_{lm}$ is determined by linear least squares estimation using Eq.(18). Hence, the variance of s_{lm} is

$$\sigma_{s_{lm}}^2 = \sigma_s^2 \left(\widetilde{X}' \widetilde{X}\right)_{kk}^{-1} \tag{19}$$

where σ_s^2 is the variance of the diffusion-weighted signal, $\left(\widetilde{X}' \widetilde{X}\right)_{kk}^{-1}$ is the kth element on the diagonal of the matrix $\left(\widetilde{X}' \widetilde{X}\right)^{-1}$,with $k = l^2 + l + m + 1$. Assuming the variance of the diffusion-weighted signal σ_s^2 equals the variance of the non-diffusion weighted signal $\sigma_{s_0}^2$, Eq.(19) becomes

$$\sigma_{s_{lm}}^2 = \sigma_{s_0}^2 \left(\widetilde{X}' \widetilde{X}\right)_{kk}^{-1} \tag{20}$$

Inserting Eq.(20) into Eq.(17), we have

$$\sigma_{p_{lm}}^2 = p_{lm}^2 \frac{\sigma_{s_0}^2}{s_0^2}\left(1+\left(\widetilde{X}'\widetilde{X}\right)_{kk}^{-1}\cdot\frac{s_0^2}{s_{lm}^2}\right)$$
$$= \frac{1}{SNR^2}\left(p_{lm}^2+\left(\widetilde{X}'\widetilde{X}\right)_{kk}^{-1}\frac{1}{c_l^{\,2}}\right) \qquad (21)$$

Therefore, for a given fitting order l, to minimize the variance of the estimated p_{lm}, the b *value* should be chosen to maximize $|c_l|$. Hence for a typical value of $\lambda_\perp = 0.54\times10^{-5} cm^2/s$, the $l=6$ order coefficients, $\vec{p}_{6m}$, have the lowest variance at $b = 3200 s/mm^2$. The dependence of c_l on the b value is shown in Figure 26.

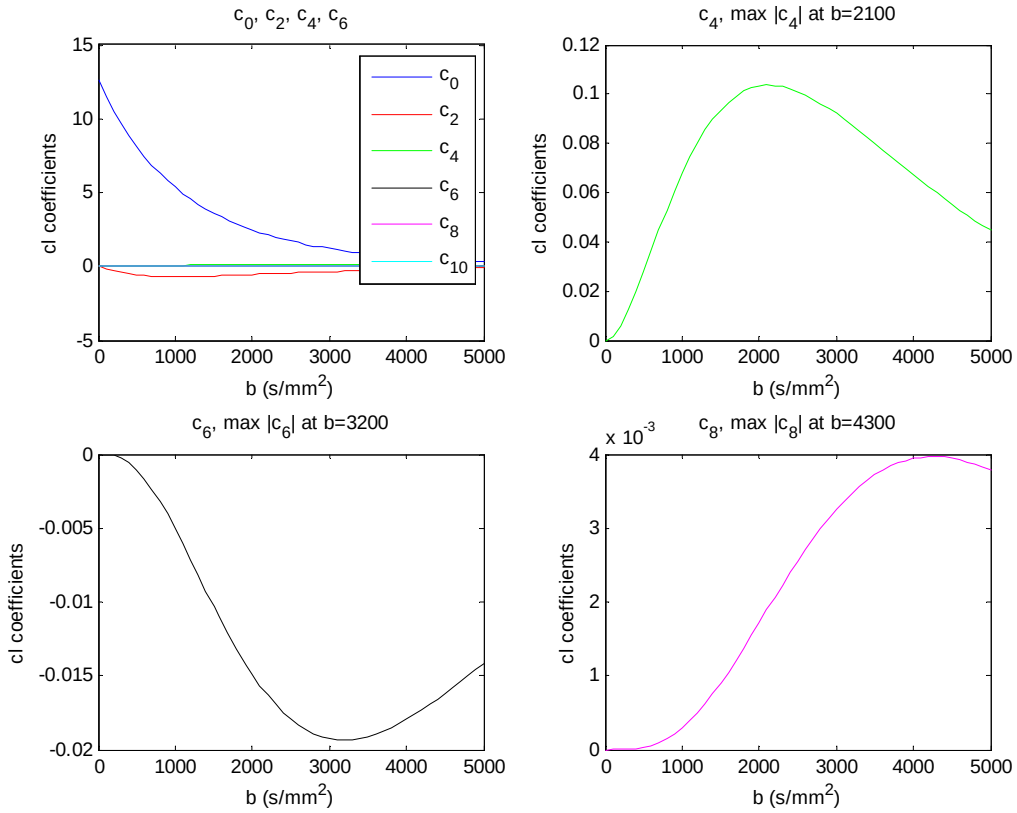

Figure 26. Coefficients c_l vs. b. Subplot in top left shows c_l for even orders from 0 to 10. The other subplots show c_l for orders 4, 6 and 8 (assuming $\lambda_\perp = 0.54\times10^{-3} mm^2/s$).

REFERENCES

1. Basser PJ, Mattiello J, LeBihan D. MR diffusion tensor spectroscopy and imaging. Biophysical journal 1994;66(1):259-267.

2. Basser PJ, Pierpaoli C. Microstructural and physiological features of tissues elucidated by quantitative-diffusion-tensor MRI. Journal of magnetic resonance 1996;111(3):209-219.

3. Beaulieu C. The basis of anisotropic water diffusion in the nervous system - a technical review. NMR in biomedicine 2002;15(7-8):435-455.

4. Conturo TE, Lori NF, Cull TS, Akbudak E, Snyder AZ, Shimony JS, McKinstry RC, Burton H, Raichle ME. Tracking neuronal fiber pathways in the living human brain. Proceedings of the National Academy of Sciences of the United States of America 1999;96(18):10422-10427.

5. Mori S, Wakana S, Nagae-Poetscher LM, van Zijl PCM. MRI atlas of human white matter. Amsterdam: Elsevier; 2005.

6. Mori S, Crain BJ, Chacko VP, van Zijl PC. Three-dimensional tracking of axonal projections in the brain by magnetic resonance imaging. Annals of neurology 1999;45(2):265-269.

7. Miller SP, Vigneron DB, Henry RG, Bohland MA, Ceppi-Cozzio C, Hoffman C, Newton N, Partridge JC, Ferriero DM, Barkovich AJ. Serial quantitative diffusion tensor MRI of the premature brain: development in newborns with and without injury. J Magn Reson Imaging 2002;16(6):621-632.

8. Warach S, Chien D, Li W, Ronthal M, Edelman RR. Fast magnetic resonance diffusion-weighted imaging of acute human stroke. Neurology 1992;42(9):1717-1723.

9. Miller DH, Grossman RI, Reingold SC, McFarland HF. The role of magnetic resonance techniques in understanding and managing multiple sclerosis. Brain 1998;121 (Pt 1):3-24.

10. Hugg JW, Butterworth EJ, Kuzniecky RI. Diffusion mapping applied to mesial temporal lobe epilepsy: preliminary observations. Neurology 1999;53(1):173-176.

11. Ito R, Melhem ER, Mori S, Eichler FS, Raymond GV, Moser HW. Diffusion tensor brain MR imaging in X-linked cerebral adrenoleukodystrophy. Neurology 2001;56(4):544-547.

12. Kono K, Inoue Y, Nakayama K, Shakudo M, Morino M, Ohata K, Wakasa K, Yamada R. The role of diffusion-weighted imaging in patients with brain tumors. Ajnr 2001;22(6):1081-1088.

13. Nusbaum AO, Tang CY, Buchsbaum MS, Wei TC, Atlas SW. Regional and global changes in cerebral diffusion with normal aging. Ajnr 2001;22(1):136-142.

14. Ricci PE, Burdette JH, Elster AD, Reboussin DM. A comparison of fast spin-echo, fluid-attenuated inversion-recovery, and diffusion-weighted MR imaging in the first 10 days after cerebral infarction. Ajnr 1999;20(8):1535-1542.

15. Sorensen AG, Wu O, Copen WA, Davis TL, Gonzalez RG, Koroshetz WJ, Reese TG, Rosen BR, Wedeen VJ, Weisskoff RM. Human acute cerebral ischemia: detection of changes in water diffusion anisotropy by using MR imaging. Radiology 1999;212(3):785-792.

16. Tievsky AL, Ptak T, Farkas J. Investigation of apparent diffusion coefficient and diffusion tensor anisotrophy in acute and chronic multiple sclerosis lesions. Ajnr 1999;20(8):1491-1499.

17. Bozzali M, Cercignani M, Sormani MP, Comi G, Filippi M. Quantification of brain gray matter damage in different MS phenotypes by use of diffusion tensor MR imaging. Ajnr 2002;23(6):985-988.

18. Cercignani M, Bozzali M, Iannucci G, Comi G, Filippi M. Intra-voxel and inter-voxel coherence in patients with multiple sclerosis assessed using diffusion tensor MRI. Journal of neurology 2002;249(7):875-883.

19. Eriksson SH, Rugg-Gunn FJ, Symms MR, Barker GJ, Duncan JS. Diffusion tensor imaging in patients with epilepsy and malformations of cortical development. Brain 2001;124(Pt 3):617-626.

20. Krabbe K, Gideon P, Wagn P, Hansen U, Thomsen C, Madsen F. MR diffusion imaging of human intracranial tumours. Neuroradiology 1997;39(7):483-489.

21. Guo AC, Cummings TJ, Dash RC, Provenzale JM. Lymphomas and high-grade astrocytomas: comparison of water diffusibility and histologic characteristics. Radiology 2002;224(1):177-183.

22. Wiegell MR, Larsson HB, Wedeen VJ. Fiber crossing in human brain depicted with diffusion tensor MR imaging. Radiology 2000;217(3):897-903.

23. Tuch DS, Reese TG, Wiegell MR, Makris N, Belliveau JW, Wedeen VJ. High angular resolution diffusion imaging reveals intravoxel white matter fiber heterogeneity. Magn Reson Med 2002;48(4):577-582.

24. Alexander DC, Barker GJ, Arridge SR. Detection and modeling of non-Gaussian apparent diffusion coefficient profiles in human brain data. Magn Reson Med 2002;48(2):331-340.

25. Frank LR. Anisotropy in high angular resolution diffusion-weighted MRI. Magn Reson Med 2001;45(6):935-939.

26. Ozarslan E, Mareci TH. Generalized diffusion tensor imaging and analytical relationships between diffusion tensor imaging and high angular resolution diffusion imaging. Magn Reson Med 2003;50(5):955-965.

27. Jansons KM, Alexander DC. Persistent Angular Structure: new insights from diffusion MRI data. Dummy version. Inf Process Med Imaging 2003;18:672-683.

28. Tuch DS, Reese TG, Wiegell MR, Wedeen VJ. Diffusion MRI of complex neural architecture. Neuron 2003;40(5):885-895.

29. Tuch DS. Q-ball imaging. Magn Reson Med 2004;52(6):1358-1372.

30. Wedeen VJ, Reese TG, Tuch DS, Weigel MR, Dou J-G, Weiskoff RM, Chessler D. Mapping fiber orientation spectra in cerebral white matter with Fourier-transform diffusion MRI. Proc Intl Soc Mag Reson Med 2000;8:82.

31. Moseley ME, Cohen Y, Kucharczyk J, Mintorovitch J, Asgari HS, Wendland MF, Tsuruda J, Norman D. Diffusion-weighted MR imaging of anisotropic water diffusion in cat central nervous system. Radiology 1990;176(2):439-445.

32. Pierpaoli C, Basser PJ. Toward a quantitative assessment of diffusion anisotropy. Magn Reson Med 1996;36(6):893-906.

33. Basser PJ, Mattiello J, LeBihan D. Estimation of the effective self-diffusion tensor from the NMR spin echo. Journal of magnetic resonance 1994;103(3):247-254.

34. Stejskal EO, Tanner JE. Spin diffusion measurements: spin echoes in the presence of a time-dependent field gradient. J Chem Phys 1965;42:288-292.

35. Mori S, van Zijl PC. Fiber tracking: principles and strategies - a technical review. NMR in biomedicine 2002;15(7-8):468-480.

36. Lori NF, Akbudak E, Shimony JS, Cull TS, Snyder AZ, Guillory RK, Conturo TE. Diffusion tensor fiber tracking of human brain connectivity: aquisition methods, reliability analysis and biological results. NMR in biomedicine 2002;15(7-8):494-515.

37. Khong PL, Leung LH, Fung AS, Fong DY, Qiu D, Kwong DL, Ooi GC, McAlanon G, Cao G, Chan GC. White matter anisotropy in post-treatment childhood cancer survivors: preliminary evidence of association with neurocognitive function. J Clin Oncol 2006;24(6):884-890.

38. Hall DE, Moffat BA, Stojanovska J, Johnson TD, Li Z, Hamstra DA, Rehemtulla A, Chenevert TL, Carter J, Pietronigro D, Ross BD. Therapeutic efficacy of DTI-015 using diffusion magnetic resonance imaging as an early surrogate marker. Clin Cancer Res 2004;10(23):7852-7859.

39. Dong Q, Welsh RC, Chenevert TL, Carlos RC, Maly-Sundgren P, Gomez-Hassan DM, Mukherji SK. Clinical applications of diffusion tensor imaging. J Magn Reson Imaging 2004;19(1):6-18.

40. Alexander AL, Hasan KM, Lazar M, Tsuruda JS, Parker DL. Analysis of partial volume effects in diffusion-tensor MRI. Magn Reson Med 2001;45(5):770-780.

41. Poupon C, Bloch I. Détection des faisceaux de fibres de la substance blanche pour l'étude de la connectivité anatomique cérébrale (Tracking of white matter fiber bundles for the study of cerebral connectivity). Paris, FRANCE: Ecole nationale supérieure des télécommunications; 1999.

42. Pierpaoli C, Barnett A, Pajevic S, Chen R, Penix LR, Virta A, Basser P. Water diffusion changes in Wallerian degeneration and their dependence on white matter architecture. NeuroImage 2001;13(6 Pt 1):1174-1185.

43. Wiegell MR, Reese TG, Tuch DS, Sorensen AG, Wedeen VJ. Diffusion spectrum imaging of fiber white matter degeneration. Proc Intl Soc Mag Reson Med 2001;9:504.

44. Tuch DS. MRI of complex tissue structure. Cambridge, Massachusetts: Harvard University-Massachusetts Institute of Technology; 2002.

45. Callaghan PT, Eccles CD, Xia Y. NMR microscopy of dynamic displacements: k-space and q-space imaging. J Phys E: Sci Instrum 1988;21:820-828.

46. Parker GJ, Alexander DC. Probabilistic Monte Carlo based mapping of cerebral connections utilising whole-brain crossing fibre information. Inf Process Med Imaging 2003;18:684-695.

47. Frank LR. Characterization of anisotropy in high angular resolution diffusion-weighted MRI. Magn Reson Med 2002;47(6):1083-1099.

48. Liu C, Bammer R, Acar B, Moseley ME. Characterizing non-Gaussian diffusion by using generalized diffusion tensors. Magn Reson Med 2004;51(5):924-937.

49. von dem Hagen EA, Henkelman RM. Orientational diffusion reflects fiber structure within a voxel. Magn Reson Med 2002;48(3):454-459.

50. Zhan W, Stein EA, Yang Y. Mapping the orientation of intravoxel crossing fibers based on the phase information of diffusion circular spectrum. NeuroImage 2004;23(4):1358-1369.

51. Ozarslan E, Shepherd TM, Vemuri BC, Blackband SJ, Mareci TH. Resolution of complex tissue microarchitecture using the diffusion orientation transform (DOT). NeuroImage 2006;31(3):1086-1103.

52. Anderson AW, Ding Z. Sub-voxel measurement of fiber orientation using high angular resolution diffusion tensor imaging. Proc Intl Soc Mag Reson Med 2002;10:440.

53. Tournier JD, Calamante F, Gadian DG, Connelly A. Direct estimation of the fiber orientation density function from diffusion-weighted MRI data using spherical deconvolution. NeuroImage 2004;23(3):1176-1185.

54. Anderson AW. Measurement of fiber orientation distributions using high angular resolution diffusion imaging. Magn Reson Med 2005;54(5):1194-1206.

55. Hong X, Anderson AW, Ding Z. Resolve Fiber Orientation Ambiguity Using HARD Imaging. Proc Intl Soc Mag Reson Med 2006;14:2728.

56. Hess CP, Mukherjee P, Han ET, Xu D, Vigneron DB. Q-ball reconstruction of multimodal fiber orientations using the spherical harmonic basis. Magn Reson Med 2006;56(1):104-117.

57. Descoteaux M, Angelino E, Fitzgibbons S, Deriche R. Apparent diffusion coefficients from high angular resolution diffusion imaging: estimation and applications. Magn Reson Med 2006;56(2):395-410.

58. Tournier JD, Calamante F, Connelly A. Improved characterization of crossing fibers: optimisation of spherical deconvolution parameters using a minimum entropy principle. Proc Intl Soc Mag Reson Med 2005;13:384.

59. Tournier JD, Calamante F, Connelly A. Improved characterisation of crossing fibres: spherical deconvolution combined with Tikhonov regularization. Proc Intl Soc Mag Reson Med 2006;14:645.

60. Sakaie KE, Lowe MJ. An objective method for regularization of fiber orientation distributions derived from diffusion-weighted MRI. NeuroImage 2007;34(1):169-176.

61. Tournier JD, Calamante F, Connelly A. Robust determination of the fibre orientation distribution in diffusion MRI: non-negativity constrained super-resolved spherical deconvolution. NeuroImage 2007;35(4):1459-1472.

62. Jeong H-K. Imaging of brain white matter using diffusion weighted magnetic resonance imaging. Nashville, TN: Vanderbilt University; 2008.

63. Hansen PC. Regularization Tools: A Matlab Package For Analysis and Solution of Discrete Ill-posed Problems. Numerical algorithms 1994;6:1-35.

64. Ritchie DW. Fast computation, rotation and comparison of low resolution spherical harmonic molecular surfaces. J Comput Chem 1998;20:383-395.

65. Efron B, Tibshirani RJ. An Introduction To the Bootstrap: Chapman & Hall/CRC; 1994. 436 p.

66. Skare S, Li T, Nordell B, Ingvar M. Noise considerations in the determination of diffusion tensor anisotropy. Magnetic resonance imaging 2000;18(6):659-669.

67. Zhou XJ, Leeds NE. Assessing glioma cell infiltration using a fiber coherence index: a DTI study. Proc Intl Soc Mag Reson Med 2006;14:365.

68. Mardia KV, Jupp PE. Directional Statistics: Wiley; 1999. 350 p.

69. Alexander DC, Pierpaoli C, Basser PJ, Gee JC. Spatial transformations of diffusion tensor magnetic resonance images. IEEE transactions on medical imaging 2001;20(11):1131-1139.

70. Xu D, Mori S, Shen D, van Zijl PC, Davatzikos C. Spatial normalization of diffusion tensor fields. Magn Reson Med 2003;50(1):175-182.

71. Wolfram S. The Mathematica Book: Wolfram Media/Cambridge University Press; 1996.

72. Netsch T, van Muiswinkel A. Quantitative evaluation of image-based distortion correction in diffusion tensor imaging. IEEE transactions on medical imaging 2004;23(7):789-798.

73. Li R. Automatic placement of regions of interest in medical images using image registration [Master's degree thesis]. Nashville, TN, USA: Vanderbilt University; 2001.

74. Rohde GK, Aldroubi A, Dawant BM. The adaptive bases algorithm for intensity-based nonrigid image registration. IEEE transactions on medical imaging 2003;22(11):1470-1479.

75. Arlinghaus LR. Investigating tract-specific changes in white matter with diffusion tensor imaging. Nashville, TN, USA: Vanderbilt University; 2009. 106 p.

76. Chiang MC, Leow AD, Klunder AD, Dutton RA, Barysheva M, Rose SE, McMahon KL, de Zubicaray GI, Toga AW, Thompson PM. Fluid registration of diffusion tensor images using information theory. IEEE transactions on medical imaging 2008;27(4):442-456.

77. Breier A, Buchanan RW, Elkashef A, Munson RC, Kirkpatrick B, Gellad F. Brain morphology and schizophrenia. A magnetic resonance imaging study of limbic, prefrontal cortex, and caudate structures. Archives of general psychiatry 1992;49(12):921-926.

78. DeLisi LE, Sakuma M, Ge S, Kushner M. Association of brain structural change with the heterogeneous course of schizophrenia from early childhood through five years subsequent to a first hospitalization. Psychiatry research 1998;84(2-3):75-88.

79. Gur RE, Cowell P, Turetsky BI, Gallacher F, Cannon T, Bilker W, Gur RC. A follow-up magnetic resonance imaging study of schizophrenia. Relationship of neuroanatomical changes to clinical and neurobehavioral measures. Archives of general psychiatry 1998;55(2):145-152.

80. Weinberger DR, Berman KF, Suddath R, Torrey EF. Evidence of dysfunction of a prefrontal-limbic network in schizophrenia: a magnetic resonance imaging and regional cerebral blood flow study of discordant monozygotic twins. The American journal of psychiatry 1992;149(7):890-897.

81. Yurgelun-Todd DA, Waternaux CM, Cohen BM, Gruber SA, English CD, Renshaw PF. Functional magnetic resonance imaging of schizophrenic patients and comparison subjects during word production. The American journal of psychiatry 1996;153(2):200-205.

82. Shergill SS, Brammer MJ, Williams SC, Murray RM, McGuire PK. Mapping auditory hallucinations in schizophrenia using functional magnetic resonance imaging. Archives of general psychiatry 2000;57(11):1033-1038.

83. Uranova N, Orlovskaya D, Vikhreva O, Zimina I, Kolomeets N, Vostrikov V, Rachmanova V. Electron microscopy of oligodendroglia in severe mental illness. Brain research bulletin 2001;55(5):597-610.

84. Eastwood SL, Harrison PJ. Interstitial white matter neurons express less reelin and are abnormally distributed in schizophrenia: towards an integration of molecular and morphologic aspects of the neurodevelopmental hypothesis. Molecular psychiatry 2003;8(9):769, 821-731.

85. Kirkpatrick B, Messias NC, Conley RR, Roberts RC. Interstitial cells of the white matter in the dorsolateral prefrontal cortex in deficit and nondeficit schizophrenia. The Journal of nervous and mental disease 2003;191(9):563-567.

86. Hakak Y, Walker JR, Li C, Wong WH, Davis KL, Buxbaum JD, Haroutunian V, Fienberg AA. Genome-wide expression analysis reveals dysregulation of myelination-related genes in chronic schizophrenia. Proceedings of the National Academy of Sciences of the United States of America 2001;98(8):4746-4751.

87. Tkachev D, Mimmack ML, Ryan MM, Wayland M, Freeman T, Jones PB, Starkey M, Webster MJ, Yolken RH, Bahn S. Oligodendrocyte dysfunction in schizophrenia and bipolar disorder. Lancet 2003;362(9386):798-805.

88. Aston C, Jiang L, Sokolov BP. Microarray analysis of postmortem temporal cortex from patients with schizophrenia. Journal of neuroscience research 2004;77(6):858-866.

89. Lim KO, Hedehus M, Moseley M, de Crespigny A, Sullivan EV, Pfefferbaum A. Compromised white matter tract integrity in schizophrenia inferred from diffusion tensor imaging. Archives of general psychiatry 1999;56(4):367-374.

90. Agartz I, Andersson JL, Skare S. Abnormal brain white matter in schizophrenia: a diffusion tensor imaging study. Neuroreport 2001;12(10):2251-2254.

91. Minami T, Nobuhara K, Okugawa G, Takase K, Yoshida T, Sawada S, Ha-Kawa S, Ikeda K, Kinoshita T. Diffusion tensor magnetic resonance imaging of disruption of regional white matter in schizophrenia. Neuropsychobiology 2003;47(3):141-145.

92. Buchsbaum MS, Friedman J, Buchsbaum BR, Chu KW, Hazlett EA, Newmark R, Schneiderman JS, Torosjan Y, Tang C, Hof PR, Stewart D, Davis KL, Gorman J. Diffusion tensor imaging in schizophrenia. Biological psychiatry 2006;60(11):1181-1187.

93. Kanaan R, Barker G, Brammer M, Giampietro V, Shergill S, Woolley J, Picchioni M, Toulopoulou T, McGuire P. White matter microstructure in schizophrenia:

effects of disorder, duration and medication. Br J Psychiatry 2009;194(3):236-242.

94. Ardekani BA, Nierenberg J, Hoptman MJ, Javitt DC, Lim KO. MRI study of white matter diffusion anisotropy in schizophrenia. Neuroreport 2003;14(16):2025-2029.

95. Caan MW, Vermeer KA, van Vliet LJ, Majoie CB, Peters BD, den Heeten GJ, Vos FM. Shaving diffusion tensor images in discriminant analysis: a study into schizophrenia. Medical image analysis 2006;10(6):841-849.

96. Kubicki M, Park H, Westin CF, Nestor PG, Mulkern RV, Maier SE, Niznikiewicz M, Connor EE, Levitt JJ, Frumin M, Kikinis R, Jolesz FA, McCarley RW, Shenton ME. DTI and MTR abnormalities in schizophrenia: analysis of white matter integrity. NeuroImage 2005;26(4):1109-1118.

97. Kubicki M, Westin CF, Nestor PG, Wible CG, Frumin M, Maier SE, Kikinis R, Jolesz FA, McCarley RW, Shenton ME. Cingulate fasciculus integrity disruption in schizophrenia: a magnetic resonance diffusion tensor imaging study. Biological psychiatry 2003;54(11):1171-1180.

98. Hao Y, Liu Z, Jiang T, Gong G, Liu H, Tan L, Kuang F, Xu L, Yi Y, Zhang Z. White matter integrity of the whole brain is disrupted in first-episode schizophrenia. Neuroreport 2006;17(1):23-26.

99. Kumra S, Ashtari M, Cervellione KL, Henderson I, Kester H, Roofeh D, Wu J, Clarke T, Thaden E, Kane JM, Rhinewine J, Lencz T, Diamond A, Ardekani BA, Szeszko PR. White matter abnormalities in early-onset schizophrenia: a voxel-based diffusion tensor imaging study. Journal of the American Academy of Child and Adolescent Psychiatry 2005;44(9):934-941.

100. Burns J, Job D, Bastin ME, Whalley H, Macgillivray T, Johnstone EC, Lawrie SM. Structural disconnectivity in schizophrenia: a diffusion tensor magnetic resonance imaging study. Br J Psychiatry 2003;182:439-443.

101. Hubl D, Koenig T, Strik W, Federspiel A, Kreis R, Boesch C, Maier SE, Schroth G, Lovblad K, Dierks T. Pathways that make voices: white matter changes in auditory hallucinations. Archives of general psychiatry 2004;61(7):658-668.

102. Kubicki M, Westin CF, Maier SE, Frumin M, Nestor PG, Salisbury DF, Kikinis R, Jolesz FA, McCarley RW, Shenton ME. Uncinate fasciculus findings in schizophrenia: a magnetic resonance diffusion tensor imaging study. The American journal of psychiatry 2002;159(5):813-820.

103. Buchsbaum MS, Tang CY, Peled S, Gudbjartsson H, Lu D, Hazlett EA, Downhill J, Haznedar M, Fallon JH, Atlas SW. MRI white matter diffusion anisotropy and PET metabolic rate in schizophrenia. Neuroreport 1998;9(3):425-430.

104. Szeszko PR, Ardekani BA, Ashtari M, Kumra S, Robinson DG, Sevy S, Gunduz-Bruce H, Malhotra AK, Kane JM, Bilder RM, Lim KO. White matter abnormalities in first-episode schizophrenia or schizoaffective disorder: a diffusion tensor imaging study. The American journal of psychiatry 2005;162(3):602-605.

105. Kubicki M, McCarley R, Westin CF, Park HJ, Maier S, Kikinis R, Jolesz FA, Shenton ME. A review of diffusion tensor imaging studies in schizophrenia. Journal of psychiatric research 2007;41(1-2):15-30.

106. Hong X, Arlinghaus LR, Anderson AW. Spatial normalization of the fiber orientation distribution based on high angular resolution diffusion imaging data. Magn Reson Med 2009;61(6):1520-1527.

107. Jezzard P, Balaban RS. Correction for geometric distortion in echo planar images from B0 field variations. Magn Reson Med 1995;34(1):65-73.

108. Hong X, Arlinghaus LR, Anderson AW. Altered Fiber Radial Diffusivity in Schizophrenia Revealed by Diffusion MRI. Proc Intl Soc Mag Reson Med 2007;15:342.

109. Akbarian S, Kim JJ, Potkin SG, Hetrick WP, Bunney WE, Jr., Jones EG. Maldistribution of interstitial neurons in prefrontal white matter of the brains of schizophrenic patients. Archives of general psychiatry 1996;53(5):425-436.

110. Foong J, Symms MR, Barker GJ, Maier M, Woermann FG, Miller DH, Ron MA. Neuropathological abnormalities in schizophrenia: evidence from magnetization transfer imaging. Brain 2001;124(Pt 5):882-892.

111. Niznikiewicz MA, O'Donnell BF, Nestor PG, Smith L, Law S, Karapelou M, Shenton ME, McCarley RW. ERP assessment of visual and auditory language processing in schizophrenia. Journal of abnormal psychology 1997;106(1):85-94.

112. Fletcher PC, McKenna PJ, Frith CD, Grasby PM, Friston KJ, Dolan RJ. Brain activations in schizophrenia during a graded memory task studied with functional neuroimaging. Archives of general psychiatry 1998;55(11):1001-1008.

113. Hazlett EA, Buchsbaum MS, Jeu LA, Nenadic I, Fleischman MB, Shihabuddin L, Haznedar MM, Harvey PD. Hypofrontality in unmedicated schizophrenia patients studied with PET during performance of a serial verbal learning task. Schizophrenia research 2000;43(1):33-46.

114. Guillem F, Bicu M, Hooper R, Bloom D, Wolf MA, Messier J, Desautels R, Debruille JB. Memory impairment in schizophrenia: a study using event-related potentials in implicit and explicit tasks. Psychiatry research 2001;104(2):157-173.

115. Kubicki M, McCarley RW, Nestor PG, Huh T, Kikinis R, Shenton ME, Wible CG. An fMRI study of semantic processing in men with schizophrenia. NeuroImage 2003;20(4):1923-1933.

116. Gruzelier JH. Functional neuropsychophysiological asymmetry in schizophrenia: a review and reorientation. Schizophrenia bulletin 1999;25(1):91-120.

117. Crow TJ. Schizophrenia as a transcallosal misconnection syndrome. Schizophrenia research 1998;30(2):111-114.

118. Butler PD, Schechter I, Zemon V, Schwartz SG, Greenstein VC, Gordon J, Schroeder CE, Javitt DC. Dysfunction of early-stage visual processing in schizophrenia. The American journal of psychiatry 2001;158(7):1126-1133.

119. Byne W, Hazlett EA, Buchsbaum MS, Kemether E. The thalamus and schizophrenia: current status of research. Acta neuropathologica 2009;117(4):347-368.

120. Hof PR, Haroutunian V, Friedrich VL, Jr., Byne W, Buitron C, Perl DP, Davis KL. Loss and altered spatial distribution of oligodendrocytes in the superior frontal gyrus in schizophrenia. Biological psychiatry 2003;53(12):1075-1085.

121. Jeong H-K, Anderson AW. Measurement of intrinsic fiber diffusivity using spherical deconvolution of high angular resolution diffusion data. Proc Intl Soc Mag Reson Med 2007;15:905.